https://theses.gla.ac.uk/

Theses Digitisation:

https://www.gla.ac.uk/myglasgow/research/enlighten/theses/digitisation/

This is a digitised version of the original print thesis.

Copyright and moral rights for this work are retained by the author

A copy can be downloaded for personal non-commercial research or study, without prior permission or charge

This work cannot be reproduced or quoted extensively from without first obtaining permission in writing from the author

The content must not be changed in any way or sold commercially in any format or medium without the formal permission of the author

When referring to this work, full bibliographic details including the author, title, awarding institution and date of the thesis must be given

Enlighten: Theses
https://theses.gla.ac.uk/
research-enlighten@glasgow.ac.uk

An Integrated Optical Pressure Sensor in the GaAs/AlGaAs Ternary System

A thesis submitted to

the Faculty of Engineering of the

University of Glasgow for the Degree of

Doctor of Philosophy

by

Joseph James Isaac

© 1987 J.J. Isaac

October 1987

ProQuest Number: 11003392

All rights reserved

INFORMATION TO ALL USERS
The quality of this reproduction is dependent upon the quality of the copy submitted.

In the unlikely event that the author did not send a complete manuscript
and there are missing pages, these will be noted. Also, if material had to be removed,
a note will indicate the deletion.

ProQuest 11003392

Published by ProQuest LLC (2018). Copyright of the Dissertation is held by the Author.

All rights reserved.
This work is protected against unauthorized copying under Title 17, United States Code
Microform Edition © ProQuest LLC.

ProQuest LLC.
789 East Eisenhower Parkway
P.O. Box 1346
Ann Arbor, MI 48106 – 1346

Dedicated to my mother, Aletha.

Acknowledgements

I would like to thank Professor J. Lamb for the extensive research facilities provided by the Department of Electronics and Electrical Engineering during this project.

I am indebted to both my academic supervisor Professor R.M. De La Rue and my industrial supervisor Dr. K.K. Wong for their advice and encouragement throughout the project.

My thanks to the other Members of The Room: M. Fletcher, C. Mitchie and I. MacIntyre for useful discussions and support which made my stay a very pleasant one. I also wish to thank Dr. A. Nutt and Dr. M. MacBean for their advice.

Appreciation is also expressed for the efficient running of the clean room, Reactive Ion Etching, computer facilities and the Ultra-Small Structures Laboratory and the assistance of the technical staff of the Department is gratefully acknowledged.

My thanks to the Integrated Optics Group at GEC Research for the use of their facilities and assistance during this project.

I would like to acknowledge financial support by the Science and Engineering Research Council and GEC Research Ltd.

Finally, I would like to thank my family for their encouragement and support throughout my academic career.

Summary

The principal concerns of this thesis are the design, fabrication and demonstration of an optical pressure sensor in the aluminium gallium arsenide (AlGaAs) ternary epitaxial layer system. The device is based on a ridge optical waveguide traversing a section of GaAs wafer which has been wet-chemically etched, in a well-defined area, from the wafer base, through the substrate (approximately 400μm thick) to within approximately 10μm of the top surface of the wafer. A deflection of the membrane from equilibrium by a pressure differential across its thin dimension results in a stress-induced change in the refractive index of the membrane material. A guided wave on the top surface of the membrane experiences a change of phase as it passes through the stress field produced by the membrane deformation.

A mathematical theory of photoelasticity is developed to model the deflection and stress-induced refractive index changes of a membrane of material in the zinc-blende cubic crystal class ($\bar{4}3$m), of which GaAs is a member. The theoretical model was firstly tested by measuring the deflection of membranes under pressure by observing them in a microscope equipped with a Tolansky interferometer. Using the experimental apparatus described in this thesis, membrane deflection was achieved by evacuating one side of the membranes. This resulted in the pressure being limited to one atmosphere across a membrane (or limited by the evacuating capability of the vacuum pump).

Two types of device are investigated — the first uses only straight waveguides and is here referred to as a birefringent pressure sensor

while the second incorporates a Mach–Zehnder waveguide structure.

(1) The birefringent pressure sensing device was fabricated and tested. It consisted of a number of straight waveguides crossing a membrane and was placed in an external Mach–Zehnder interferometer in order to measure the phase–shift of light in the waveguide when a uniform pressure was applied to one surface of the membrane. The theoretical model indicates that the change in phase for TE and TM polarisations is different i.e there is stress–induced birefringence. Thus linearly polarised light launched into a straight waveguide (equally exciting the TE and TM polarisations) experiences a change of polarisation with pressure. The polarisation of the light output by the device could be monitored without placing the device in an external interferometer – hence the name 'birefringent pressure sensor'. This sensor was studied using both the techniques described above.

(2) The design considerations for a waveguide Mach–Zehnder interferometric pressure sensor are based on both the photoelasticity model developed in this thesis and the results obtained from the birefringent pressure sensor. The device parameters were chosen to allow at least 2π phase–shift (i.e one cycle) within the one atmosphere pressure limit in this thesis. The arm separation of the Mach–Zehnder structure is $300\mu m$ and the total device length is about 17mm. The Y–junctions are symmetric and are formed by two intersecting S–bends of radius of curvature 40mm. The arm separation and S–bend radii are limited by the losses of the device. Theoretical calculations indicate that considerably smaller radii for the S–bends would be acceptable with only a small

reduction in optical transmission.

In order to estimate the losses, the transmission of the Mach–Zehnder waveguides was compared to those for straight waveguides of the same overall length. The Y–junction structures forming the Mach–Zehnder waveguide configurations were also fabricated individually in order to assess the losses relative to straight guides. The results have been compared to theoretical models of the losses in S–bends and Y–junctions.

The fabrication methods for waveguides and membranes are described. Straight waveguides, Y–junction and Mach–Zehnder waveguide structures were fabricated by both Reactive Ion Etching and wet–chemical etching and a comparison of the propagation characteristics is given. Dry etching was not used for membrane fabrication mainly due to the extensive etching depths required to form membrane structures (several hundred microns). In addition wet–chemical etching was more readily available and better developed for selective etching which allowed greater control over the thickness of the membranes.

Table of Contents

Acknowledgements i
Summary ii
Table of Contents v

Chapter One

Introduction

1.1 General Background 1
1.2 Optical Sensors 1
1.3 Thesis Outline 5
References

Chapter Two

Analysis of Optical Waveguides in GaAs

2.1 Introduction 8
2.2 The Control of Refractive Index in GaAs 8
2.2.1 Free Carrier Concentration 8
2.2.2 Material Composition 10
2.3 One-dimensional Slab Waveguides 12
2.3.1 Maxwell's Equations 12
2.3.2 Dispersion Relations 14
2.3.3 Power Distribution in a Slab Waveguide 15
2.4 Two-dimensional Channel Waveguides 18
2.4.1 Numerical Techniques 19
2.4.2 The Effective Index Method 21
2.5 S-Bend Waveguides 25
2.5.1 Mathematical Formalism 25
2.5.2 Numerical Evaluation 27
2.6 Y-Junction Model 29
2.6.1 Mathematical Basis 30
2.6.2 Transmission, Reflection and Scattering Coefficients 31
2.6.3 Numerical Evaluation 33
2.7 Mach-Zehnder Interferometer 35
2.7.1 Device Operation 35
2.7.2 Device Parameters 38
2.8 Summary 39

Appendix A 41
Appendix B 41
Appendix C 42
References 43

Chapter Three

Mathematical Theory of Elasticity applied to Thin Plates

3.1 Introduction 46
3.2 Membrane Coordinate System 47

3.3 Strain-Displacement Relations 48
3.4 Stress-Strain Relations 51
3.5 Equilibrium Relations 54
3.6 Boundary Conditions 55
3.7 Elliptical Solution of Lagrange's Equation 56
3.8 Photoelastic Effect 57
3.8.1 Phase Shifts due to Changes in Refractive Index 58
3.8.2 Phase Shifts due to Changes in Path Length 63
3.9 Numerical Evaluation 64
3.9.1 Membrane for the Mach-Zehnder Pressure Sensor 65
3.9.2 Membrane for the Birefringent Pressure Sensor 66
3.10 Summary 67

Appendix A 69
References 70

Chapter Four

Device Fabrication by Wet and Dry Chemical Etching

4.1 Introduction 71
4.2 Chemical Etchant Systems for GaAs/AlGaAs 71
4.2.1 Wet Chemical Etching 72
4.2.2 Dry Chemical Etching 74
4.3 Material Preparation 75
4.3.1 GaAs/AlGaAs Epitaxial Layers 75
4.3.2 Wafer Cleavage Planes 75
4.3.3 Wafer Thickness Assessment 76
4.3.4 Sample Cleaning prior to Photolithography 77
4.3.5 Differentiating Between <011> and <01$\bar{1}$> Directions 77
4.4 Waveguide Fabrication 79
4.4.1 Wet Chemically Etched waveguides 79
4.4.2 Reactive Ion Etched waveguides 80
4.5 Membrane Fabrication 81
4.6 Waveguide/Membrane Alignment 84
4.7 Summary 85

Appendix A 86
Appendix B 86
Appendix C 87
Appendix D 88
References 90

Chapter Five

Experimental Results and Interpretations

5.1 Introduction 92
5.2 Deflection-Pressure Tests 92
5.2.1 Objectives 92
5.2.2 Experimental Procedure 92
5.2.3 Discussion of Results 94
5.3 Straight Waveguide Observations 95
5.3.1 Objectives 95
5.3.2 Experimental Procedure 95
5.3.3 Results 96
5.4 Y-Junction Analysis 99

5.4.1 Objectives 99
5.4.2 Experimental Procedure 100
5.4.3 Results 100
5.5 Birefringent Pressure Sensor and External Interferometer 103
5.5.1 Objectives 103
5.5.2 Experimental Procedure 103
5.5.3 Results 105
5.6 Addendum 107

References 109

Chapter Six

Conclusions and Suggestions for Further Research

6.1 Conclusions 110
6.2 Further Research 113

References 115

CHAPTER ONE

Introduction

1.1 General Background

In 1969, S.E. Miller coined the phrase 'Integrated Optics'. The 'Optics' part involves the generation and manipulation of light, but what exactly does 'Integrated' mean? Integration, in this case, is the incorporation of a number of optical components in a system in which light is the carrier of information. Information is kept in the form of light all the way to its destination point – ideally all processing (modulation/demodulation and re-direction) should be carried out using only optical components. At present, a great deal of work is currently being carried out in the field of non-linear optics[1] demonstrating that modulation could possibly be carried out by light sources. There are a number of good introductory texts to the field of integrated optics[2–5] which provide the basic mathematics and terminology of the field.

1.2 Optical Sensors

Optical Fibres

The rapid growth rate of the optical fibre sensor field during the late '70s and early '80s led to the demonstration of a large number of devices. Two review articles[6–7], containing some 262 references between them, cover the majority of optical fibre sensor applications. Pressure, magnetic, chemical, rotation and temperature sensors are just a few of some 60 different types of device which have been demonstrated to have sensitivites comparable to or surpassing existing technologies. The devices can be conveniently divided into two groups: amplitude sensors and phase sensors. In a typical sensor

arrangement, a light source (e.g LED or laser) is used to couple light into a fibre in which it is guided to a detector. At some point along its length, the interaction path, the fibre passes through the field to be sensed (e.g a magnetic field) and this alters the amplitude and/or phase of the light. Amplitude changes can be monitored directly by a photodetector, but in the case of phase sensors the devices need to be somewhat more complicated. Firstly, the sources must produce coherent light and secondly the light must be divided into two paths, the lengths of which must not differ by more than the coherence length of the source. One path passes through the region to be monitored while the other, the reference path, ensures that the light experiences no phase changes. The phases of the two paths can then be compared at the detector.

The sensitivity of an optical sensor is dependent on the interaction length and the detection system. In the case of fibres, one can wind the fibre into coils within the region to be sensed and hence increase the overall interaction length, and it is often the case that the sensitivity is quoted 'per unit length'. In addition, the smallest change in amplitude that can be monitored by the photodetection system limits the sensitivity of the device. In order to avoid confusion which may result when detection systems are compared, the sensitivity is given relative to a 10^{-6} radian change[8]. Typical values quoted for a 1m– length of fibre, and assuming a 10^{-6} radians detection limit, are given in Table 1.1[7]:

TABLE 1.1

PARAMETER	POTENTIAL LIMIT
Pressure	10^{-2}Pa
Magnetic field	10^{-9}Tesla
Rotation rate	10^{-2}deg/hr
Temperature	10^{-8}°C

Planar Technology

'Integrated Optical Sensors' is the term which will be used to refer to sensors using light guided in thin planar films e.g exploiting GaAs or $LiNbO_3$ technologies. The aim of these devices is to permit more processing power at the sensor site – a definite trend in the commercial area. Although optical fibre technology has been well established for about a decade, the area of optical sensors in $LiNbO_3$ is relatively new and for GaAs even more so. The demonstration of sensors on $LiNbO_3$ [9–14] includes displacement, temperature and electromagnetic field sensors but none, to the authors knowledge, have been demonstrated in the AlGaAs/GaAs system. The principles on which optical sensing devices operate can often quite easily be achieved in fibres, $LiNbO_3$, GaAs or silicon technologies, but for optoelectronic purposes the lack of devices based on GaAs is possibly due to the present difficulty in obtaining epitaxially grown material.

The comparison of performance between optical fibre sensors and planar waveguide sensors is not a simple one. Optical fibres have the general advantage of increased interaction length but there are two points to note: (i) one must bear in mind that the sensing region may be spatially limited, thus restricting the amount of fibre usable and (ii) if a sensing field gradient is required, geometry considerations are once again important. In both cases, small sensors based on planar wafers may allow measurements to be made in steep field gradient

situations. On the other hand, fibre devices are, in general, more robust than their planar counterparts and can be coated to survive in harsh environments. The advantages and disadvantages are very dependent on (i) the exact nature of the environment in which the sensor is placed, (ii) the required sensitivity, (iii) the phenomenon to be sensed and (iv) whether fast intelligent feed–back at the sensor site is necessary. Before a manufacturer can embark on such a venture, a great deal of research and developement will be necessary to devise an approach which is easily adaptable to a number of sensing areas.

One of the inherent advantages of compound semiconductor based devices is the possibility of monolithic integration[2] i.e placing laser, sensor, plus the electronics for drive, detection and processing, onto one chip. At present no other technology can match such capabilities. There are still a number of problems to overcome, with the most difficult likely to be robust packaging of thin–film devices, a consideration which at present has not received much attention. Many optical sensors are susceptible to a number of other phenomena which may be considered as noise in the system. A badly packaged device may have enhanced sensitivity to noise, thus reducing the overall sensitivity of the device, or may allow corrosive environments to damage the sensor. Much work is required before completely integrated, monolithic chips are readily available, but present efforts are likely to increase the importance of integrated optic devices.

At present, the techniques for growing epitaxial layers on GaAs substrates, for example Metal Organic Chemical Vapour Deposition (MOCVD) or Molecular Beam Epitaxy (MBE), can be quite difficult

and may, in some circumstances, lead to a delay in the supply of requested material. For this reason individual components of the pressure sensor e.g the behaviour of straight waveguides, Y– junction waveguides and membranes were assessed independently before fabricating the complete device.

In the commercial field it is the integration of components to produce devices which is important. Integrated optical devices, e.g fast modulators, are now appearing on the market and commercial interest is growing rapidly. The efforts of integrated electronics, where vast sums of money are spent pushing back its frontiers, will always provide stiff competition for optoelectronics.

1.3 Thesis Outline

Two basic designs for a pressure sensor are given in Fig.1.1. The first, Fig.1.1a– b, consists of a straight ridge optical waveguide traversing a section of a GaAs wafer (shaded region) which has been etched, in a well– defined area from the wafer base, through the substrate, to within approximately 10μm of the top wafer surface. The etched region, which is much thinner than the normal wafer thickness of 400μm, is referred to as a membrane. The second type of device, Fig.1.1c– d, is an advanced version of the former, incorporating a Mach– Zehnder waveguide configuration which has only one arm crossing the membrane. Deflection of the membrane due to a pressure differential across its thickness will lead, via the photoelastic effect, to a phase change in the light crossing the membrane. The Mach– Zehnder arrangement has the advantage that the phase changes caused by pressure are immediately converted into amplitude changes at the output of the device.

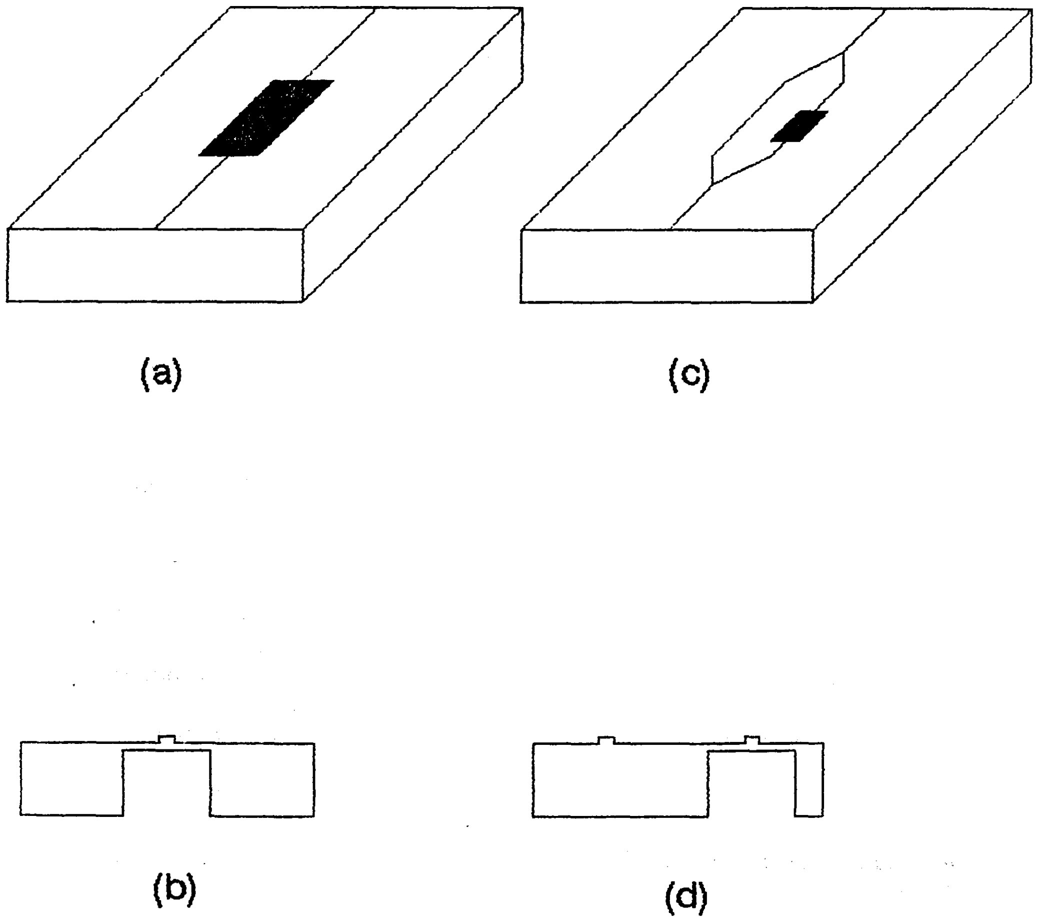

Fig.1.1

Two types of waveguide pressure sensing device where (a) is the birefringent pressure sensor and (c) is the waveguide Mach – Zehnder Interferometric pressure sensor. (b) and (d) are cross – sections through (a) and (c) respectively.

A theoretical description of the characteristics of the optical ridge waveguides is given in Chap.2. Models for the losses in the Y-junctions and S-bends is discussed separately and the overall losses for a Mach-Zehnder waveguide interferometer is aslo presented.

A mathematical theory of elasticity is developed in Chap.3 to predict the deflections of membranes for an applied uniform pressure. The stress-induced changes in refractive index of a membrane due to a pressure differential across its thin dimension allows the phase-shift of guided TE and TM modes on the top surface of the membrane to be calculated.

The actual fabrication techniques for the waveguides and membranes are given in Chap.4. Waveguides were fabricated by both Reactive Ion Etching and wet-chemical etching. But the extensive depths required to form membranes (hundreds of microns), plus the lack of selectivity, ruled out dry etching as a feasible approach.

In Chap.5, a number of experiments related to various aspects of the pressure sensing devices is presented. The results are discussed in relation to the theoretical models which have been developed throughout the thesis.

Finally, the conclusions are given in Chap.6 together with suggestions for future work.

References

[1.1] HOPF, F.A. and STEGEMAN, G.I.:'Applied Classical Electrodynamics – Volume 2: Non-linear Optics', Wiley Series in Pure and Applied Optics, 1985

[1.2] TAMIR, T.:'Integrated Optics', Topics in Applied Physics, **7**, Springer-Verlag, 1979

[1.3] HUNSPERGER, R.G.:'Integrated Optics: Theory and Technology', Springer Series in Optical Sciences, Springer-Verlag, April 1982

[1.4] YARIV, A.:'Optical Electronics', Holt-Saunders International Editions, 1985

[1.5] MARCUSE, D.:'Theory of Dielectric Optical Waveguides', Academic Press, New York, 1974.

[1.6] GIALLORENZI, T.G., BUCARO, J.A., DANDRIDGE, A., SIGEL JR, G.H., COLE, J.H., RASHLEIGH, S.C. and PRIEST, R.G.:'Optical Fiber Sensor Technology', IEEE Journal of Quantum Electronics, **QE-18**, No.4, pp626-665, 1982

[1.7] PITT, G.D., EXTANCE, P., NEAT, R.C., BATCHELDER, D.N., JONES, R.E., BARNETT, J.A. and PRATT, R.H.:'Optical-fibre Sensors', IEE Proceedings, **132**, Pt.J, No.4, pp214-248, 1985.

[1.8] JACKSON, D.A., DANDRIDGE, A. and SHEEM, S.K.:'Measurement of Small Phase Shifts using a Single-mode Optical-fiber Interferometer', Optics Letters, **5**, No.4, pp139-141, 1980

[1.9] IZUTSU, M., ENOKIHARA, A. and SUETA, T.:'Optical-waveguide Micro-displacement Sensor', Electronics Letters, **18**, N0.20, pp867-868, 1982

[1.10] HARUNA, M., NAKAJIMA, H. and NISHIHARA, H.:'Optical π-arc Waveguide Interferometer in Proton-exchanged $LiNbO_3$ for Temperature Sensing', Applied Optics, **24**, No.16, pp2483-2484, 1985

[1.11] BULMER, C.H., MOELLER, R.P. and BURNS, W.K.:'Linear Mach-Zehnder Interferometers in $LiNbO_3$ for Electromagnetic Field Sensing', Proceedings of the 2nd European Conference on Integrated Optics, Florence, pp140-143, 1983

[1.12] IZUTSU, M., ENOKIHARA, A., MEKADA, N. and SUETA, T.:'Optical-waveguide Pressure Sensor', Proceedings of the 2nd European Conference on Integrated Optics, Florence, pp144-147, 1983

[1.13] JOHNSON, L.M. and LEONBERGER, F.J.:'Integrated Optical Temperature Sensor', Applied Physics Letters, **41**, No.2, pp134-136, 1982

[1.14] IZUTSU, M., ENOKIHARA, A. and SUETA, T.:'Integrated Optic Temperature and Humidity Sensors', Journal of Lightwave Technology, **LT-4**, No.7, pp833-836, 1986

CHAPTER TWO

Analysis of Optical Waveguides in GaAs

2.1 Introduction

Accurate modelling of the behaviour of light in a waveguide allows quantities such as power distribution, propagation velocity and power losses to be estimated. For some simple index distributions it is possible to obtain an analytic solution, but the majority of cases require a numerical analysis or a physically intuitive approximation – invariably involving the use of a computer. The models presented in this chapter include ones for straight guides, curved guides and waveguide Y–junctions with numerical examples based on waveguides actually fabricated. The final section brings the models together in order to optimise the characteristics of the Mach–Zehnder interferometer pressure sensor.

2.2 The Control of Refractive Index in GaAs

An optical waveguide is a structure which confines light energy to either one or two dimensions. The most common techniques used for confinement in semiconductors are (a) altering the free–carrier concentration or (b) changing the material composition.

2.2.1 Free Carrier Concentration

Doping a layer of an intrinsic GaAs crystal, either n–type or p–type, causes a reduction in the dielectric constant and hence refractive index. Waveguides formed by epitaxial layers of high resistivity (low–doped) GaAs grown on low resistivity (high–doped) GaAs can be obtained by a number of growth techniques including Metal Organic Chemical Vapour Deposition, MOCVD, and Molecular Beam

Epitaxy, MBE. Guiding can also be achieved by utilising the carrier–free depletion region between an n–type and p–type layer[1].

In semiconductors, the change in refractive index is given by[2]:

$$\Delta n_S = -\frac{N\lambda_0^2 e^2}{\epsilon_0 n_S 8\pi^2 m^* c^2} \qquad 2.1$$

where

N : free–carrier concentration
n_S: refractive index of the intrinsic semiconductor
λ_0: wavelength of light in vacuum
e : free–carrier charge
ϵ_0: permittivity of vacuum
c : speed of light in vacuum
m^*: effective mass of the free carriers

At a wavelength of 1.3μm and for a relatively high free–carrier concentration of 10^{18} cm^{-3}, $\Delta n_S \simeq 0.003$. Holes have ten times the effective mass of an electron ($m_h^* = 10m_e^* \triangleq 0.7m_e$)[3] and hence, for a given carrier concentration, produce a smaller index reduction.

The presence of free carriers, however, leads to optical absorption[4] as well as a reduction in the refractive index – the two processes being inseparable. At a wavelength of about 1μm, Rashevskaya and Fistul[4] measured losses of 20dB/cm for free carrier concentrations of 10^{18}cm^{-3}. However, if an intrinsic GaAs layer is grown on a doped substrate, the losses only occur in the evanescent tail of the guided modes. High substrate doping increases the refractive index difference between the guiding layer and the substrate, which in turn means that the mode becomes more tightly confined. Confinement can also be increased by using thicker guiding layers[5]. Thus, less light travels in the more lossy substrate, leading to a trade–off between

loss and confinement.

2.2.2 Material Composition

When altering the material composition of GaAs to form an optical waveguide the aim is to do so with as little crystal damage, or distortion, as possible. Dislocations and strains can result in unnecessary optical absorption. Either diffusion or epitaxial growth is used to change the refractive index of the GaAs zinc blende structure, the latter being favoured since it allows more control over the index profile. Various group III or V elements can be incorporated into the GaAs crystal substituting at either the gallium or arsenic sites. Examples of ternary compounds include $Al_xGa_{1-x}As$, $In_xGa_{1-x}As$ and $GaAs_{1-x}Sb_x$ and there are also the quaternary compounds e.g GaInAsP. Although the number of combinations is large, two parameters restrict choice – the lattice constant of the binary components (GaAs, AlAs etc) and the position of the band edge of the composite material. The lattice constant is a measure of the interatomic separation of a compound. The lattice constants of GaAs and AlAs are 5.64Å and 5.66Å respectively while that for InAs is 6.06Å [6]. Thus the strain in $Al_xGa_{1-x}As$ will typically be much less than that for $In_xGa_{1-x}As$ and there will be far fewer dislocations per unit area. The band edge of AlAs is at 580nm (corresponding to an energy gap of 2.14eV) while that for InAs is at 3.4μm [4] (0.37eV). With the GaAs edge at 870nm (1.43eV) one might expect that the addition of indium to the crystal lattice will, in general, produce a red–shift (shift to longer wavelengths) in the band edge while aluminium content produces a blue–shift [7].

The availability of good quality epitaxial layers of AlGaAs, plus the

existence of infra-red HeNe and semiconductor lasers with which the fabricated waveguides can be analysed, makes it an obvious choice for this project. In addition, AlGaAs/GaAs is the most established for wet-chemical etching properties, Chap.4. As mentioned above, the partial substitution of aluminum in GaAs moves the band edge from 870nm to shorter wavelengths which means that waveguide analysis with wavelengths greater than 1 μm does not require a detailed knowledege of the absorption edge as a function of aluminium concentration. However, the change of refractive index as a function of aluminium content is an important consideration. The variation of the refractive index of $Al_xGa_{1-x}As$ is given by the Sellmeir equation[8] which is based on a fit to experimental data:

$$n(x) = A + 2.92x + \frac{B}{\lambda_0^2 - C(x)} - D(x)\lambda_0^2 \qquad 2.2$$

where for GaAs:

λ_0: operating wavelength (μm)

$A = 10.906$

$B = 0.97501$

$C = (0.52886-0.735x)^2 \qquad x \leq 0.36$

$\;\; = (0.30386-0.105x)^2 \qquad x \geq 0.36$

$D = 0.002467(1.41x+1)$

Typical values, calculated using the Sellmeir equation, are given in Table 2.1 for wavelengths of 1.15μm and 1.3μm.

TABLE 2.1

WAVELENGTH (μm)	GaAs	$Al_{0.1}Ga_{0.9}As$	AlAs
1.15	3.4406	3.3889	2.9560
1.30	3.4049	3.3566	2.9269

A 10% Al content in GaAs changes the refractive index by $\Delta n \simeq 0.05$. The refractive index changes produced by partial substitution of aluminium into GaAs is thus much larger than that achievable by altering the free carrier concentraion, Sec.2.2.1, without the same

levels of loss. At the time of writing, a ±2% accuracy on the aluminium concentration in a layer, which corresponds to $\Delta n \simeq 0.01$, is achievable using MOCVD.

2.3 One-dimensional Slab Waveguides

2.3.1 Maxwell's Equations

Maxwell's equations for an isotropic, homogeneous, source free medium are as follows:

$$\underline{\nabla} \cdot \varepsilon\underline{E} = 0 \qquad 2.3$$

$$\underline{\nabla} \cdot \mu\underline{H} = 0 \qquad 2.4$$

$$\underline{\nabla} \wedge \underline{E} = -\mu \frac{\partial \underline{H}}{\partial t} \qquad 2.5$$

$$\underline{\nabla} \wedge \underline{H} = \varepsilon \frac{\partial \underline{E}}{\partial t} \qquad 2.6$$

where:

$\underline{E}$ and $\underline{H}$: Electric and magnetic field vectors

ε and μ : Permittivity and permeability of the medium

It is assumed that the solutions to Eqns.2.3-6 are harmonic, single frequency waves travelling in the z direction, and have a form given by:

$$\underline{E} = \underline{E}(x,y)e^{i(\omega t - \beta z)} \qquad 2.7$$

$$\underline{H} = \underline{H}(x,y)e^{i(\omega t - \beta z)} \qquad 2.8$$

where:

ω: radian frequency

β: propagation constant is real for a lossless medium

Combining Maxwell's equations leads to the wave equation:

$$\nabla^2\underline{E}(x,y) + \omega^2\mu\varepsilon\underline{E}(x,y) = 0 \qquad 2.9$$

This equation or its magnetic equivalent forms the basis for all

modelling of waveguides. It is the boundary conditions present in the medium which dictate the exact form of the solution.

The waveguides throughout this thesis are fabricated using non-magnetic media and hence $\mu = \mu_0$ where μ_0 is the permeability of free space. In addition, for lossless media $\varepsilon = \varepsilon_0 \varepsilon_r = \varepsilon_0 n^2$ where n is a real number representing the refractive index of the medium and ε_0 is the permittivity of free space.

The one dimensional slab waveguide is the simplest to model and analytic solutions can readily be obtained. A detailed analysis is given in standard texts[6] but an overview is described here. Fig.2.1 shows schematically the fundamental parameters of a single layer slab.

Fig.2.1

Two self-consistent types of solution exist for the slab guide, where $\partial/\partial y = 0$. The first is referred to as transverse electric (TE), since there is no component of the electric field in the direction of propagation. Its finite components are E_y, H_x and H_z. The second type of solution contains only H_y, E_x, and E_z and is referred to as a TM wave. Assuming solutions to Eqn.2.9 of the form given in Eqn.2.7 leads to the wave equation for TE modes.

$$\frac{\partial^2 E_y}{\partial x^2} + (n^2 k_0^2 - \beta^2) E_y = 0 \qquad 2.10$$

where:

$$k_0^2 = \mu_0 \varepsilon_0 \omega^2.$$

The corresponding wave equation for TM modes is given by:

$$n^2 \frac{\partial}{\partial x}\left[\frac{1}{n^2}\frac{\partial H_y}{\partial x}\right] + (n^2k_0^2-\beta^2)H_y = 0 \qquad 2.11$$

If n is constant within each layer, Eqn.2.11 reduces to the same form as Eqn.2.10, where $\psi = E_y$ or H_y:

$$\frac{\partial^2\psi_y}{\partial x^2} + (n^2k_0^2-\beta^2)\psi_y = 0 \qquad 2.12$$

For non–magnetic media, Maxwell's equations require all magnetic field components to be continuous across boundaries. But in the case of electric fields, the tangential components and the perpendicular displacement components are continuous across boundaries. Only this difference in boundary conditions distinguishes between the TE modes, E_y, and the TM modes, H_y. For the TE modes, E_y and $\partial E_y/\partial x$ are continuous across a boundary whereas, for TM modes H_y, and $(1/n^2)\partial H_y/\partial x$ are continuous.

2.3.2 Dispersion Relations

Applying the boundary conditions to Eqn.2.12 for guided modes in the structure shown in Fig.2.1 leads to the dispersion relations which contain all the parameters required to define the behaviour of light in the slab:

$$\kappa t = \varphi_s + \varphi_c + \Pi\nu \qquad \nu = 0,1,2... \qquad 2.13$$

where:

$$\kappa = ((n_f k_0)^2-\beta^2)^{\frac{1}{2}} \qquad 2.14$$

$$\gamma_s = (\beta^2-(n_s k_0)^2)^{\frac{1}{2}} \qquad 2.15$$

$$\gamma_c = (\beta^2-(n_c k_0)^2)^{\frac{1}{2}} \qquad 2.16$$

For TE modes:

$$\varphi_s = \tan^{-1}\left[\frac{\gamma_s}{\kappa}\right], \qquad \varphi_c = \tan^{-1}\left[\frac{\gamma_c}{\kappa}\right] \qquad 2.17$$

and for TM modes:

$$\varphi_s = \tan^{-1}\left[\frac{n_f^2\gamma_s}{n_s^2\kappa}\right], \qquad \varphi_c = \tan^{-1}\left[\frac{n_f^2\gamma_c}{n_s^2\kappa}\right] \qquad 2.18$$

Eqn.2.13 is a transcendental equation which can be solved for β using standard techniques. The guided mode solutions are discrete ($\nu=0,1,2...$) where $\nu=0$ gives the propagation constant of the fundamental mode. The propagation constants of all the guided modes must lie in the range $n_s k_0 < \beta < n_f k_0$ or, equivalently, $n_s < N < n_f$ where N is the effective index of the guide. For the above notation, the forms of the function, γ= E or H, within each layer is given by Fig.2.2:

x

λ_0 vacuum wavelength

	$\psi_y = \psi_c \exp(-\gamma_c(x-t))$	$\beta > n_c k_0$
x = t	$\psi_y = \psi_f \cos(\kappa x - \varphi_s)$	$\beta < n_f k_0$
x = 0	$\psi_y = \psi_s \exp(\gamma_s x)$	$\beta > n_s k_0$

>y

Fig.2.2

2.3.3 Power Distribution in a Slab Waveguide

In the AlGaAs/GaAs system the layers are grown on a GaAs substrate as indicated in Fig.2.3:

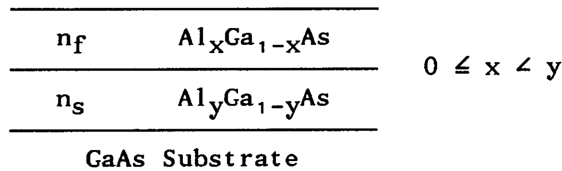

Fig.2.3

It is important to be able to calculate the power distribution in the layers in order to select the thickness of layer n_s which minimises the

penetration of the evanescent tail of the guided mode into the GaAs substrate, where the light is lost.

The distribution of power between layers is calculated for TM modes but the procedure is similar for TE.

x		λ_0 vacuum wavelength
	$H_y = H_c \exp(-\gamma_c (x-t))$	n_c
x = t		
	$H_y = H_f \cos(\kappa x - \varphi_s)$	n_f
x = 0	→y	
	$H_y = H_s \exp(\gamma_s x)$	n_s

Fig.2.4

The flow of power carried by an electromagnetic wave through a plane of constant z is given by the Poynting vector, $\underline{S}$:

$$\underline{S} = \mathrm{Re}\int_{-\infty}^{\infty}\int_{-\infty}^{\infty} \underline{E} \times \underline{H}^* \, dxdy \qquad 2.19$$

For a TM mode propagating in the slab of Fig.2.4, the Poynting vector can be expressed as the power per unit length:

$$S_z = \frac{1}{2} \mathrm{Re}\int_{-\infty}^{\infty} H_y E_x^* dx \qquad 2.20$$

Maxwell's equations, which relate the magnetic and electric field components, can be used in conjunction with Eqns.2.7–8 to express E_x in terms of H_y. The integral in Eqn.2.20 must be carried out for each layer to give the power in the guiding layer, P_f, the substrate, P_s and cover, P_c,:

$$P = P_c + P_f + P_s \qquad 2.21$$

where:

$$P_c = \frac{N k_0 H_c^2}{4\omega\varepsilon_0 n_c^2} \frac{1}{\gamma_c} \qquad 2.22$$

$$P_f = \frac{Nk_0H_c^2}{2\omega\varepsilon_0 n_f^2}\left[\frac{t}{2} + \frac{1}{4\kappa}\{\sin[2(\kappa t-\varphi_s)] + \sin(2\varphi_s)\}\right] \qquad 2.23$$

$$P_s = \frac{Nk_0H_s^2}{4\omega\varepsilon_0 n_s^2}\frac{1}{\gamma_s} \qquad 2.24$$

The boundary conditions in Fig.2.4 allow the field amplitudes H_c and H_s to be expressed in terms of H_f:

$$\frac{H_{s/c}^2}{n_{s/c}^2} = \frac{H_f^2}{n_f^2}\left[\frac{\kappa^2}{\gamma_{s/c}^2 + \left[\frac{n_{s/c}k_0}{n_f}\right]^2}\right] \qquad 2.25$$

Substitution of Eqn.2.25 into each of Eqns.2.22–24 and dividing by the total power, P, gives the relative power in each layer in terms of the refractive indices and thickness of the slab. One can also calculate $1/\gamma_s$ which represents the distance, into the substrate, from the film/substrate interface where the field intensity falls to e^{-1}. Fig.2.5 contains parameters for one of the epitaxial layers grown by MOCVD. The etch stop layer is incorporated into the structure for the purposes of membrane fabrication and ideally the mode should be unaffected by its presence. When the $Al_{0.08}Ga_{0.92}As$ layer is assumed infinitely thick, $1/\gamma_s$ for the fundamental TE mode is 0.6μm. Thus, the intensity at the position of the etch stop is 1/100 of the value at the $GaAs/Al_{0.08}Ga_{0.92}As$ interface.

Air		
GaAs	1.2μm	
$Al_{0.08}Ga_{0.92}As$	2.5μm	
$Al_{0.60}Ga_{0.40}As$	3.0μm	Etch Stop
GaAs Substrate		

Fig.2.5

2.4 Two–dimensional Channel Waveguides

For one–dimensional slab waveguides, TE and TM modes are natural solutions to Maxwell's equations. This terminology is often carried over to two–dimensional guides but it is not strictly correct. In scalar numerical analyses of waveguides, quasi–TE and TM mode solutions are assumed where the respective electric and magnetic field components in the direction of propagation are assumed small compared to the transverse components. To overcome this particular problem requires a full vector analysis[9] which is very difficult to implement and requires a great deal of computer time to find solutions, even when using the fastest commercially available minicomputers. In Sec.2.4.1, the main principles of two scalar techniques are described, but there are a number of other methods including finite element methods[10], the beam propagation method[11] and mode–matching techniques[12–13] which the reader will find useful for obtaining further literature on many aspects of waveguide analysis as well as useful comparisons of the various methods.

One finds that many of the complex problems involving two–dimensional analysis can be approximated by a simpler one–dimensional approach which yields useful information about the

structures[17-18]. In Sec.2.4.2 one such method, 'the effective index method' will be described.

2.4.1 Numerical Techniques

Scalar Variational Analysis

This method solves Eqn.2.9 by taking advantage of the variational properties of the modal propagation constant, β, which is expressed by the Rayleigh Quotient[14]:

$$\beta^2 \geq \frac{\iint_{-\infty}^{\infty}\{k_0^2 n^2(x,y)\,|\psi_t(x,y)|^2 - |\nabla_t\psi|^2\}dxdy}{\iint_{-\infty}^{\infty}|\psi_t|^2\, dxdy} \qquad 2.26$$

where:

k_0 : wavenumber of the light in vacuum

$n(x,y)$: value of refractive index at the point (x,y)

ψ_t is a trial field i.e a summation of orthogonal functions whose resultant form is required to match that of the true modal function as closely as possible. The trial functions have a number of parameters whose values can be changed to alter the functional form. Variational methods rely on the fact that the correct modal function, for a given index distribution, and boundary conditions, will place β at its maximum value. One should add that the maximum value of β provides only the best modal fit that the particular trial function can generate. Thus, judicious choice of trial functions is essential if good approximations to the propagation constant and mode field are to be calculated. Examples of trial function families include parabolic cylinder functions[15] and Hermite-Guassian functions. A variational method using Hermite-Guassian trial functions has been developed at Glasgow University by Prof. C.D.W and Dr. J.A.H. Wilkinson which

has since been modified by Dr. R.G. Walker, Plessey Research (Caswell) Ltd to deal with step-index stripe waveguides. The characteristics of the program have been extensively studied by Dr. M. Mac Bean[16].

Finite Difference Method

For quasi-TE modes, the wave equation (Eqn.2.9) can be written:

$$\frac{\partial^2 E(x,y)}{\partial x^2} + \frac{\partial^2 E(x,y)}{\partial y^2} + (\omega^2\mu\varepsilon-\beta^2)E(x,y) = 0 \qquad 2.27$$

In the Finite Difference Method, the waveguide cross-section is divided into a large number of mesh points each of which is labelled with a refractive index and an electric field value depending on its position, hence forming two matrices n(I,J) and E(I,J) where IxJ is the number of mesh points. Eqn.2.9 is evaluated by considering the gradients between neighbouring points:

$$\frac{\partial^2 E_y}{\partial x^2} = \frac{E(I+1,J)+E(I-1,J)-2E(I,J)}{(\Delta x)^2} \qquad 2.28$$

$$\frac{\partial^2 E_y}{\partial y^2} = \frac{E(I,J+1)+E(I,J-1)-2E(I,J)}{(\Delta y)^2} \qquad 2.29$$

where Δx and Δy are the distances between neighbouring points in the x and y directions. Substituting Eqns.2.28-29 into Eqn.2.27 and rearranging for E(I,J) gives:

$$E(I,J) = \frac{E(I+1,J)+E(I-1,J)+R^2\{E(I,J+1)+E(I,J-1)\}}{2(1+R^2) - k_0^2(\Delta x)^2\{n^2(I,J)-N^2\}} \qquad 2.30$$

where $R = \Delta x/\Delta y$.

A typical program can begin with an arbitrary field distribution

E(I,J), which is integrated using the variational expression, Eqn.2.26, to provide the first estimate of the effective index $N=\beta/k_0$ which can, in turn, be used to modify the electric field distribution in Eqn.2.30. The iteration is repeated until E and N have converged to the final values determined by the required accuracy.

Computing Time versus Accuracy

In both methods described above the normal procedure is to encase the cross-sectional area of the waveguide in a larger region where the field is assumed to fall to zero at the boundary. Because there are always limitations on computing time, there is a corresponding limit on the number of mesh points used to define the cross-section and, in the case of variational method the number of orthogonal trial functions that can be used. If fields at the boundary have fallen to a sufficiently low value, then any perturbation to the position of the boundary should result in very little change in the propagation characteristics or the mode profile. In addition, alteration to the density of mesh points, or the number of trial functions used, should have no effect on the propagation characteristics. Determining the optimum values for all these parameters can be a very time consuming task.

2.4.2 The Effective Index Method

The numerical methods described in the last section, if carefully formulated, are only limited in accuracy by the computation time, which can, in some cases, be quite extensive. For this reason, methods, more intuitive than analytical, have evolved which can provide information about structures without resort to exhaustive calculations[17]. The results may then be compared to those acquired

through numerical analyses and the weaknesses are noted and taken into account. One such technique is the 'effective index method', which has been compared to many other methods in the past[18]. The method is quite simple only requiring knowledge about slab waveguides, but the information it supplies is very limited. Unlike many of the numerical techniques, there is no way to retrieve the final mode profile of the waveguide structure. It is suited to rectangular ridge structures like that shown in Fig.2.6:

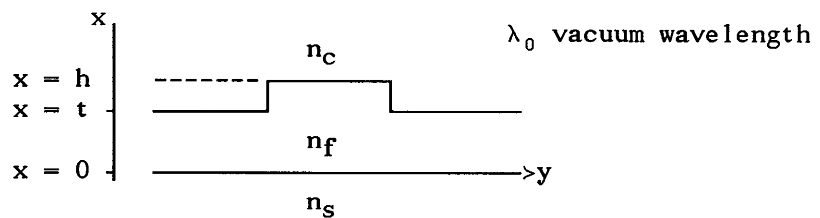

Fig.2.6

The procedure for applying the effective index method for a TE mode in this ridge structure (considered to be a single-mode guide), is now outlined. The guide is first divided into the three slabs in Fig.2.7:

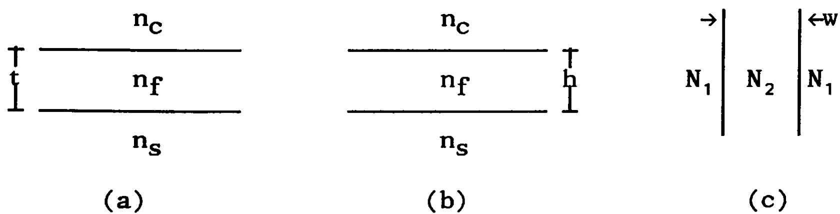

Fig.2.7

The propagation constant of the fundamental TE mode, N_1, is calculated for the slab in Fig.2.7a (TE implies that the electric field is parallel to the layer boundaries). The same procedure is applied for that in Fig.2.7b, giving N_2. To obtain the propagation constant and confinement in the y-direction, the ridge is represented by the slab in Fig.2.7c using the previously calculated effective indices N_1

and N_2. This final effective index, N, which must be calculated for TM (the electric field is now perpendicular to the layer boundaries), is taken as the effective index of the ridge waveguide.

Care must be exercised when applying and interpreting the information supplied by the effective index method. For asymmetric guides it is possible for the outer slab of thickness t to be below cut–off and thus N_1 cannot be calculated, but this certainly does not imply that the whole ridge structure is below cut–off. N_1 is often substituted by the substrate index in order to continue with the calculations when the inner slab, of thickness h, is above cut–off. The second problem arises when the inner and/or outer slabs support more than one guided mode. Under these circumstances the logical procedure would be to calculate all combinations of inner and outer indices and label the modes starting with that of the highest effective index as the fundamental mode. The author has not seen any evidence of this continuation in the literature, which usually restricts itself to the single–mode regime of the analysis. For regions where $h-t \ll t$ and the slab modes are far from cut–off the effective index method proves very useful for obtaining propagation characteristics. In addition, any ridge structure found to just reach cut–off will, according to numerical analyses[18], still support a guided mode.

Apart from these difficulties, the effective index method is a useful and yet simple technique which provides propagation characteristics and trends for analysing complicated structrures. The method will be applied to curved guides and Y–junctions in the following two sections which would otherwise be extremely difficult to analyse and understand.

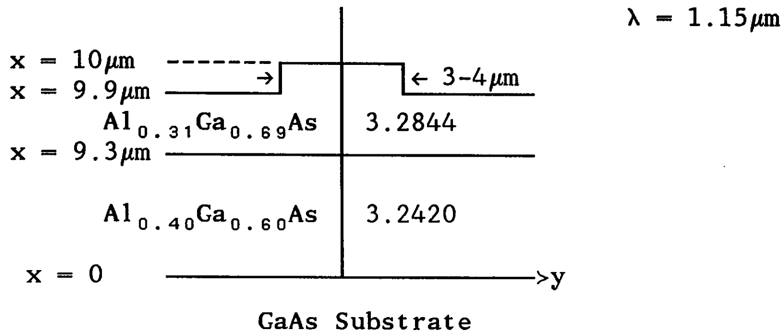

Fig.2.8

TABLE 2.2

RIDGE WIDTH (μm)	MODE	N_{eff}	$1/\gamma_s$ (μm)	P.R (%)
3	0	3.24728	1.44	97
4	0	3.24778	1.31	98
4	1	3.24497	5.35	91

Table 2.2 shows values calculated for $3\mu m$ and $4\mu m$ wide ridges for the structure in Fig.2.8 using the effective index method. The $3\mu m$ wide guide is single-mode while that of $4\mu m$ supports two modes. If the intensity at $y = \pm\frac{1}{2}$(Ridge width) is given by I_0 then at $y = y_g$ (where $y_g = \pm\{\frac{1}{2}\text{Ridge width} + 1/\gamma_s\}$) it has fallen to $I_0 e^{-1}$. The P.R value represents the percentage of light which travels in the region defined by $|y| < y_g$. For the $4\mu m$ wide guide, the mode is thus considered to be spread over $4 + 2\text{x}1.31 = 6.62\mu m$ and this region carries 97% of the power in the wave. On the other hand the first asymmetric mode of the $4\mu m$ wide guide is more weakly confined and is spread over $14.7\mu m$ carrying 91% of the power in this region. In the following section, the confinement factor indicated here is shown to play an important role in interpreting the loss experienced by guided modes in the curved sections of a waveguide.

2.5 S- Bend Waveguides

Understanding the losses due to curved waveguides is an important feature of integrated optic design. Complex methods have been developed for their analysis[19-21] and a great deal of experimental work has been carried out[22-25]. The Mach- Zehnder pressure sensor, Fig.1.1, proposed in this thesis uses S- bends to form the Y- junctions. Fig.2.9 shows the parameters involved with an S- bend Y- junction structure. The S- bends were initially designed with 40mm radii of curvature sections providing a 300μm separation between the Mach- Zehnder interferometer arms. In this section the transmission P_{out}/P_{in}, for one S- bend (ignoring the Y- junction) is calculated by integrating the loss per unit length of a curved section of waveguide over the length of the S- bend. This recent study indicates that the 40mm radius of curvature, for which experimental studies have already been carried out, can be greatly reduced.

2.5.1 Mathematical Formalism

The analysis developed by Marcatilli and Miller[26] leads to a simple expression for the loss experienced by modes in curved sections of waveguides as a function of the radius of curvature. Minford et al[27] have more recently extended the formalism to cope with Ti:LiNbO$_3$ waveguide bends and have obtained good experimental agreement. Due to the generally unfamiliar concept, the mathematical model will be detailed at some points. The waveguide considered is a one- dimensional slab with a radius of curvature R, Fig.2.10.

The guided light travels with a velocity c/N where N is the effective index of the slab, and $N_1 < N < N_1$. For a curved waveguide, a distance x_r exists where the light must travel at c/N_1 in order to

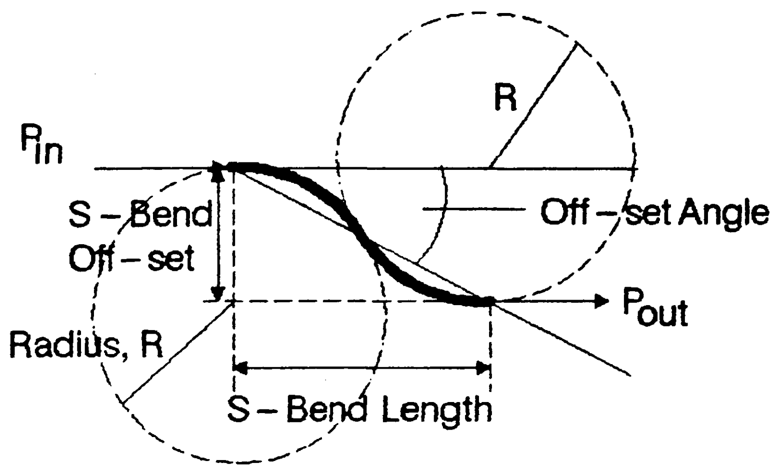

Fig.2.9

S – bend parameters

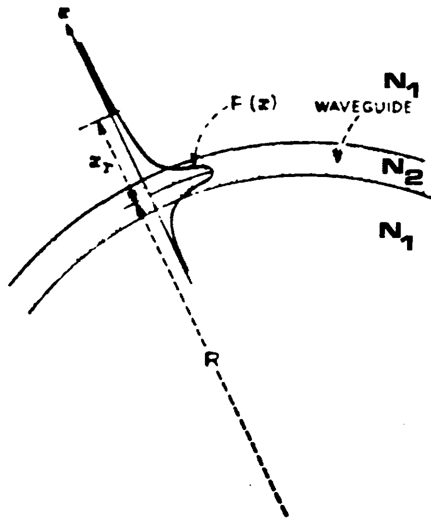

Fig.2.10

Curved Slab Waveguide

maintain a constant wavefront. Beyond this distance, $x > x_r$, the light energy in this region would have to travel faster than the speed of light to keep up with the remainder of the light in $x \leq x_r$. So, in the current framework, this light is assumed to be radiated. The distance x_r is given by:

$$k_0 N R d\varphi \geq N_1 k_0 (R + x_r) d\varphi$$

leading to:

$$x_r = \frac{(N - N_1)}{N_1} R \qquad 2.31$$

Denoting the energy in the region $x > x_r$ as ε_l and the total energy carried by the mode as ε_T, the fraction of energy lost is given by $\varepsilon_l / \varepsilon_T$.

In an infinite uniform medium, light energy of wavelength λ/N_1 remains collimated for a distance given by:

$$Z_c = \frac{(\text{transverse field width})^2}{2 \times \text{wavelength}} = \frac{a^2 N_1}{2\lambda_0} \qquad 2.32$$

Assuming an approximate distance Z_c required for energy to flow out from the guided field of the same width 'a' and a power decay rate $e^{-2\alpha z} \simeq 1 - 2\alpha z$, the fractional powerloss is:

$$\frac{\varepsilon_l}{\varepsilon_T} = 2\alpha z \quad \equiv \quad \alpha = \frac{1}{2Z_c} \cdot \frac{\varepsilon_l}{\varepsilon_T} \qquad 2.33$$

The exact forms of ε_l and ε_T are given in Appendix A.

The effective transverse field width is simply given by:

$$a = w + 2/\gamma_s \qquad 2.34$$

which, when substituted in Eqn.2.32 leads to:

$$Z_c = \left[\frac{w+2/\gamma_s}{2(\lambda/N_1)}\right]^2 \qquad 2.35$$

Eqn.A.1−2 in Appendix A and Eqns.2.34−35 substituted into Eqn.2.33 provides the loss, α, as a function of radius, R:

$$\alpha(R) = C_1 \exp(-C_2 R) \qquad 2.36$$

where:

$$C_1 = \frac{1}{2Z_c}\frac{\varepsilon_1'}{\varepsilon_T} \qquad 2.37$$

$$C_2 = \frac{k_0[2(N-N_1)]^{3/2}}{\surd N_1} \qquad 2.38$$

$$\varepsilon_1' = \varepsilon_1 \exp(2\gamma_s x_r) \qquad 2.39$$

The calculations for the loss per unit length along a curved waveguide have now been derived. A numerical example is now given to provide the magnitude of the loss likely to be experienced by S−bend waveguides fabricated in this project.

2.5.2 Numerical Evaluation

A numerical analysis is now presented for the ridge structure shown in Fig.2.8 and the S−bend parameters are indicated in Fig.2.9. The effective index method is used to convert the two−dimensional ridge waveguide into a slab waveguide as described in Sec.2.4.2.

Fig.2.11a−b are plots of the S−bend length and Offset angle based on the simple geometrical relationships:

$$\text{Length, } L = 2(O \times R - (\tfrac{1}{2}O)^2)^{\frac{1}{2}} \qquad 2.40$$

$$\text{Offset angle} = \tan^{-1}(O/L) \qquad 2.41$$

where: L is the S−bend length, O is the S−bend offset and R the radius of curvature of the curved sections. For the initial Mach−Zehnder design, an offset angle of 150μm with 40mm radii of

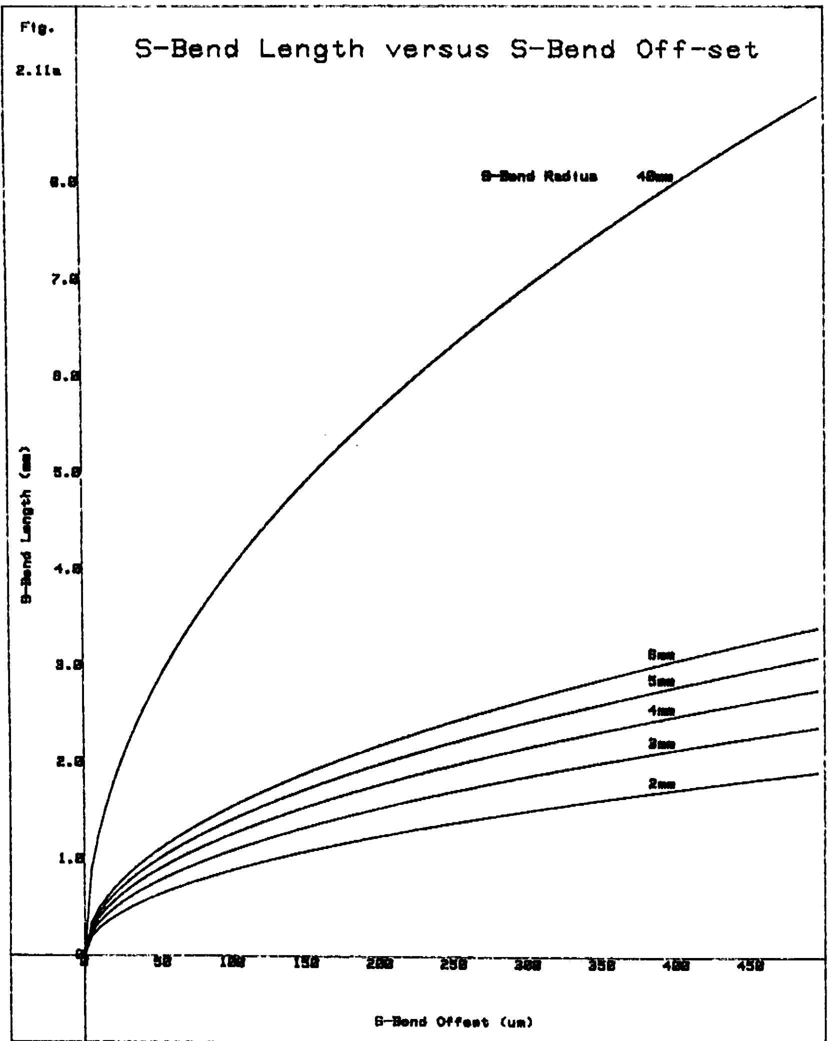
Fig.
2.11a
S-Bend Length versus S-Bend Off-set
S-Bend Radius
40mm
6mm
5mm
4mm
3mm
2mm
8.0
7.0
6.0
5.0
4.0
3.0
2.0
1.0
0
S-Bend Length (mm)
50
100
150
200
250
300
350
400
450
S-Bend Offset (um)

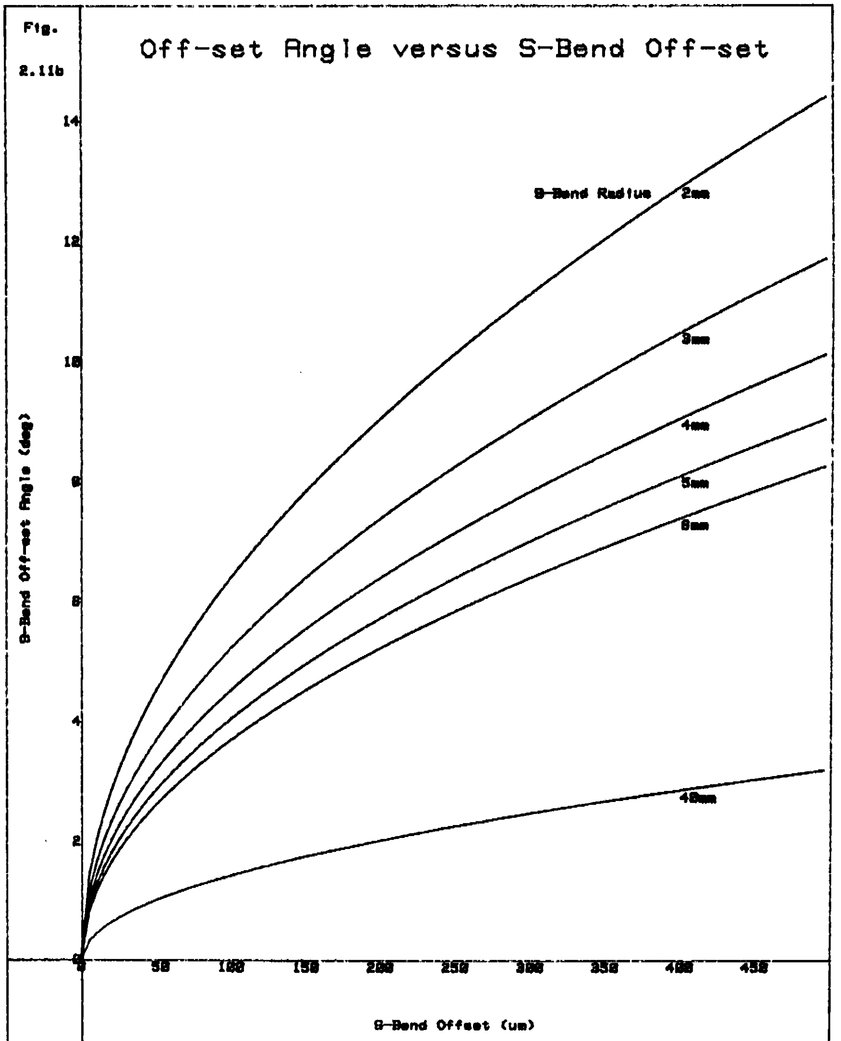
Fig.
2.11b
Off-set Angle versus S-Bend Off-set
S-Bend Radius
2mm
3mm
4mm
5mm
6mm
40mm
14
12
10
8
6
4
2
0
S-Bend Off-set Angle (deg)
50
100
150
200
250
300
350
400
450
S-Bend Offset (um)

curvature was chosen, based on an intuitive desire to keep the offset angle around 0.5°. Since there are two S-bend Y-junctions in a single Mach-Zehnder waveguide (input and output), the overall length of the Y-junction is around 10mm. This length does not include the straight section of the input, output and arms of the structure. Reducing the radius of curvature to 6mm results in a total S-bend length reduction to just 4mm. The important question to bear in mind is: How do the inevitable losses in the S-bends vary with the radius of curvature?

Fig.2.12 gives some idea of the complexity of the problem. For a 0.1 μm etch depth, Fig.2.12a, a 150 μm offset has a transmission very close to 100% for a 40mm radius of curvature, but when the radius is reduced to 5-6mm, the transmission is still very high (about 90%). Calculations carried out for a 0.2 μm etch depth, Fig.2.12b, show a very different picture. The extra etching provides more confinement for the guided mode and hence even smaller radii of curvature are negotiable. In the latter case, a 150 μm offset now gives 90% transmission for a radius of 2mm. The total S-bend length is reduced to just 2mm. Mode confinement can also be increased by fabricating wider ridge waveguides. Fig.2.12c shows the variation of transmission with ridge width for a 0.1 μm etch. However, increasing the etch depth reduces the number of guided lateral modes while increasing the ridge width increases the number of modes. Single mode guides are crucial to Mach-Zehnder interferometric operation, Sec.2.7, so it is safer to vary the etch depth of the ridge. As the etch depth is increased the modes experience scattering losses from the ridge walls and this is likely to be the limiting factor for high ridges with small radii of curvature[28].

Fig. 2.12a

Transmission:3um Ridge Width,0.1um Etch

S-Bend Radius: 8mm, 5mm, 4mm, 3mm, 2mm

S-Bend Transmission (0 – 1.0)

S-Bend Offset (um) (0 – 450)

Fig. 2.12b

Transmission:3um Ridge Width,0.2um Etch

S-Bend Radius: 2.5mm, 2mm, 1.5mm, 1mm

S-Bend Transmission (0 – 1.0)

S-Bend Offset (um) (0 – 450)

Fig. 2.12c

Transmission:5mm S-Bend Radii,.1um Etch

Ridge Width: 4um, 3um, 2um

S-Bend Transmission (0 – 1.0)

S-Bend Offset (um) (0 – 450)

2.6 Y– Junction Model

Theoretical models for both symmetric and asymmetric waveguides[29–33], as well as experimental investigations[34–36], have been carried out for Y– junction waveguides. The more difficult task of multimode Y– junctions[37–39] has received less attention, probably due to the complexity of the problem. The model used here is one developed by Anderson[40] for the TE– transmission coefficient of a single– mode dielectric slab waveguide Y– junction. TE refers to a mode with its electric field in the plane of the slab waveguide. The analysis was initially designed to cater for straight input and output slab waveguides with a Y– junction half– angle, α, Fig.2.13a. The effective index method can then be used to convert the ridge Y– junction waveguides into the slab waveguides of the Anderson model. However, two major changes have been made to the formalism in order to make it directly applicable to the structures in this chapter. (i) The first involves a switch from TE– to TM– transmission. The propagation constants of the TE modes in the initial ridge structures are replaced by the TM propagation constants of the slab waveguide approximation, Fig.2.7c, as described in Sec.2.4.2. For this reason, the Anderson model is modified to cope with TM modes. (ii) The second change involves the Y– junction arm separation which is achieved by two S– bends where the curved sections have a radius, R. Thus the Y– junction (one branch of which is high– lighted in Fig.2.9) is shaped like the tangential intersection of two sets of circles where the join point is shown in Fig.2.13b. In this instance the Y– junction half– angle, α, is assumed to be that of the tangent to the curved guides at the point $z=0$, where the total guide width is approximately 2w. The insertion loss

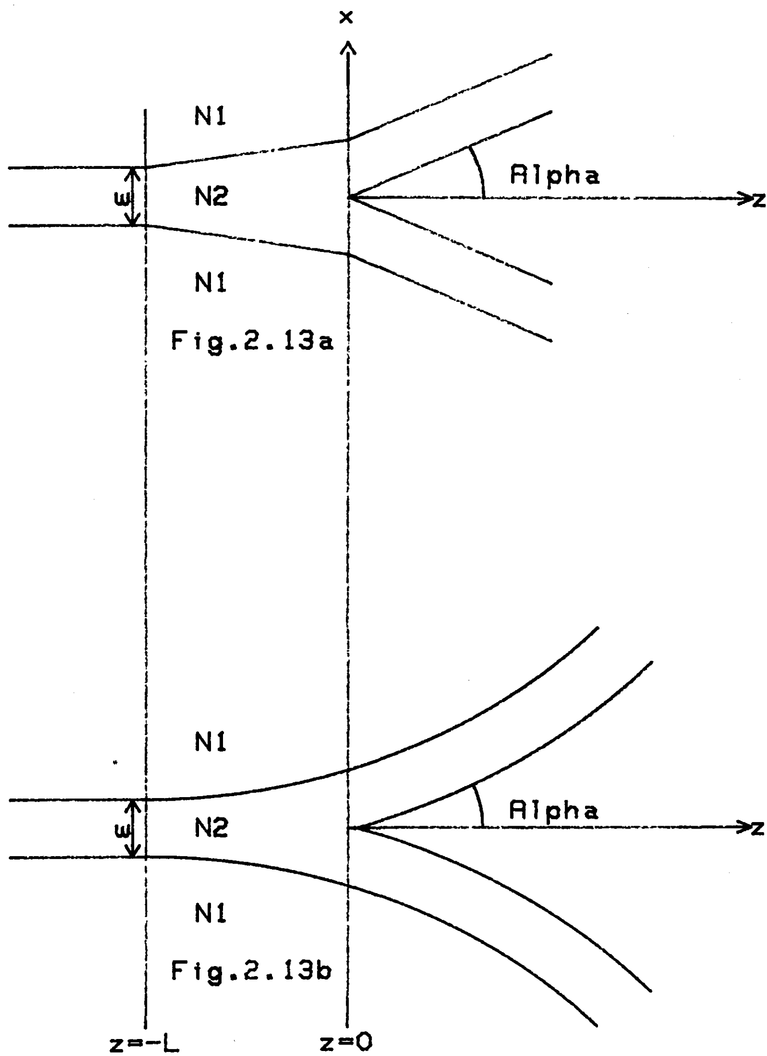

Fig.2.13

Straight and S-Bend Y-Junction Waveguides

will be an underestimate for the straight guide case since the mode is entering a curved guide. But for large values of the radius of curvature, and good mode confinement, the loss matches that for a straight guide more accurately.

2.6.1 Mathematical Basis

The waveguide structure analysed is a symmetrical Y-junction composed of one straight and two curved dielectric slab waveguides of width w, the latter overlapping to form a tapered section of length L. The medium is assumed to be isotropic, source-free and lossless and the guiding and substrate indices are N_2 and N_1 respectively, Fig.2.13b. The aim of this section is to model the Y-junction mathematically and obtain the transmission, reflection and scattering coefficients which dominate the behaviour of the fundamental mode travelling from the input guide to the two output guides.

A preliminary study of the work on tapers carried out by Marcuse[41] for sufficiently long tapers, applicable to the regimes encountered during the present analysis, indicate that the transmission coefficient is close to unity and hence the overall transmission coefficient is characterised by that of the Y-junction.

Far from the junction, all three waveguides are considered to support the fundamental mode dictated by the thickness, w, of the waveguides and the guide indices N_1 and N_2. Close to the junction, however, coupling phenomena do exist and have been analysed by Yajima[42]. In order to simplify the mathematics, the field distribution in $z>0$ is assumed to be a superposition of the modes of each of the output waveguides in isolation. This assumption results in the transmission

coefficient being less than that for the real junction and can be pictured as an abrupt Y– junction where the propagation constant at $z=0$ is assumed to change discontinuously. As the Y– junction angle is increased, the calculated transmission becomes more accurate since the strong coupling effects are experienced for smaller values of z.

2.6.2 Transmission, Reflection and Scattering Coefficients

With reference to Fig.2.13b, the incident TM mode, H_y^i, on the plane $z=0$ excites a transmitted mode, τH_y^t, in the region $z>0$. In addition, the discontinuity at $z=0$ produces a reflected mode, rH_y^i, in $z < 0$ plus radiation fields which are summed over the plane $z=0$. Matching tangential electric and magnetic field components in $z \gtrless 0$ on the plane $z=0$ produces a pair of equations similar to those for the TE– case solved by Anderson[40]:

$$(1+r)H_y^i(x,0)+\int_0^\infty q_r(\rho)H_y^i(\rho)d\rho = \tau H_y^t(x,0)+\int_0^\infty q_t(\rho)H_y^t(\rho)d\rho \quad 2.42$$

$$(1-r)E_x^i(x,0)+\int_0^\infty q_r(\rho)E_x^i(\rho)d\rho = \tau E_x^t(x,0)+\int_0^\infty q_t(\rho)E_y^t(\rho)d\rho \quad 2.43$$

where i, r, and t indicate incident, reflected and transmitted waves, the integrals represent the radiation modes and $H_y^i(x,0)$ is the incident field of the TM guided mode. $|r|^2$ and $|\tau|^2$ are the reflection and transmission coefficients respectively. Brooke and Kharadly[43] have verified that most of the unguided radiation is scattered in the forward direction and so it is safe to assume that $q_r(\rho)$ is small as assumed by Marcuse[41] and Anderson[40]. Thus, τ and r can be isolated by relying on the orthogonality of the modes, in the isolated waveguides, and multiplying Eqns.2.42– 43 by $E_x^t(x,0)$ and $H_y^{t*}(x,0)$ respectively and integrating with respect to x over the $z=0$ plane.

$$\tau = \frac{\beta_a\beta_b}{\beta_a+\beta_b}\frac{1}{\omega}\int_{-\infty}^{\infty}\frac{H_y^i(x,0)H_y^{t*}(x,0)}{\varepsilon}\,dx \qquad 2.44$$

$$r = \frac{\beta_a-\beta_b}{\beta_a+\beta_b} \qquad 2.45$$

where β_a and β_b are the propagation constants just before and after $z=0$ in Fig.2.13b. ω and ε are the radian frequency and permittivity respectively. The transmisson, reflection and scattering coefficients, T, R and S, are related by:

$$T = |\tau|^2$$
$$R = |r|^2 \qquad 2.46$$
$$T + R + S = 1$$

The evaluation of the integral in Eqn.2.44 has been determined for the TE– transmission case[40]. The analytical procedure was repeated for the TM– case by the author and the main results will be quoted here. The transmission, τ (Eqn.2.44), can be written as:

$$\tau = 2AB[J_1 + J_2\cos(\tfrac{1}{2}\kappa_b w) + \exp(\gamma_a w)\cos(\kappa_a w)\cos(\tfrac{1}{2}\kappa_b)\{\exp(\gamma_b w)J_3(\alpha) + J_3(-\alpha)\}] \qquad 2.47$$

where β_a, κ_a and γ_a are functions of the propagation constant of a guide of width 2w, representing the tapered guide at the $z=0$ boundary, Fig.2.13b. The method for calculating them is given in Sec.2.3.2.

β_b, κ_b and γ_b are calculated for the isolated guides, of width w, in the region $z \gg 0$.

J_1, J_2 and J_3 are complex functions of the propagation constants for the guide widths w and 2w, and are detailed for the TM case, in Appendix B. The equations can be directly related to those derived by Anderson[40].

A and B are the amplitudes of the incident and transmitted waves

which are normalised so that the power is unity (W/m in the y-direction) for both $z<0$ and $z>0$. Expressions for A and B are given below for the TM case:

$$A = \left[\frac{2\omega}{\beta_a}\right]^{\frac{1}{2}} \left[\frac{1}{N_2^2}\left[w + \frac{\sin(2\kappa_a w)}{2\kappa_a}\right] + \frac{1}{N_1^2}\frac{\cos^2(\kappa_a w)}{\gamma_a}\right]^{-\frac{1}{2}} \qquad 2.48$$

$$B = \left[\frac{\omega}{\beta_b}\right]^{\frac{1}{2}} \left[\frac{1}{N_2^2}\left[\frac{w}{2} + \frac{\sin(2\kappa_b w)}{2\kappa_b}\right] + \frac{1}{N_1^2}\frac{\cos^2(\kappa_b \frac{1}{2} w)}{\gamma_b} + 4\exp(-\tfrac{1}{2}\gamma_b w)\cos(\tfrac{1}{2}\kappa_b w)\mathrm{Re}\{\}\right]^{-\frac{1}{2}} \qquad 2.49$$

where:

$$\{\} = \exp(-i\alpha\beta_b w)\left[\frac{\exp(-\frac{1}{2}\gamma_b w - i\alpha\beta_b w)\cos(\frac{1}{2}\kappa_b w)}{2N_1^2(\gamma_b + i\alpha\beta_b)} + C(\kappa_b) + C(-\kappa_b)\right]$$

with:

$$C(\kappa_b) = \frac{\sin\{\frac{1}{2}(\kappa_b - 2\alpha\beta_b)w + i\frac{1}{2}\gamma_b w\}}{N_1^2\{(\kappa_b - 2\alpha\beta_b) + i\gamma_b\}}$$

This section has provided the mathematical basis for calculating the transmission, reflection and scattering coefficients for a ridge waveguide Y-junction via the effective index method. A numerical example will now be provided for the ridge waveguide shown in Fig.2.8.

2.6.3 Numerical Evaluation

In Fig.2.13, the relations between the junction half angle, α, the taper length, L, the radius of curvature used to form the S-bends and the waveguide widths is fairly complex. A study of the diagrams show that the angle and taper length vary with the guide thickness and the radius of curvature. The variations are depicted in Figs.2.14-15 where it can be seen that, for a given radius, narrow lines have shorter taper lengths and experience a smaller junction angle than wider guides.

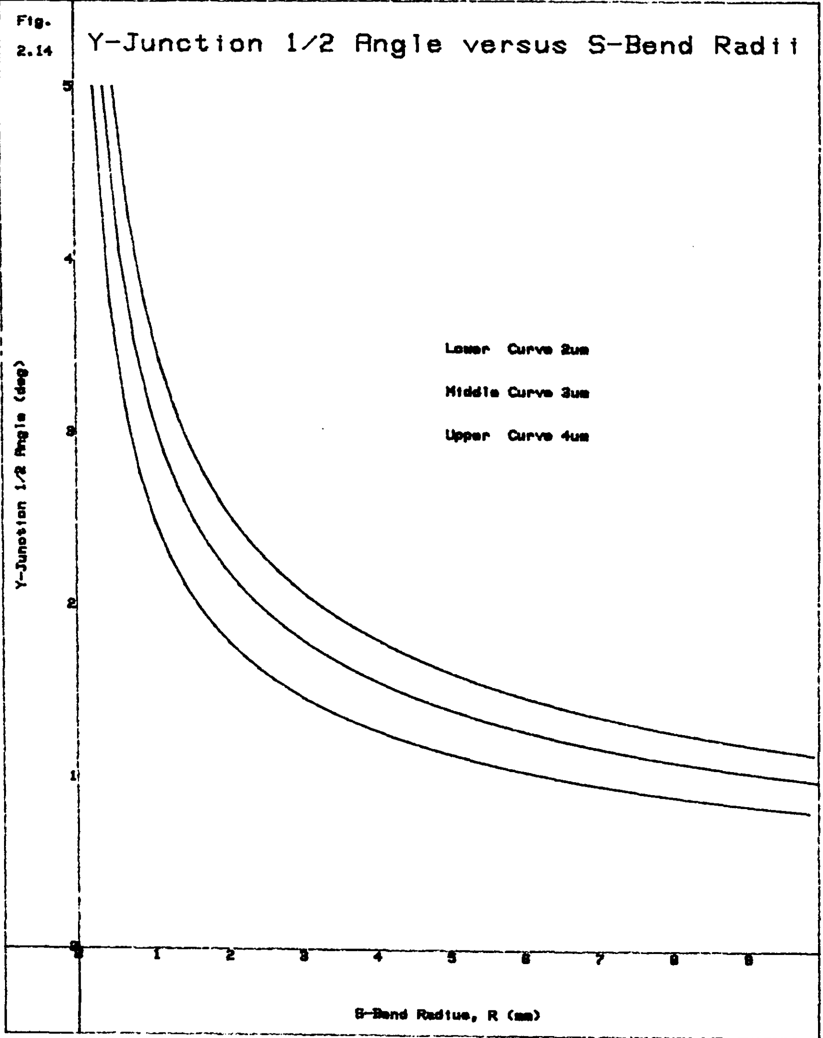

Fig.
2.14
Y-Junction 1/2 Angle versus S-Bend Radii
Y-Junction 1/2 Angle (deg)
0
1
2
3
4
5
Lower Curve 2um
Middle Curve 3um
Upper Curve 4um
0 1 2 3 4 5 6 7 8 9
S-Bend Radius, R (mm)

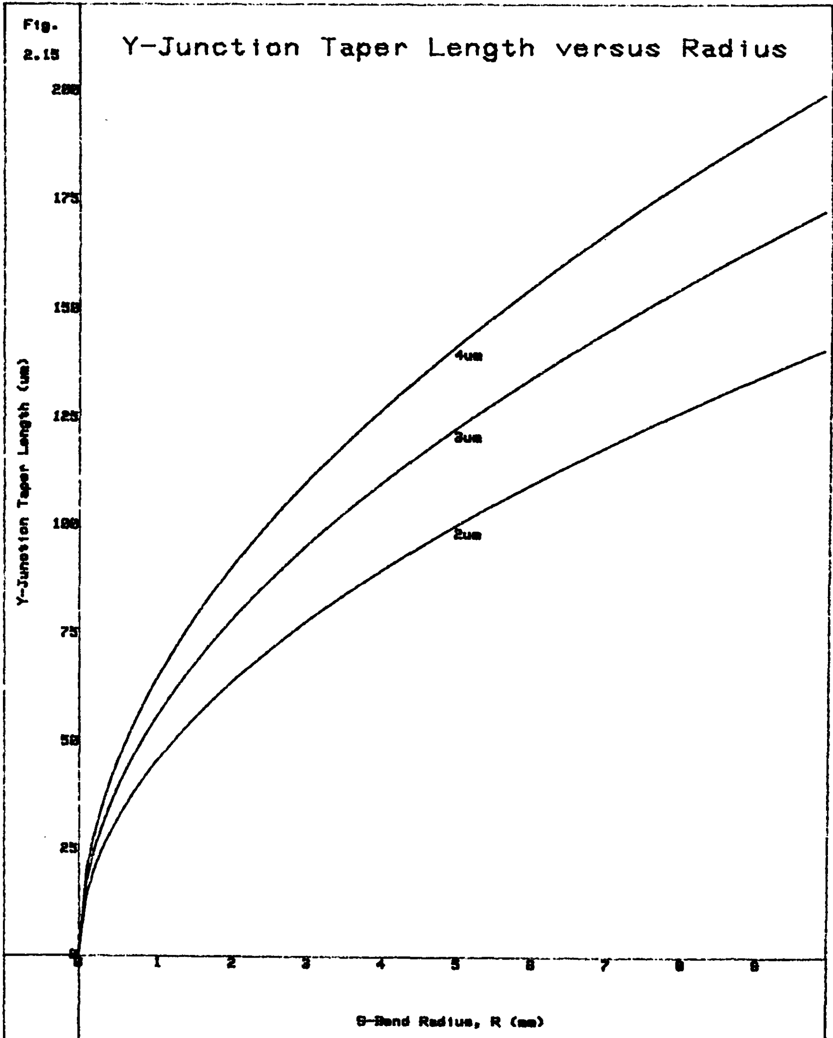

Fig.
2.15
Y-Junction Taper Length versus Radius
Y-Junction Taper Length (um)
0
25
50
75
100
125
150
175
200
4um
3um
2um
0 1 2 3 4 5 6 7 8 9
S-Bend Radius, R (mm)

Fig.2.16 is a plot of the Y–junction transmission as a function of the radius of curvature forming the S–bends. The fundamental parameters are:

(1) The radius of curvature of the waveguides forming the Y–junctions, Fig.2.13b.

(2) The widths of the ridge waveguides.

(3) Mode confinement to the guiding region – controlled by the ridge heights.

For a given ridge width and etch depth, large radii of curvature lead to less loss at the Y–junction. As the radius is increased, the Y–junction half–angle decreases, Fig.2.14, and hence the mismatch between the incident and transmitted fields is reduced[40]. Although the taper length also increases, Fig.2.15, the losses within the taper are negligible for radii of curvature much larger than the guide widths.

For a given radius of curvature and etch depth, narrower lines experience less loss at the Y–junction. Fig.2.14 shows that the narrower lines lead to a smaller Y–junction half–angle and hence less loss.

For a given radius of curvature and ridge width, an increase in the etch depth results in greater mode confinement and the Y–junction transmission increases. It would appear that the loss experienced by the field within the waveguides (the internal field[40]) is, in general, less than that experienced by fields in the evanescent tail of the modes. The reasons for this are at present unclear.

The reflection losses for the above cases were found to be negligible, and via Eqn.2.46, this indicates that any power not transmitted

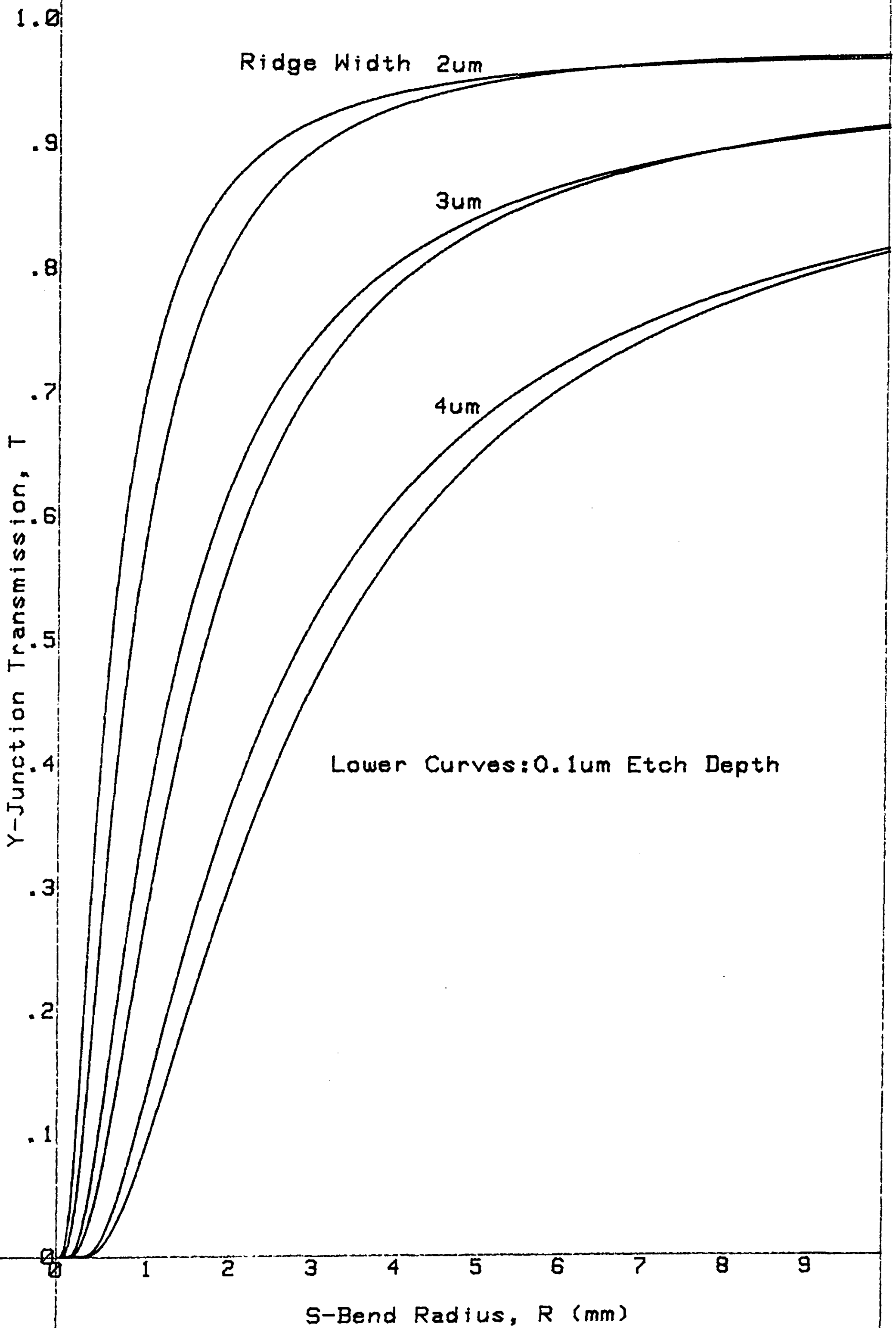
Fig. 2.16
Transmission:0.1um & 0.2um Etch Depths
Ridge Width 2um
3um
4um
Lower Curves:0.1um Etch Depth
Y-Junction Transmission, T
1.0
.9
.8
.7
.6
.5
.4
.3
.2
.1
0
1
2
3
4
5
6
7
8
9
S-Bend Radius, R (mm)

through the Y– junction is scattered into radiation modes. Hence the Y– junction scattering coefficient, S, is given by S ≃ 1 – T.

2.7 Mach– Zehnder Interferometer

2.7.1 Device Operation

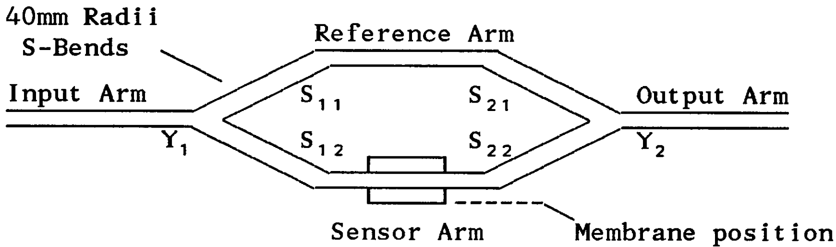

Fig.2.17

For the Mach– Zehnder waveguide structure proposed in this project, the Y– junctions, Y_1 and Y_2, are symmetrical and identical resulting in a symmetrical device. All waveguides are single– mode, a fact which is essential for efficient operation. The four S– bends, S_{11} etc, are described in Sec.2.5 and the Y– junctions in Sec.2.6. Due to the symmetrical nature of the Y– junctions light coupled into the input arm is divided equally between the S– bends, S_{11} and S_{12}, as described in Sec.2.6. At this junction, some of the light is lost to radiation via a scattering process. The guided modes travel along the curved sections of the S– bends experiencing some loss due to the curved nature of the guides. The two curved waveguide sections which form one S– bend have the same radius of curvature and the intersection point is tangential to both curves, Fig.2.9. Therefore, well– confined modes experience no transition loss when moving from the first curve to the second[47]. The modes then arrive at the straight sections of the reference and sensor arms and propagate towards the junction Y_2. The sensing arm crosses a thin membrane which, when deformed by a pressure differential across its thickness,

causes a phase–shift (via the photoelastic effect, Chap.3) in the light relative to that in the reference arm. Thus, as the modes in the S–bends, S_{21} and S_{22}, approach Y_2 a phase difference may exist between them. Is the behaviour at Y_2 identical to that at Y_1? The answer is no since (i) a phase–shift now exists between the modes which, due to symmetry was not present after passing through Y_1 and (ii) the transmission characteristics may alter, depending on the nature of the taper as described below.

Rediker and Leonberger[44] have studied the junction Y_2 as a four–port lossless network where the fourth port is a window to the radiation modes, which remove power from the guided wave system in the vicinity of the coupler. The technique uses the properties of a scattering matrix, successfully applied in microwave circuits[45], to determine the outputs from a Y–junction for arbitrary combinations of input power and phase. There are, however, a number of restrictions on the use of the formalism which will now be discussed with respect to the analyses carried out in this chapter and the proposed device.

Assumptions

(1) The two input arms and the output arm of Y_2 must be single–mode, and thus this junction, operating as a power coupler (i.e Y_1), must act as a near–3dB splitter.

(2) It is also assumed that there is no coupling between the input ports of Y_2 – an assumption adopted in the analysis of Sec.2.6.

(3) The final assumption is that all the power of the input arm is transferred to the output arms – i.e zero coupling to radiation modes which implies no scattering. But, as discovered in

Sec.2.6. smaller radii of curvature in the S– bends forming the Y– junction, results in the scattering at Y_1 becoming more important. However, if Y_1 operates with a transmssion close to one, which happens to be the case for the design under consideration, this assumption is valid.

Now applying the formalism developed by Rediker and Leonberger[44] to the Mach– Zehnder of Fig.2.17, gives the power, P, at the output to the device in terms of the powers reaching junction Y_2:

$$P(\varphi) = \tfrac{1}{2}\{P_1(1+\delta)+P_2(1-\delta)+2(P_1P_2(1-\delta^2))^{\frac{1}{2}}\cos\varphi\} \qquad 2.50$$

where:

$P_1(1+\delta)$,$P_2(1-\delta)$ are the input powers to Y_2 from the S– bends S_{21} and S_{22} respectively. δ represents any imbalance that may exist.

φ is the phase– shift experienced in the sensing arm.

For an input power, P, and equal power division at Y_1:

$$P(\varphi) = \tfrac{1}{2}\gamma P(1+\cos\varphi) \qquad 2.51$$

γ accounts for the overall losses of the Mach– Zehnder structure where the losses are assumed to be equal in each of the paths. Thus if there is no phase– shift in the sensing arms the the output is γP and a π phase– shift between the two arms reduces the output to zero.

If the tapered sections of Y_1 and Y_2 can, at some point along their length, support more than one symmetric mode then the formalism presented still applies, although the losses at Y_2 may increase. Consider the case where there is no mode coupling in the taper section. For Y_1, the propagation constant of the mode in the input

arm would increase as the taper widens. At some point along its length more guided modes would be permitted. Since the Y–junction is symmetric, only the symmetric modes need be considered at this stage. With no mode conversion, the higher order symmetric modes are not excited. At Y_2, the recombination of the light in sections S_{21} and S_{22} (single–mode guides) would excite the even and odd modes of the structure depending on their phase difference. In the ideal case, zero phase difference should transfer the total power in S_{21} and S_{22} into the fundamental mode of the output arm. If the taper supports higher order modes these may be excited and will be lost to radiation as thay travel down the narrowing taper. This loss can be incorporated into the γ–factor, Eqn.2.51. Hence, for a given detection system, the device becomes less sensitive to phase changes.

2.7.2 Device Parameters

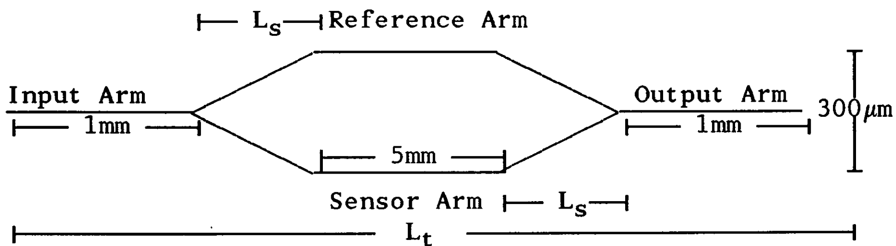

Fig.2.18

L_s is the length of the S–bends and L_t is the total length of the device. The input and output arms are cleaved to have lengths of 1mm or more to ensure that the radiated modes do not appear at the device output[46]. The 5mm length of the reference and sensing arms was based on calculations of the phase change experienced in the sensing arm which traverses a membrane, Chap.3.

The table in Appendix C shows device characteristics calculated from work presented in Sec.2.5–6 for the device in Fig.2.18 with 3μm wide ridge waveguides of height 0.1μm, Fig.2.8.

It is evident from Table C that the device length of 17mm (0.4dB losses), fabricated in this thesis, can be reduced to 10mm (2.8dB losses) without a great penalty in transmission power. Alternatively, a reduction of radius to 5mm would allow greater arm separation e.g 1mm with a device length of just 13mm. Increasing the arm separation allows wider membranes to be fabricated under the sensing arm without affecting the reference arm. There is more on this subject in Chap.3

A recent report on a GaAs–GaAlAs Y–Branch Interferometer Modulator, based on the same design for the Mach–Zehnder waveguide structure presented here, was fabricated at BTRL by Rodgers[46]. This device has an arm separation of 20μm and uses S–bend radii of 5mm incorporated into a device of total length 7mm. Losses of 5.5dBcm^{-1} were measured for the device, but direct comparison of the theories presented in this thesis is impossible since essential data in the epitaxial layer structure were not reported.

2.8 Summary

Before the theory presented in this chapter was finalised, the Y–junctions of the Mach–Zehnder waveguides fabricated in this thesis were formed by two intersecting S–bends where the radii of curvature were 40mm. An arm separation of 300μm was used giving a total device length of 17mm. The S–bend radii of curvature and the arm separation were chosen intuitively to keep the S–bend offset angle

small and hence the Y– junction loss minimal.

The recently completed theory indicates that the original design of the Mach– Zehnder waveguides given above have a calculated loss of 0.4dB. Further, using S– bend radii of 5mm reduces the overall device length the just 10mm while the loss becomes 2.8dB. Reducing the radius of curvature further leads to a rapid increase in the loss at the Y– junctions and S– bends. A shorter device has the added advantage that the material losses are reduced. Alternatively, the radius of curvature of the S– bends can be traded for greater arm separation allowing membranes of larger area and hence a device with greater sensitivity as described in the following chapter.

Appendix A

The power distribution calculations, ε_l and ε_T are based on the formulation given in Sec.2.3.3, they are detailed here for completeness.

The coordinate system will be shifted to the slab centre in order to clarify the equations:

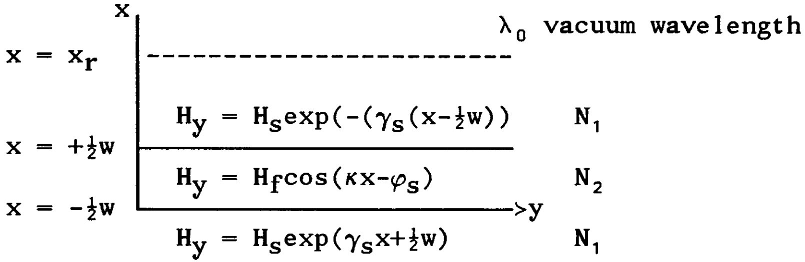

Fig.A.1

The power is obtained by integrating over the relevent regions:

$$\varepsilon_l = \frac{Nk_0}{2\omega\varepsilon_0}\int_{x_r}^{\infty}\frac{H_y^2}{n^2}\,dx = \frac{1}{2\gamma_s}\,\frac{Nk_0}{2\omega\varepsilon_0}\,\frac{H_s^2}{N_1^2}\exp(-2\gamma_s(x_r-\tfrac{1}{2}w)) \qquad \text{A.1}$$

$$\varepsilon_T = \frac{Nk_0}{2\infty\varepsilon_0}\int_{-\infty}^{\infty}\frac{H_y^2}{n^2}\,dx = \frac{Nk_0}{2\omega\varepsilon_0}\left[\int_{-\frac{1}{2}w}^{+\frac{1}{2}w}\frac{H_s^2}{N_2^2}\,dx + 2\int_{\frac{1}{2}w}^{\infty}\frac{H_y^2}{N_1^2}\,dx\right]$$

$$= \frac{Nk_0}{\omega\varepsilon_0}\left[\left[\frac{w}{2} + \sin(\kappa w)\cos(2\varphi_s)\right]\frac{H_f^2}{N_2^2} + \frac{1}{2\varphi_s}\,\frac{H_s^2}{N_1^2}\right] \qquad \text{A.2}$$

where: $H_s = H_f\cos(\frac{1}{2}\kappa w - \varphi_s)$ and $\varphi_s = \tan^{-1}\left[\frac{N_2^2\varphi_s}{N_1^2\kappa}\right]$

Appendix B

Functions controlling the transmitted Y-junction power for $L \gg \frac{1}{2}\beta_a w^2$:

$$J_1 = D(\kappa_a,\kappa_b) + D(\kappa_a,-\kappa_b) + D(-\kappa_a,\kappa_b) + D(-\kappa_a,-\kappa_b) \qquad \text{B.1}$$

where

$$D(\kappa_a,\kappa_b) \simeq \tfrac{1}{2}\exp\{i\tfrac{1}{2}(\alpha\beta_b+\kappa_a)w\}\frac{\sin\{(\alpha\beta_b + \kappa_a + \kappa_b)\}}{\alpha\beta_b+\kappa_a+\kappa_b}$$

$$J_2 = E(\kappa_a) + E(\kappa_b) \tag{B.2}$$

where

$$E(\kappa_a) \simeq \exp\{-\tfrac{1}{2}\gamma_b w - i\tfrac{1}{2}(\alpha\beta_b-\kappa_a)w\}\frac{\sin\{(\alpha\beta_b + \kappa_a - i\gamma_b)\}}{\alpha\beta_b + \kappa_a - i\gamma_b}$$

$$J_3(\alpha) \simeq \frac{\exp\{-(\gamma_a+\gamma_b)w + i\alpha\beta_b w\}}{\gamma_a + \gamma_b - i\alpha\beta_b} \tag{B.3}$$

Appendix C

TABLE C

S-B Radius (mm)	40	6	5	4	3	2
Y-J ½ Angle, α (deg)	0.5	1.1	1.3	1.5	1.8	2.2
Y-J Taper Length (μm)	340	135	120	110	95	80
Y-J Transmission	0.97	0.86	0.82	0.80	0.74	0.62
S-B Length, L_s (mm)	5.0	1.8	1.6	1.4	1.2	1.0
S-B Offset (deg)	1.5	4.4	5.0	5.5	6.2	7.8
S-B Transmission	0.99	0.96	0.88	0.70	0.40	0.11
Device Length, L_t (mm)	17.0	10.6	10.2	9.8	9.4	9.0
Device Transmission	0.92	0.68	0.52	0.31	0.09	0.005
Device Loss (dB)	0.4	1.6	2.8	5.0	10.6	23.3

where S−B and Y−J refer to S−Bends and Y−Junctions respectively.

References

[2.1] YARIV, A., LEITE, R.C.C.:Applied Physics Letters, 2, p55, 1963

[2.2] GARMIRE, E.:NEREM 72, Proceedings of the Solid State Circuits, pp115–118, (NEREM, Boston, 1972)

[2.3] Kittel, C.:'Introduction to Solid State Physics', John Wiley and Sons, p223, 1976

[2.4] RASHEVSKAYA, E.P. and FISTUL,V.I.:'Infra-Red Absorption of GaAs doped with Group III Impurities', Soviet Physics – Solid State, 9, No.12, 1968.

[2.5] REINHART, F.K., HAYASHI, I. and PANISH, M.B.:Journal of Applied Physics, 42, p4466, 1971.

[2.6] TAMIR, T. (Ed.):'Integrated Optics', Springer and Verlag, Topics in Applied Physics, 7, pp45–53, 1974

[2.7] Adachi, S.:'GaAs, AlAs and $Al_xGa_{1-x}As$: Material Parameters for Use in Research and Device Applications', Journal of Applied Physics, 58, No.3, ppR1–R29, 1985

[2.8] EVTUHOV, V. and YARIV, A.:'GaAs and GaAlAs Devices for Integrated Optics', IEEE Transactions on Microwave Theory and Techniques, MTT–23, No.1, 1975

[2.9] KOSHIBA, M. and SUZUKI, M.:'Vectorial Wave Analysis of Dielectric Waveguides for Optical-Integrated Circuits using Equivalent Network Approach', Journal of Lightwave Technology, LT–4, No.6, pp656–664, 1986

[2.10] KOSHIBA, M.,HAYATA, K. and SUZUKI, M.:'Finite-Element Solution of Anisotropic Waveguides with Arbitrary Tensor Permittivity', Journal of Lightwave Technology, LT–4, No.2, pp121–126, 1986

[2.11] LAGASSE P.E.:'Recent Developments on Beam Propagation Theory for Integrated Optics Applications', Proceedings of the 2nd European Conference, IEE Conference Publication, pp1–4, Florence 1983

[2.12] YASUURA, K., SHIMOHARA, K. and MIYAMOTO, T.:'Numerical Analysis of a Thin-film Waveguide by Mode-matching Method', Journal of the Optical Society of America, 70, No.2, pp183–191, 1980

[2.13] MITTRA, R., HOU, Y. and JAMNEJAD, V.:'Analysis of Open Dielectric Waveguides using Mode-matching Technique and Variational Methods', IEEE Transactions on Microwave Theory and Techniques, MTT–28, No.1, pp36–43, 1985

[2.14] SHARMA, A., MISHRA, P.K. and GHATAK, A.K.:'Analysis of Single Mode Waveguides and Directional Couplers with Rectangular Cross-section', Proceedings of the 2nd European Conference, IEE Conference Publication, pp9–12, Florence 1983

[2.15] MATSUHARA, M.:'Analysis of TEM Modes in Dielectric Waveguides by a Variational Method', Journal of the Optical Society of America, 63, No.12, pp1514–1517, 1973

[2.16] Mac BEAN, M.:'Multi Quantum Well Structures for Optical Waveguides', PhD Thesis, University of Glasgow, 1986.

[2.17] DIESTEL, H.:'A Method for Calculating the Guided Modes of Strip-loaded Optical Waveguides with Arbitrary Index Profile', IEEE Journal of Quantum Electronics, QE–20, No.11, pp1288–1293, 1984

[2.18] HOCKER, G.B. and BURNS, W.K.:'Mode Dispersion in

Diffused Channel Waveguides by the Effective Index Method', Applied Optics, **16**, No.1, pp113–118, 1977

[2.19] MITSUNOBU, M. and NISHIDA, S.:'Bending Losses of Dielectirc Rectangular Waveguides for Integrated Optics', Journal of the Optical Society of America, **68**, No.3, pp316–319, 1978

[2.20] BAETS, R. and LAGASSE, P.E.:'Loss Calculation and Design of Arbitrarily Curved Integrated–optic Waveguides', Journal of the Optical Society of America, **73**, No.2, pp177–182, 1983

[2.21] SNYDER, A.W., WHITE, I. and MITCHELL, D.J.:'Radiation from Bent Optical Waveguides', Electronics Letters, **11**, No.15, pp332–333, 1975

[2.22] INOUE, H., HIRUMA, K. ISHIDA, K. ASAI, T. and MATSUMURA, H.:'Low Loss GaAs Optical Waveguides', Journal of Lightwave Technology, **LT–3**, No.6, pp1270–1276, 1985

[2.23] AUSTIN, M.W., and FLAVIN, P.G.:'Small–Radii Curved Rib Waveguides in GaAs/GaAlAs Using Electron–Beam Lithography', Journal of Lightwave Technology, **LT–1**, No.1, pp236–240, 1983

[2.24] DERI, R.J., KAPON, E. and SCHIAVONE, L.M.:'Bend Losses in GaAs/AlGaAs Optical Waveguides', Electronics Letters, **23**, No.16, pp845–847, 1987

[2.25] HUTCHESON, L.D., WHITE, I.A. and BURKE, J.J.:'Comparison of Bending Losses in Integrated Optical Circuits', Optics Letters, **5**, No.6, pp276–278, 1980

[2.26] MARCATILLI, E.A.J., MILLER, S.E.:'Improved Relations Describing Directional Control in Electromagnetic Wave Guidance', Bell Systems Technical Journal, **48**, pp2161–2188, 1969

[2.27] MINFORD, W.J., KOROTKY, S.K. and ALFERNESS, R.C.:'Low–loss Ti:$LiNbO_3$ Waveguide Bends at λ = 1.3μm', IEEE Journal of Quantum Electronics, **QE–18**, No.10, pp1802–1806, 1982

[2.28] AUSTIN, M.W.:'GaAs/GaAlAs Curved Rib Waveguides', IEEE Journal of Quantum Electronics, **QE–18**, No.4, pp795–800, 1982

[2.29] OGUSU, K.:'Transmission Characteristics of Single–mode Asymmetric Dielectric Waveguide Y–Junctions', Optics Communications, **53**, No.3, pp169–172, 1985

[2.30] SASAKI, H. and MIKOSHIBA, N.:'Normalised Power Transmission in Single Mode Optical Branching Waveguides', Electronics Letters, **17**, No.3, pp136–138, 1981

[2.31] SASAKI, H., and ANDERSON, I.:'Theoretical and Experimental Studies on Active Y–Junctions in Optical Waveguides', IEEE Journal of Quantum Electronics, **QE–14**, No.11, pp883–892, 1978

[2.32] SOMEDA, C.G.:'Simple Way to Understand the Behaviour of an Optical Y–Junction', Electronics Letters, **20**, No.8, pp349–350, 1984

[2.33] MURAKAMI, Y. and IKEDA, M.:'Single–Mode Optical Y–Branching Circuit using Deposited Silica Guides (DS Guides)', Electronics Letters, **17**, No.12, pp411–413, 1981

[2.34] CULLEN, T.J. and WILKINSON, C.D.W.:'Radiation Losses from Single–mode Optical Y–junctions formed by

Silver– ion Exchange in Glass', Journal of the Optical Society of America, **10**, No.4, pp134–136, 1984

[2.35] CULLEN, T.:'Y– Junction Analysis', PhD Thesis, University of Glasgow, 1986.

[2.36] AL– HEMYARI, K.A.A.:'Design Fabrication By Dry Etching and Characterisation of Y– junctions in GaAs/GaAlAs', MSc Thesis, University of Glasgow, 1987.

[2.37] YAJIMA, H.:'Coupled Mode Analysis of Dielectric Planar Branching Waveguides', IEEE Journal of Quantum Electronics, **QE– 14**, No.10, pp749– 755, 1978

[2.38] BURNS, W.K. and MILTON, A.F.:'Mode Conversion in Planar– Dielectric Separating Waveguides', IEEE Journal of Quantum Electronics, **QE– 11**, No.1, pp32– 39, 1975

[2.39] YAJIMA, H.:'Dielectric Thin– film Optical Branching Waveguide', Applied Physics Letters, **22**, No.12, pp 647– 649, 1973

[2.40] ANDERSON, I.:'Transmission Performance of Y– Junctions in Planar Dielectric Waveguide', Microwaves, Optics and Acoustics, **2**, No.1, 1978

[2.41] MARCUSE, D.:'Radiation Losses of Tapered Dielectric Slab Waveguides', Bell System Technical Journal, **49**, pp273– 290, 1970

[2.42] YAJIMA, H.:'Theory and Applications of Dielectric Branching Waveguides', Proceedings of the Symposium on Optical and Acoustical Micro– Electronics, New York, 1974

[2.43] BROOKE, G.H. and KHARADLY, M.M.Z.:'Step Discontinuities on Dielectric Waveguides', Electronics Letters, **12**, pp473– 475, 1976

[2.44] REDIKER, R.H. and LEONBERGER, F.J.:'Analysis of Integrated Optics Near 3dB Coupler and Mach– Zehnder Interferometric Modulator Using Four– Port Scattering Matrix', IEEE Journal of Quantum Electronics, **QE– 18**, No.10, pp1813– 1816, 1982

[2.45] MONTGOMERY, C.G., DICKE, R.H. and PURCELL, E.M.:'Principles of Microwave Circuits', New York: Mc Graw– Hill, pp139– 161, 1948

[2.46] RODGERS, P.M.:'GaAs– GaAlAs Y– Branch Interferometric Modulator', Proceedings of the 3rd European Conference, Integrated Optics:Springer– Verlag Press, pp117– 120, Berlin 1985

[2.47] MARCATILLI, E.A.J.:'Bends in Optical Dielectric Guides' Bell Systems Technical Journal, **48**, pp2103– 2132, 1969

CHAPTER THREE

Mathematical Theory of Photoelasticity Applied to Thin Plates

3.1 Introduction

Elasticity theory has been applied to many waveguide devices including photoelastic waveguides[1], a wide variety of acoustic interactions[2–8] and is currently being applied to the relatively new field of Strain–Layer Superlattices[9] (SLS's). The complexity of the analyses often means that the models are restricted to the structures and boundary conditions for each field. The mathematical analysis which follows has been specifically developed for direct application to a thin plate though, where possible general equations, are indicated. A thin plate is defined as one in which two dimensions are much larger than the third. Since it is intended to apply the results to a GaAs plate (or membrane) it must be borne in mind that GaAs is a single–crystal material. From the viewpoint of elasticity, GaAs is an anisotropic material, which means that the principal crystal axes play an important role and care must be exercised when defining a coordinate system with respect to these axes.

The membranes are formed in only a small section of a wafer so it is pertinent to assume that the edges of the membrane are pinned to the surrounding material and so do not experience any movement. The border of the membrane can be considered elliptical due to the etching procedure used in its fabrication, Chap.4. In addition, the pressure is regarded as uniform over the membrane. This results in a pressure differential across its thin dimension. These assumptions make the task of obtaining a analytic relationship between the deflection of the membrane and the applied pressure rather than

having to carry out a finite element analysis requiring a minicomputer.

3.2 Membrane Coordinate System

The membrane of Fig.3.1 is treated as a thin plate i.e the membrane thickness, h is much less than the planar dimensions a and b. The principal crystal axes (<100>, <010> and <001>) are clearly indicated and are chosen to conform to those obtained in crystal growth for this project. In this orientation the <100> crystal axis points out of the optical surface the wafer.

The cartesian coordinate system x_1,x_2,x_3 chosen for this analysis has axes which are rotated anti-clockwise through 45° about the <100> axis. The natural cleavage planes of the wafer lie along <01$\bar{1}$> and <011>, which correspond to the x_2 and x_3 directions respectively. For reasons discussed in Chap.4, the elliptical axes of the membrane were also aligned along these directions. The tensors generally found in standard texts[10–11] are defined with respect to the principal axes. Thus it is required to rotate the tensors through 45° anti-clockwise about the <100> axis in order to align them to the membrane coordinate system.

The middle plane or neutral plane of the membrane is also shown on Fig.3.1. It is defined as the plane which bisects the membrane in the thin dimension (perpendicular to the x_1 axis). The origin of the cartesian coordinate system is taken to lie in this plane, thus making the boundaries $x_1 = \pm\frac{1}{2}h$ while the major and minor axes of the ellipse are $x_2 = \pm a$ and $x_3 = \pm b$ respectively. The pressure P is uniform over the $x_1 = \frac{1}{2}h$ face of the membrane, and acts in the $-x_1$ direction.

3.3 Strain– Displacement Relations

In one dimension, strain e, has the simple definition of increase in length, du, per unit length, dx:

$$e = \frac{du}{dx} \qquad 3.1$$

However, when three dimensions are involved the strain becomes a second rank tensor consisting of nine components. The strain is represented as follows:

$$e_{ij} = \begin{bmatrix} e_{11} & e_{12} & e_{13} \\ e_{21} & e_{22} & e_{23} \\ e_{31} & e_{32} & e_{33} \end{bmatrix} \qquad 3.2$$

The relation between the strains and the material displacements is given below:

$$e_{ij} = \frac{1}{2}\left[\frac{\partial u_i}{\partial x_j} + \frac{\partial u_j}{\partial x_i}\right] \qquad i,j=1,2,3 \qquad 3.3$$

e_{11},e_{22} and e_{33} are known as the normal strains and the remaining six strains are termed the shear strains. A physical interpretation of e_{11} and e_{13} is given in Fig.3.2.

Due to the obvious symmetry in the shear strains (Eqn.3.3) it is possible to reduce the number of components from nine to six:

$$e_{ij} = \begin{bmatrix} e_{11} \\ e_{22} \\ e_{33} \\ 2e_{23} \\ 2e_{13} \\ 2e_{12} \end{bmatrix} \qquad 3.4$$

At this point a number of assumptions attributed to Kirchhoff[10] are

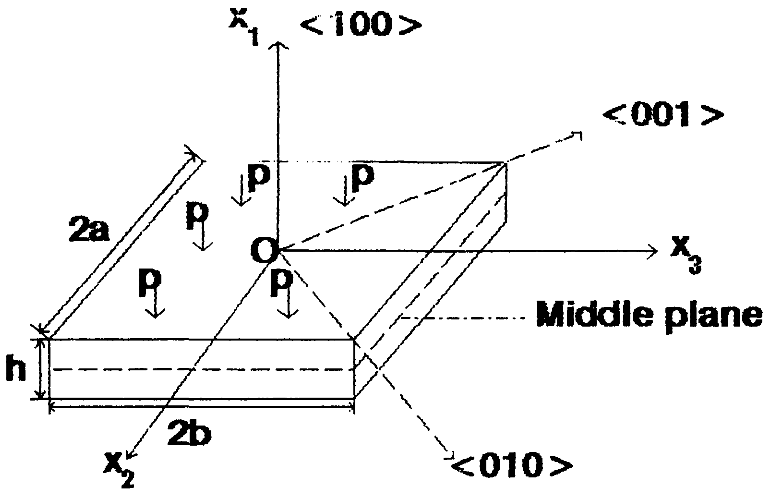

Fig.3.1

The membrane coordinate system

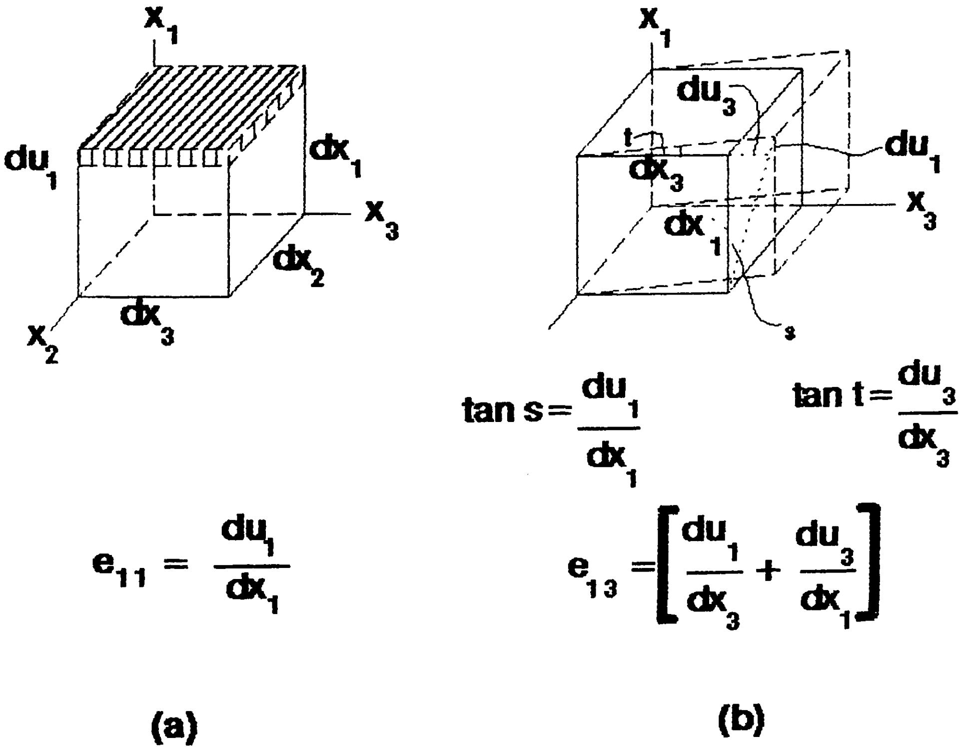

$$\tan s = \frac{du_1}{dx_1} \qquad \tan t = \frac{du_3}{dx_3}$$

$$e_{11} = \frac{du_1}{dx_1} \qquad e_{13} = \left[\frac{du_1}{dx_3} + \frac{du_3}{dx_1}\right]$$

(a) (b)

Fig.3.2

e_{11} and e_{13} strain components

made which restrict this mathematical analysis to deflections of the membrane which are small compared to its thickness.

Kirchhoff's Assumptions:

1. The middle or neutral plane of the membrane remains unstrained throughout its deformation. The equilibrium of the forces acting on an element of the plate in the Ox_2 *and* Ox_3 *directions can be neglected.*

2. The normal strain e_{11}*, i.e that normal to the plane of the membrane, is negligible and the corresponding stress* $\sigma_{11} \ll \sigma_{22}, \sigma_{33}$*. This allows* e_{11} *and* σ_{11} *to be neglected from the stress–strain relations.*

3. The normals to the middle plane before bending remain normal to this plane after bending. This results in the out–of–plane shear strains e_{13}, e_{12} *being negligible.*

A great deal of simplification can now be achieved based on the above assumptions. From assumptions 2 and 3:

$$e_{11} = e_{13} = e_{12} = 0 \tag{3.5}$$

There are now only three strains to take into account:

$$e_{22} = \frac{\partial u_2}{\partial x_2} \tag{3.6}$$

$$e_{33} = \frac{\partial u_3}{\partial x_3} \tag{3.7}$$

$$e_{23} = \frac{1}{2}\left[\frac{\partial u_2}{\partial x_3} + \frac{\partial u_3}{\partial x_2}\right] \tag{3.8}$$

All three strains can now be expressed in terms of u_1. In Eqn.3.5,

$e_{11} = \partial u_1/\partial x_1 = 0$ which implies that $u_1 = u_1(x_2,x_3)$. Consider the out-of-plane shear strains given in Eqn.3.5:

$$e_{13} = \frac{1}{2}\left[\frac{\partial u_1}{\partial x_3} + \frac{\partial u_3}{\partial x_1}\right] \qquad 3.9$$

$$e_{12} = \frac{1}{2}\left[\frac{\partial u_1}{\partial x_2} + \frac{\partial u_2}{\partial x_1}\right] \qquad 3.10$$

Integrating Eqns.3.9 and 3.10 with respect to x_1 gives:

$$u_3 = -x_1\frac{\partial u_1}{\partial x_3} + f(x_2,x_3) \qquad 3.11$$

$$u_2 = -x_1\frac{\partial u_1}{\partial x_2} + g(x_2,x_3) \qquad 3.12$$

The functions f and g represent deformations in the neutral plane. But from assumption 1, negligible strain exists in this plane so these functions can be approximated to zero.

$$u_3 = -x_1\frac{\partial u_1}{\partial x_3} \qquad 3.13$$

$$u_2 = -x_1\frac{\partial u_1}{\partial x_2} \qquad 3.14$$

Finally, the three remaining strains can be re-written in terms of u_1 by substituting Eqns.3.13-14 into Eqns.3.6-8. Thus the strains can be given in terms of the displacement in the direction of the applied pressure:

$$e_{22} = -x_1\frac{\partial^2 u_1}{\partial x_2^2} \qquad 3.15$$

$$e_{33} = -x_1\frac{\partial^2 u_1}{\partial x_3^2} \qquad 3.16$$

$$e_{23} = -x_1 \frac{\partial^2 u_1}{\partial x_2 \partial x_3} \qquad 3.17$$

3.4 Stress– Strain Relations

In order to discover the relation between pressure and displacement it is necessary to take the intermediate step of considering the stress– strain and hence stress– displacement relations. The stress– strain relations are defined in terms of a generalised form of Hooke's Law which simply states that each component of the stress varies linearly with the components of the strain:

$$\sigma_{ij} = c_{ijkl} e_{kl} \qquad 3.18$$

The inverse relation can be expressed as follows:

$$e_{ij} = s_{ijkl} \sigma_{kl} \qquad 3.19$$

where c and s are the stiffness and compliance tensors respectively. They are both fourth rank tensors which mean that they each, in their most general form, consist of 81 independent constants. The symmetry of the stress and strain tensors, e.g $e_{ij} = e_{ji}$ (Eqn.3.3), results in a reduction in the number of components to 21, Appendix A. The 21 independent components of the stiffness and compliance tensors can be reduced still further when the elastic symmetry of the crystal is taken into account. GaAs has a zinc– blende structure which puts it in a cubic class often referred to as possessing $\bar{4}3m$ crystal symmetry[11]. This notation can be broken down into its three components, each a spatial transformation which maps the crystal back onto its original geometry:

(1) $\bar{4}$ implies an axis about which 4– fold rotational symmetry exists, where each rotation is followed by an inversion i.e

$(x_1, x_2, x_3) \rightarrow (-x_1, -x_2, -x_3)$.

(2) 3 corresponds to an axis which has 3-fold symmetry.

(3) m is simply the existence of a mirror plane in the crystal.

The three transformations result in a reduction in the number of stiffness and compliance components from 21 to just three: $c_{11}=c_{1111}$, $c_{12}=c_{1122}$ and $c_{44}=2c_{2323}$, arranged as shown below:

$$\begin{bmatrix} \sigma_{11} \\ \sigma_{22} \\ \sigma_{33} \\ \sigma_{23} \\ \sigma_{13} \\ \sigma_{12} \end{bmatrix} = \begin{bmatrix} c_{11} & c_{12} & c_{12} & 0 & 0 & 0 \\ c_{12} & c_{11} & c_{12} & 0 & 0 & 0 \\ c_{12} & c_{12} & c_{11} & 0 & 0 & 0 \\ 0 & 0 & 0 & c_{44} & 0 & 0 \\ 0 & 0 & 0 & 0 & c_{44} & 0 \\ 0 & 0 & 0 & 0 & 0 & c_{44} \end{bmatrix} \begin{bmatrix} e_{11} \\ e_{22} \\ e_{33} \\ e_{23} \\ e_{13} \\ e_{12} \end{bmatrix} \qquad 3.20$$

The strain-stress relationship is similar.

It was emphasised in Sec.3.2 that the stiffness and compliance tensors are defined with respect to the principal axis coordinate system. So it is necessary to rotate the tensors anti-clockwise through 45° about the <100> axis in order to realign them with the membrane coordinate system (Fig.3.1). This results in a mixing of components although the number of independent constants remains identical. The tensor below shows the final general stress-strain relation for the zinc-blende structure of GaAs when the stiffness tensor undergoes the above transformation:

$$\begin{bmatrix} \sigma_{11} \\ \sigma_{22} \\ \sigma_{33} \\ \sigma_{23} \\ \sigma_{13} \\ \sigma_{12} \end{bmatrix} = \begin{bmatrix} c_{12} & c_{12} & c_{12} & 0 & 0 & 0 \\ c_{12} & [+]_c & [-]_c & 0 & 0 & 0 \\ c_{12} & [-]_c & [+]_c & 0 & 0 & 0 \\ 0 & 0 & 0 & (-)_c & 0 & 0 \\ 0 & 0 & 0 & 0 & c_{44} & 0 \\ 0 & 0 & 0 & 0 & 0 & c_{44} \end{bmatrix} \begin{bmatrix} e_{11} \\ e_{22} \\ e_{33} \\ e_{23} \\ e_{13} \\ e_{12} \end{bmatrix} \qquad 3.21$$

where:

$$[+]_c = [\tfrac{1}{2}(c_{11}+c_{12})+c_{44}] \qquad 3.22$$

$$[-]_c = [\tfrac{1}{2}(c_{11}+c_{12})-c_{44}] \qquad 3.23$$

$$(-)_c = \tfrac{1}{2}(c_{11}-c_{12}) \qquad 3.24$$

Similarly:

$$\begin{bmatrix} e_{11} \\ e_{22} \\ e_{33} \\ e_{23} \\ e_{13} \\ e_{12} \end{bmatrix} = \begin{bmatrix} s_{12} & s_{12} & s_{12} & 0 & 0 & 0 \\ s_{12} & [+]_s & [-]_s & 0 & 0 & 0 \\ s_{12} & [-]_s & [+]_s & 0 & 0 & 0 \\ 0 & 0 & 0 & (-)_s & 0 & 0 \\ 0 & 0 & 0 & 0 & s_{44} & 0 \\ 0 & 0 & 0 & 0 & 0 & s_{44} \end{bmatrix} \begin{bmatrix} \sigma_{11} \\ \sigma_{22} \\ \sigma_{33} \\ \sigma_{23} \\ \sigma_{13} \\ \sigma_{12} \end{bmatrix} \qquad 3.25$$

where:

$$[+]_s = [\tfrac{1}{2}(s_{11}+s_{12})+s_{44}] \qquad 3.26$$

$$[-]_s = [\tfrac{1}{2}(s_{11}+s_{12})-s_{44}] \qquad 3.27$$

$$(-)_s = \tfrac{1}{2}(s_{11}-s_{12}) \qquad 3.28$$

Eqns.3.25–28 allow the three remaining strains to be written in an expanded form:

$$e_{22}=[+]_s\sigma_{22}+[-]_s\sigma_{33} \qquad 3.29$$

$$e_{33}=[-]_s\sigma_{22}+[+]_s\sigma_{33} \qquad 3.30$$

$$e_{23}=(-)_s\sigma_{23} \qquad 3.31$$

Rearranging these equations in terms of stress gives:

$$\sigma_{22} = \frac{\{[+]_s e_{22}-[-]_s e_{33}\}}{2s_{44}(s_{11}+s_{12})} \qquad 3.32$$

$$\sigma_{33} = \frac{\{[+]_s e_{33}-[-]_s e_{22}\}}{2s_{44}(s_{11}+s_{12})} \qquad 3.33$$

$$\sigma_{23} = \sigma_{32} = \frac{2e_{23}}{s_{11}-s_{12}} \qquad 3.34$$

The final step is to substitute Eqns.3.6–8 into Eqns.3.32–34 to

obtain the stress–displacement relations:

$$\sigma_{22} = \frac{-x_1}{2s_{44}(s_{11}+s_{12})}\left[[+]_s\frac{\partial^2 u_1}{\partial x_2^2} - [-]_s\frac{\partial^2 u_1}{\partial x_3^2}\right] \qquad 3.35$$

$$\sigma_{33} = \frac{-x_1}{2s_{44}(s_{11}+s_{12})}\left[[+]_s\frac{\partial^2 u_1}{\partial x_3^2} - [-]_s\frac{\partial^2 u_1}{\partial x_2^2}\right] \qquad 3.36$$

$$\sigma_{23} = \sigma_{32} = \frac{-2x_1}{s_{11}-s_{12}}\frac{\partial^2 u_1}{\partial x_2 \partial x_3} \qquad 3.37$$

3.5 Equilibrium Relations

The stress at a point is defined by Eqns.3.35–37, but a controlling interaction which relates the stress at one point to that at neighbouring points must be taken into account. A balance of forces throughout the material is required, which implies the enforcement of the laws of equilibrium. Each volume element of the material experiences surface forces, $\Sigma\partial\sigma_{ji}/\partial x_j$ and body forces F_i. In equilibrium, the resultant force must be zero e.g for the Ox_1 direction: $\partial\sigma_{11}/\partial x_1 + \partial\sigma_{21}/\partial x_2 + \partial\sigma_{31}/\partial x_3 + F_1 = 0$. Kirchhoff's assumptions have led to e_{11},e_{13} and e_{12} being taken as negligible, which makes the determination of the associated stresses σ_{11}, σ_{13} and σ_{12} impossible from Hooke's Law. In this instance the differential equations of equilibrium shown below are used, where the body forces are neglected:

$$\frac{\partial\sigma_{11}}{\partial x_1} + \frac{\partial\sigma_{21}}{\partial x_2} + \frac{\partial\sigma_{31}}{\partial x_3} = 0 \qquad 3.38$$

$$\frac{\partial\sigma_{12}}{\partial x_1} + \frac{\partial\sigma_{22}}{\partial x_2} + \frac{\partial\sigma_{32}}{\partial x_3} = 0 \qquad 3.39$$

$$\frac{\partial\sigma_{13}}{\partial x_1} + \frac{\partial\sigma_{23}}{\partial x_2} + \frac{\partial\sigma_{33}}{\partial x_3} = 0 \qquad 3.40$$

Rearranging Eqns.3.38–40 and integrating with respect to x_1 leads to:

$$\sigma_{11} = -\iint\left[\frac{\partial\sigma_{21}}{\partial x_2} + \frac{\partial\sigma_{31}}{\partial x_3}\right]dx_1 \qquad 3.41$$

$$\sigma_{12} = \sigma_{21} = -\iint\left[\frac{\partial\sigma_{22}}{\partial x_2} + \frac{\partial\sigma_{32}}{\partial x_3}\right]dx_1 \qquad 3.42$$

$$\sigma_{13} = \sigma_{31} = -\iint\left[\frac{\partial\sigma_{23}}{\partial x_2} + \frac{\partial\sigma_{33}}{\partial x_3}\right] \qquad 3.43$$

These equations can be solved by direct substitution of Eqns.3.35–37 but the solutions are not unique until the boundary conditions are taken into account.

3.6 Boundary Conditions

The plate is considered to have pinned edges, i.e. the material at the boundary experiences no displacement, $u_1(x_2,x_3)$, and the first derivative is also zero, $\partial u_1/\partial x_i = 0$ for $i = 2,3$. The applied pressure, P, is considered uniform over the membrane surface $x_1 = \frac{1}{2}h$ (Fig.3.1). The resulting boundary conditions are summarised below:

$$\text{At } x_1 = \pm\tfrac{1}{2}h,\ \sigma_{13} = \sigma_{12} = 0 \qquad 3.44$$

$$\text{At } x_1 = -\tfrac{1}{2}h,\ \sigma_{11} = 0 \qquad 3.45$$

$$\text{At } x_1 = +\tfrac{1}{2}h,\ \sigma_{11} = -P \qquad 3.46$$

Because the pressure is constant and acts only in the Ox_1 direction, the out-of-plane shear strains σ_{13} and σ_{12} are zero at the boundary $x_1 = \pm\frac{1}{2}h$. These conditions allow the differential equations of equilibrium, Eqns.3.41–43 to be solved exactly. The mathematics is straight forward but somewhat cumbersome and will be omitted here. The final result is:

$$P = -\frac{h^3}{12}\left[A\frac{\partial^4 u}{\partial x_2^4} + 2B\frac{\partial^4 u}{\partial^2 x_2 \partial^2 x_3} + A\frac{\partial^4 u}{\partial x_3^4}\right] \qquad 3.47$$

where:

$$A = \frac{[\frac{1}{2}(s_{11}+s_{12})+s_{44}]}{2s_{44}(s_{11}+s_{12})} \qquad 3.48$$

$$B = \frac{2}{s_{11}-s_{12}} - \frac{[\frac{1}{2}(s_{11}+s_{12})-s_{44}]}{2s_{44}(s_{11}+s_{12})} \qquad 3.49$$

and $u=u_1$ is the deflection of the membrane. This differential equation is commonly known as Lagrange's Equation[10] or sometimes the Biharmonic Equation. By solving for u, the relation between the deflection u and the applied pressure P can be derived. As mentioned in Sec.3.2, the membrane border is considered elliptical and this dictates the type of solution one should expect from Lagrange's Equation. (For a material which is elastically isotropic with respect to elasticity A= B).

3.7 Elliptical Solution of Lagrange's Equation

The elliptical boundary of the membrane obeys the equation:

$$\frac{x_2^2}{a^2} + \frac{x_3^2}{b^2} = 1 \qquad 3.50$$

Due to the elliptical nature of the boundary, the deflection, u, of the membrane is taken to have the form:

$$u = M\left[1 - \frac{x_2^2}{a^2} - \frac{x_3^2}{b^2}\right]^2 \qquad 3.51$$

where M is a constant and a and b are the respective major and minor axes of the ellipse. At the membrane edge the deflection, u, and its first derivatives, $\partial u/\partial x_2$ and $\partial u/\partial x_3$, are zero, which agrees with the boundary conditions of Sec.3.6. In order to obtain the constant M, Eqn.3.51 is substituted into the Lagrange Equation, Eqn.3.47, and the coefficients equated to give:

$$M = - \frac{3P}{2h^3\left[\frac{3A}{a^4} + \frac{2B}{a^2b^2} + \frac{3A}{b^4}\right]} \qquad 3.52$$

The final form of the deflection– pressure relation is then given by:

$$u = - \frac{3P\left[1 - \frac{x_2^2}{a^2} - \frac{x_3^2}{b^2}\right]^2}{2h^3\left[\frac{3A}{a^4} + \frac{2B}{a^2b^2} + \frac{3A}{b^4}\right]} \qquad 3.53$$

The maximum deflection, u_0, at the centre of the membrane is given below and compared to experimental results in Chap.5:

$$u_0 = - \frac{3P}{2h^3\left[\frac{3A}{a^4} + \frac{2B}{a^2b^2} + \frac{3A}{b^4}\right]} \qquad 3.54$$

Choosing an elliptical solution can be justified in view of the fact that one can quite easily engineer the etching parameters to produce an approximately elliptical border, Chap.4. The mathematical analysis becomes much simpler than that, for example, of rectangular membranes where discontinuities at the corners would require a numerical approach.

3.8 Photoelastic Effect

The stresses and strains experienced by the medium are imparted to the light as phase changes. The phase– shift is composed of two components: one due to changes in the refractive index of the material, $\Delta\varphi_n$, and the other as a result of increases in the path length of the light, $\Delta\varphi_l$. The total phase change is given by:

$$\Delta\varphi = \Delta\varphi_n + \Delta\varphi_l \qquad 3.55$$

where:

$$\Delta\varphi_n = k l \Delta n \qquad 3.56$$

$$\Delta\varphi_l = k n \Delta l \qquad 3.57$$

and k is the wave number of the light, l is the original path length, n the refractive index of the unstrained material and Δn and Δl are the changes of refractive index and path length respectively.

3.8.1 Phase Shifts due to Changes in Refractive Index

The linking factor between the strain and refractive index changes is a fourth rank tensor — the photoelastic tensor, p_{ijkl}. The refractive index changes are calculated using in a second rank tensor called the impermeability tensor, dB_{ij}:

$$dB_{ij} = p_{ijkl} e_{kl} \qquad 3.58$$

where the relation between refractive index change and impermeability is given by:

$$B = \frac{1}{n^2} \quad \rightarrow \quad dB = -\frac{2}{n^3} dn \qquad 3.59$$

Care must be exercised when converting changes of impermeability into changes in refractive index to ensure that the right components are chosen, depending on both the polarisation and direction of propagation of the light. This is explained below.

When all the symmetry considerations are taken into account, the 81 components of the photoelastic tensor reduce to just 3 in a similar way to those of the stiffness and compliance tensors described in Sec.3.4. Since the photoelastic tensor is also defined relative to the

principal crystal axes, it is again necessary to rotate the tensor through a 45° anti-clockwise rotation about the <100> axis in order to align the tensor to the membrane coordinate system:

$$\begin{bmatrix} dB_{11} \\ dB_{22} \\ dB_{33} \\ dB_{23} \\ dB_{13} \\ dB_{12} \end{bmatrix} = \begin{bmatrix} p_{11} & p_{12} & p_{12} & 0 & 0 & 0 \\ p_{12} & [+]_p & [-]_p & 0 & 0 & 0 \\ p_{12} & [-]_p & [+]_p & 0 & 0 & 0 \\ 0 & 0 & 0 & (-)_p & 0 & 0 \\ 0 & 0 & 0 & 0 & p_{44} & 0 \\ 0 & 0 & 0 & 0 & 0 & p_{44} \end{bmatrix} \begin{bmatrix} 0 \\ e_{22} \\ e_{33} \\ e_{23} \\ 0 \\ 0 \end{bmatrix} \qquad 3.60$$

where:

$$[+]_p = [\tfrac{1}{2}(p_{11}+p_{12})+p_{44}] \qquad 3.61$$

$$[-]_p = [\tfrac{1}{2}(p_{11}+p_{12})-p_{44}] \qquad 3.62$$

$$(-)_p = \tfrac{1}{2}(p_{11}-p_{12}) \qquad 3.63$$

In expanded form, Eqn.3.63 can be written as:

$$dB_{11} = p_{12}e_{22} + p_{12}e_{33} \qquad 3.64$$

$$dB_{22} = [+]_p e_{22} + [-]_p e_{33} \qquad 3.65$$

$$dB_{33} = [-]_p e_{22} + [+]_p e_{33} \qquad 3.66$$

$$dB_{23} = (-)_p e_{23} \qquad 3.67$$

$$dB_{13} = dB_{12} = 0 \qquad 3.68$$

Substituting Eqns.3.6–8 into Eqns.3.64–68 gives the impermeability components in terms of displacement.

$$dB_{11} = -p_{12}x_1 \left[\frac{\partial^2 u}{\partial x_2^2} + \frac{\partial^2 u}{\partial x_3^2}\right] \qquad 3.69$$

$$dB_{22} = -x_1 \left[[+]_p \frac{\partial^2 u}{\partial x_2^2} + [-]_p \frac{\partial^2 u}{\partial x_3^2}\right] \qquad 3.70$$

$$dB_{33} = -x_1 \left[[-]_p \frac{\partial^2 u}{\partial x_2^2} + [+]_p \frac{\partial^2 u}{\partial x_3^2}\right] \qquad 3.71$$

$$dB_{23} = -x_1(-)p\frac{\partial^2 u}{\partial x_2 \partial x_3} \qquad 3.72$$

At this point, it is necessary to integrate the impermeabilty changes over the length of the path along which the light is guided in order to obtain the total effect of the change in refractive index. In addition to the directions and length of the light path, the polarisation dictates the components of the impermeability involved in interaction with the light wave and the medium.

Consider light confined to a waveguide, of length 2a, aligned with the major axis, x_2, of the membrane, Fig.3.3. Integrating Eqns.3.69–72 with respect to x_2 will give the total effective change in impermeability over the path length, where u is given by Eqn.3.51:

$$\Delta B_{11} = -p_{12}x_1\int_{-a}^{a}\left[\frac{\partial^2 u}{\partial x_2^2} + \frac{\partial u^2}{\partial x_3^2}\right]dx_2 = \frac{16Mx_1p_{12}}{3b^2} \qquad 3.73$$

$$\Delta B_{22} = -x_1\int_{-a}^{a}\left[[+]p\frac{\partial^2 u}{\partial x_2^2} + [-]p\frac{\partial u^2}{\partial x_3^2}\right]dx_2 = \frac{16Mx_1[-]}{3b^2} \qquad 3.74$$

$$\Delta B_{33} = -x_1\int_{-a}^{a}\left[[-]p\frac{\partial^2 u}{\partial x_2^2} + [+]p\frac{\partial u^2}{\partial x_3^2}\right]dx_2 = \frac{16Mx_1[+]}{3b^2} \qquad 3.75$$

$$\Delta B_{23} = -x_1(-)p\int_{-a}^{a}\frac{\partial^2 u}{\partial x_2 \partial x_3}dx_2 = 0 \qquad 3.76$$

$$\Delta B_{13} = \Delta B_{12} = 0 \qquad 3.77$$

One of the clearest ways to view the effects of a perturbation of refractive index in a material is to introduce the concept of an indicatrix ellipsoid[11]. The general geometry of the ellipsoid is described by the following equation:

$$B_{ij}x_ix_j = 1 \qquad 3.78$$

where B is related to the refractive index by Eqn.3.59.

A specific, simple, example will serve to describe its implementation:

$$\frac{1}{n_x^2} x^2 + \frac{1}{n_y^2} y^2 + \frac{1}{n_z^2} z^2 = 1 \qquad 3.79$$

To determine the refractive index experienced by the light, one considers the plane perpendicular to the direction of travel and its intersection with the index ellipsoid. Consider light travelling in the z– direction, Fig.3.4. The refractive index is taken as the length of the line from the origin to the intersection with the ellipsoid, in the direction of the electric vector. Thus Eqn.3.79 can be interpreted as follows: For light travelling in the z– direction, polarisation in the x– direction sees a refractive index n_x while that polarised in the y– direction sees an index n_y.

Unstressed GaAs is optically isotropic i.e the refractive index seen by the light is identical regardless of direction. The ellipsoid indicatrix is thus a sphere with $n_x = n_y = n_z = n_0$, where n_0 is the refractive index of the unstressed material. The indicatrix is described by a sphere:

$$\frac{1}{n_0^2} x_1^2 + \frac{1}{n_0^2} x_2^2 + \frac{1}{n_0^2} x_3^2 = 1 \qquad 3.80$$

Strain or stress present in the material results in a deformation of the indicatrix sphere into an ellipsoid. This is observed as an introduction of cross terms in Eqn.3.80:

$$B_{11}x_1^2+B_{22}x_2^2+B_{33}x_3^2+2B_{23}x_2x_3+2B_{13}x_1x_3+2B_{12}x_1x_2=1 \qquad 3.81$$

Substituting Eqns.3.73– 77 gives the indicatrix ellipsoid when pressure is applied to the membrane:

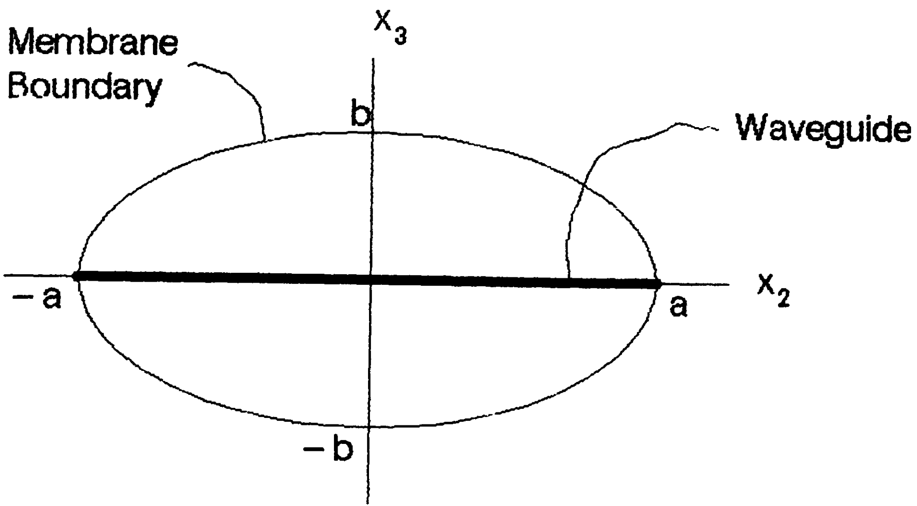

Fig.3.3

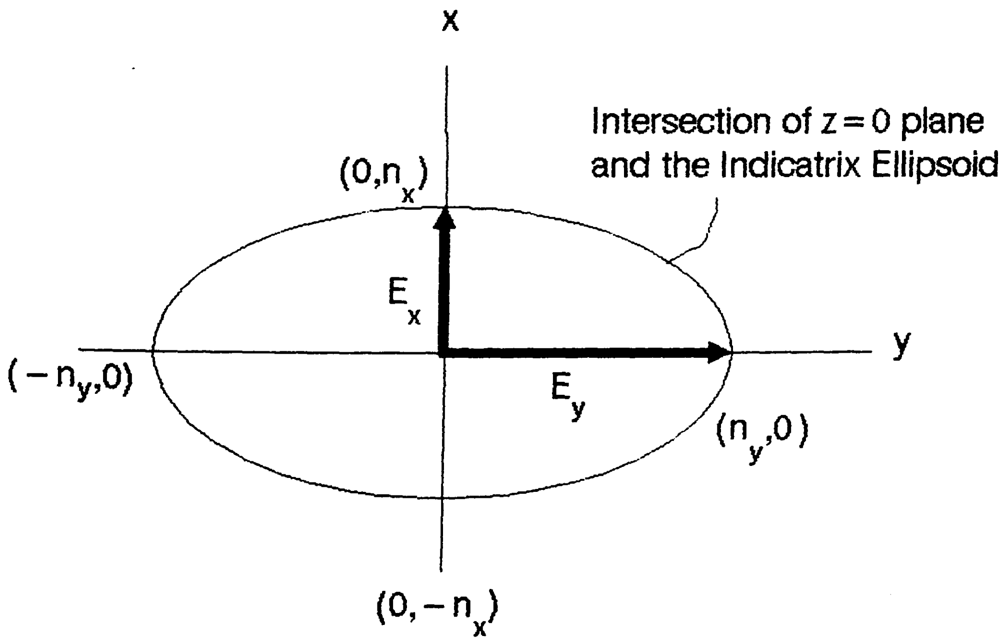

Fig.3.4

$$(B_{11}+\Delta B_{11})x_1^2+(B_{22}+\Delta B_{22})x_2^2+(B_{33}+\Delta B_{33})x_3^2 = 1 \qquad 3.82$$

This is no longer the sphere characteristic of GaAs, as given in Eqn.3.80. The strain has deformed the sphere into an ellipse whose axes still coincide with the membrane coordinate axes x_1,x_2,x_3 (i.e no cross terms). For the guide running along the major axis of the membrane, Fig.3.3, light polarised along the x_3 axis in the plane of the membrane (TE polarised), experieneces a new refractive index given by $B_{33}+\Delta B_{33}$, while light polarised along the x_1 axis perpendicular to the membrane plane (TM polarised), experiences a refractive index given by $B_{11}+\Delta B_{11}$. For unstressed material, $B_{11}=B_{33}=B_0=1/n_0^2$. Thus:

$$\frac{1}{n_{TE}^2} = \frac{1}{n_0^2} + \Delta B_{33} \qquad 3.83$$

$$\frac{1}{n_{TM}^2} = \frac{1}{n_0^2} + \Delta B_{11} \qquad 3.84$$

For small changes in refractive index Eqns.3.83–84 lead to:

$$\Delta n_{TE} = -\frac{n_0^3}{2}\Delta B_{33} \qquad 3.85$$

$$\Delta n_{TM} = -\frac{n_0^3}{2}\Delta B_{11} \qquad 3.86$$

Substituting Eqns.3.73–77 into Eqns.3.85–86 provides the refractive index changes, expressed in terms of the photoelastic constants and membrane dimensions, using Eqn.3.73–74 into Eqns.3.85–86:

$$\Delta n_{TE} = -\frac{4n_0^3 M x_1 [+]}{3b^2} \qquad 3.87$$

$$\Delta n_{TM} = -\frac{4n_0^3 M x_1 p_{12}}{3b^2} \qquad 3.88$$

where M is given by Eqn.3.52 and x_1 is the distance of the guide from the middle plane. In GaAs, guides are normally formed on the surface of the material so it is correct to set $x_1 = \frac{1}{2}h$. Substituting for both x_1 and M leads to:

$$\Delta n_{TE} = \frac{n_0^3[\frac{1}{2}(p_{11}+p_{12})+p_{44}]P}{b^2h^2\left[\frac{3A}{a^4} + \frac{2B}{a^2b^2} + \frac{3A}{b^4}\right]} \qquad 3.89$$

$$\Delta n_{TM} = \frac{n_0^3 p_{12} P}{b^2h^2\left[\frac{3A}{a^4} + \frac{2B}{a^2b^2} + \frac{3A}{b^4}\right]} \qquad 3.90$$

Assuming that the change of phase experienced by the light travelling in the guide of Fig.3.3, is totally accounted for within the refractive index change, then the phase change in crossing the membrane is given by $\Delta\varphi_n = kl\Delta n$, where $l = 2a$ and k is the wave number of the light. The final phase change experienced by the TE and TM modes, due to stress induced changes in the refractive index of the material, for a path length of 2a is given by:

$$\Delta\varphi_{TE} = \frac{2kan_0^3[\frac{1}{2}(p_{11}+p_{12})+p_{44}]P}{b^2h^2\left[\frac{3A}{a^4} + \frac{2B}{a^2b^2} + \frac{3A}{b^4}\right]} \qquad 3.91$$

$$\Delta\varphi_{TM} = \frac{2kan_0^3 p_{12} P}{b^2h^2\left[\frac{3A}{a^4} + \frac{2B}{a^2b^2} + \frac{3A}{b^4}\right]} \qquad 3.92$$

3.8.2 Phase Shifts due to Changes in Path Length

The phase-shift due to a path length change is given by $\Delta\varphi_l = kn\Delta l$. Consider, as in the last section a guide of length 2a, Fig.3.3. The length of the deflection curve, Eqn.3.53, along the x_2 axis can be obtained from the line integral:

$$\Delta l = 2\int_0^a \left[1 + \left[\frac{du}{dx_2}\right]^2\right]^{\frac{1}{2}} dx_2 = \frac{128M^2}{105a} \qquad 3.93$$

This corresponds to a phase change which is identical for both TE and TM:

$$\Delta\varphi_1 = \frac{128kn_0}{105a}\left[\frac{3P}{2h^3\left[\frac{3A}{a^4} + \frac{2B}{a^2b^2} + \frac{3A}{b^4}\right]}\right]^2 \qquad 3.94$$

3.9 Numerical Evaluation

Two membrane characteristics are given below based on calculations using the elastic compliances of GaAs[12] ($s_{11}=1.17\text{x}10^{-11}$, $s_{12}=-3.64\text{x}10^{-12}$ and $s_{44}=1.68\text{x}10^{-11}\text{Nm}^{-2}$, Eqn.3.48–49). The values for AlAs[13], differ by approximately 2% and, assuming a linear relation between the GaAs and AlAs values, indicates that the variation of the compliances with the aluminium concentration used is negligible. The photoelastic constants for GaAs[14] ($p_{11}=-0.165$, $p_{12}=-0.14$ and $p_{44}=-0.072$) are also used in the calculations.

Fig.3.5 is a diagrammatical representation of the magnitude of the strain components, e_{22}, e_{33} and e_{23} over the surface of a membrane of major and minor axes a and b respectively, where a=b for the plots indicated. The membrane displacement $u=u_1$ (Eqn.3.53) is subdivided into Eqns.3.15–17 and evaluated at the membrane surface ($x_1=\frac{1}{2}h$). There are two points to note:

(1) Along the major and minor axes, there is no shear strain ($e_{23}=0$) as indicated in the diagram.

(2) For a waveguide along the major axis, Fig.3.3, the strain e_{33} maintains the same sign along the axis, Fig.3.6a, but the e_{22} strain undergoes a change of sign, Fig.3.6b.

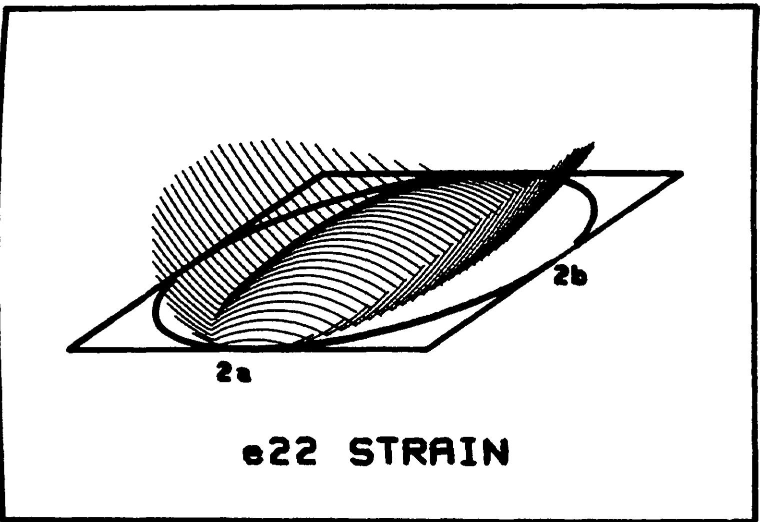

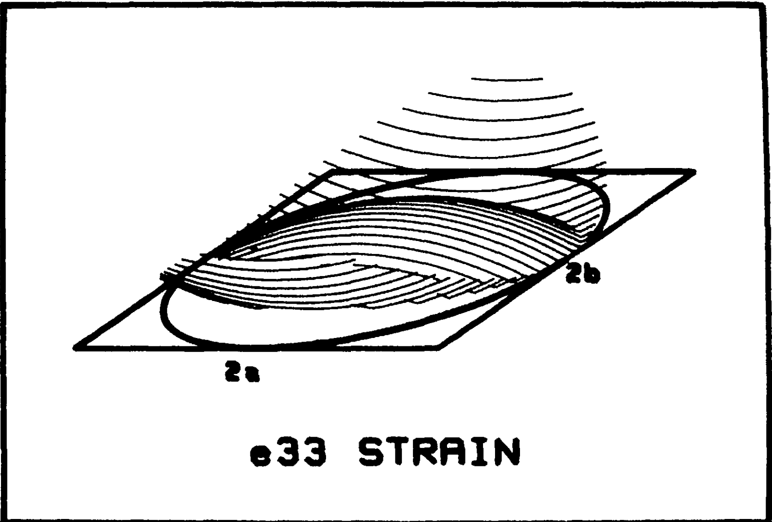

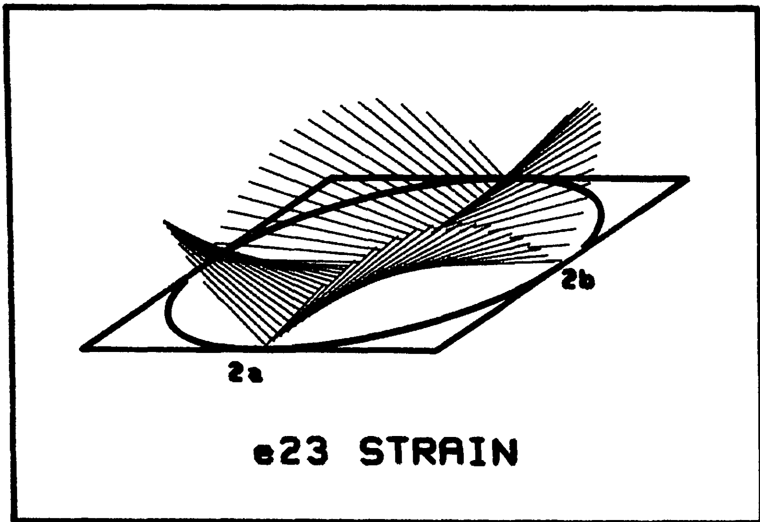

Fig.3.5

Magnitude of the Strain Components

at the Surface of a Membrane

3.9.1 Membrane for the Mach–Zehnder Pressure Sensor

Membrane Dimensions: $2a=3mm$, $2b=300\mu m$ and $h=10\mu m$

These dimensions are chosen to match those of the Mach–Zehnder pressure sensor proposed in Sec.2.7. The separation of the Mach–Zehnder interferometer arms allows one arm to run along the major axis of the membrane while the other remains free of the stress effects. The calculations below indicate that the device permits observable changes of phase for the experimental apparatus described in Chap.5.

Since $2a=3000\mu m$ and $2b=300\mu m$, the magnitudes of the e_{33} and e_{22} strains are quite different, Figs.3.6a–b. These plots show the strain at various points along the major axis where $x_2=0$ is the centre of the membrane and $x_2=a=1.5mm$ is the membrane edge. For a pressure of 100kPa ($\simeq$1atm) the central strain $e_{33}=-2.88\times10^{-4}$ and $e_{22}=-2.88\times10^{-6}$. Substitution of the membrane deflection, Eqn.3.53, into Eqns.3.15–17 reveal that $e_{33}/e_{22}=a^2/b^2$ and hence the difference in the magnitudes.

The membrane stresses experienced by a guide along the major axis are plotted in Figs.3.7a–b, and, unlike the strain components, have approximately the same magnitudes and signs. Eqns.3.32–33 show that the stress depends on a linear combination of e_{22} and e_{33} and, since $e_{22} \gg e_{33}$, the e_{33} strain dominates the σ_{22} and σ_{33} values.

Figs.3.8a–b gives the changes in index experienced by the light in the waveguide along the major axis. For both TE and TM polarisations, the largest changes in index are experienced at the membrane centre

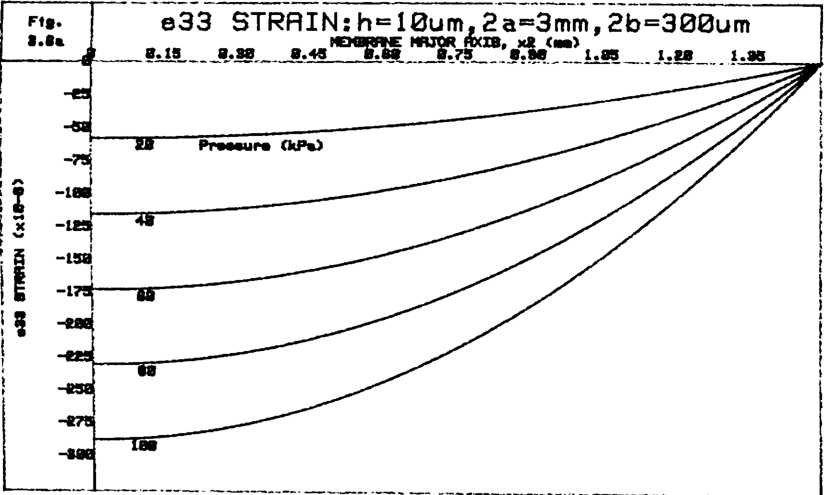
Fig. 3.6a
e33 STRAIN:h=10um,2a=3mm,2b=300um
MEMBRANE MAJOR AXIS, x2 (mm)
0.15 0.30 0.45 0.60 0.75 0.90 1.05 1.20 1.35
e33 STRAIN (x10-6)
0 -25 -50 -75 -100 -125 -150 -175 -200 -225 -250 -275 -300
Pressure (kPa)
20 40 60 80 100

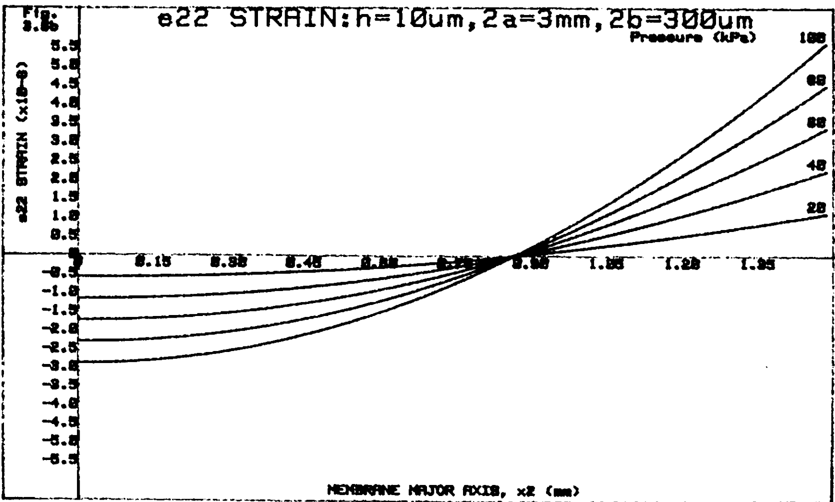
Fig. 3.6b
e22 STRAIN:h=10um,2a=3mm,2b=300um
Pressure (kPa)
100 80 60 40 20
e22 STRAIN (x10-6)
5.5 5.0 4.5 4.0 3.5 3.0 2.5 2.0 1.5 1.0 0.5 0 -0.5 -1.0 -1.5 -2.0 -2.5 -3.0 -3.5 -4.0 -4.5 -5.0 -5.5
0.15 0.30 0.45 0.60 0.75 0.90 1.05 1.20 1.35
MEMBRANE MAJOR AXIS, x2 (mm)

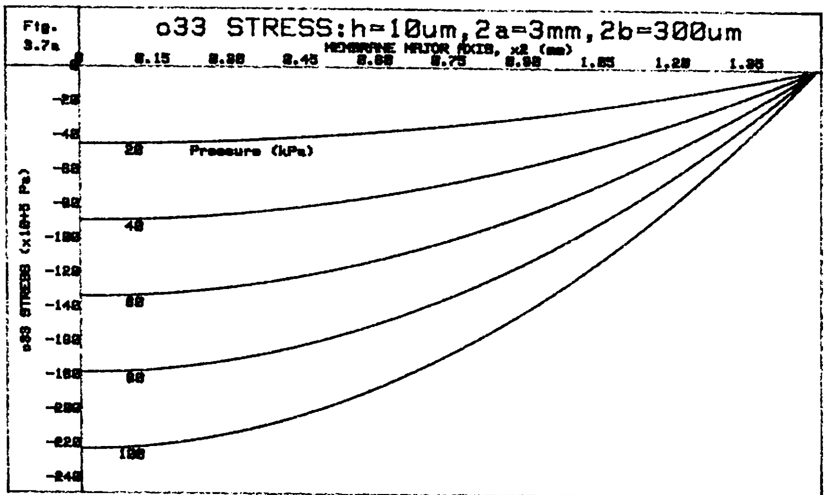
Fig. 3.7a
o33 STRESS:h=10um,2a=3mm,2b=300um
MEMBRANE MAJOR AXIS, x2 (mm)
0.15 0.30 0.45 0.60 0.75 0.90 1.05 1.20 1.35
o33 STRESS (x10+5 Pa)
0 -20 -40 -60 -80 -100 -120 -140 -160 -180 -200 -220 -240
Pressure (kPa)
20 40 60 80 100

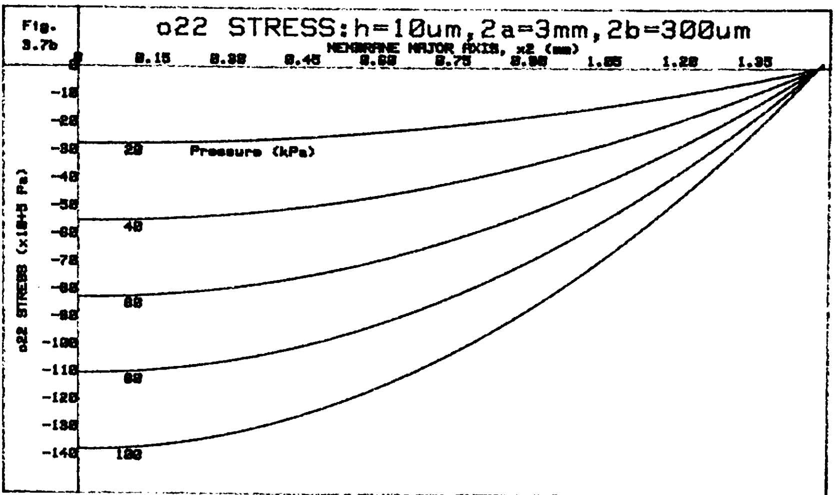
Fig. 3.7b
o22 STRESS:h=10um,2a=3mm,2b=300um
MEMBRANE MAJOR AXIS, x2 (mm)
0.15 0.30 0.45 0.60 0.75 0.90 1.05 1.20 1.35
o22 STRESS (x10+5 Pa)
0 -10 -20 -30 -40 -50 -60 -70 -80 -90 -100 -110 -120 -130 -140
Pressure (kPa)
20 40 60 80 100

($x_2=0$) but the index variation for TE modes is slightly larger than that for TM. The negative changes imply that the membrane top surface is in a state of in-plane compression.

Figs.3.9a-b are plots of the stress-induced phase-shift in the TE and TM modes for a range of values of the major axis. With $2b=300\mu m$, the major axis is plotted from $2a=300\mu m$ (i.e a circular membrane) to $2a=3mm$. The phase changes due to the change in length are negligible for the pressure ranges considered. For a pressure of 100kPa ($\triangleq$1atm) the phase-shift for TE and TM modes are 12 radians and 8 radians respectively. Thus using TE excitation of the Mach-Zehnder pressure sensor (Sec.2.7) produces a phase change of approximately 4π radians, i.e two cycles, for a 1atm pressure differential across the membrane.

3.9.2 Membrane for the Birefringent Pressure Sensor

Membrane Dimensions: $2a=2mm$, $2b=8mm$ *and* $h=25\mu m$

This device is designed to operate using only straight wavguides and relies on the difference between TE and TM phase-shifts. TE and TM polarisations are equally excited using linearly polarised light, Sec.5.5. Thus the phase-shifts between the TE and TM components, entering the device, can be taken as zero. It is assumed that the light losses experienced by the TE and TM polarisations in the device are equal. After passing through the device, a phase-shift occurs between TE and TM modes which implies that the light is, in general, elliptically polarised[15]. If the device output is viewed through a polariser aligned with that at the input, the change from linear to elliptical polarisation is observed as a change of amplitude at the output. There are two main conditions to note:

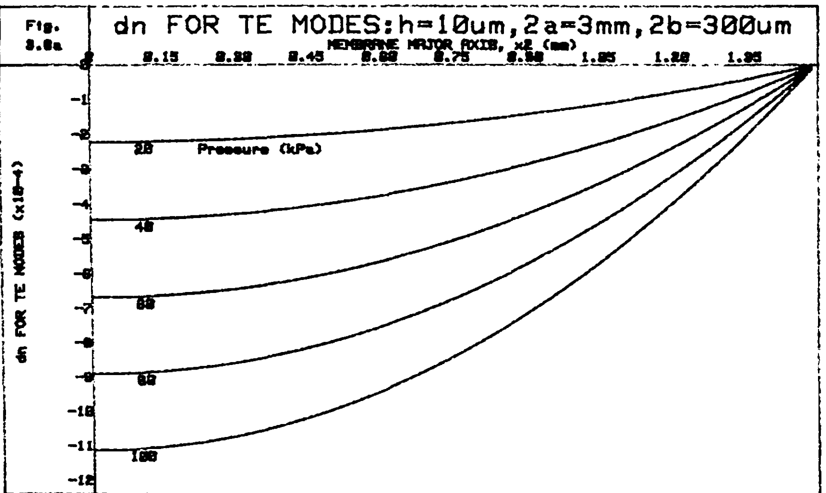
dn FOR TE MODES: h=10um, 2a=3mm, 2b=300um
MEMBRANE MAJOR AXIS, x2 (mm)
dn FOR TE MODES (x10-4)
Pressure (kPa)
20
40
60
80
100

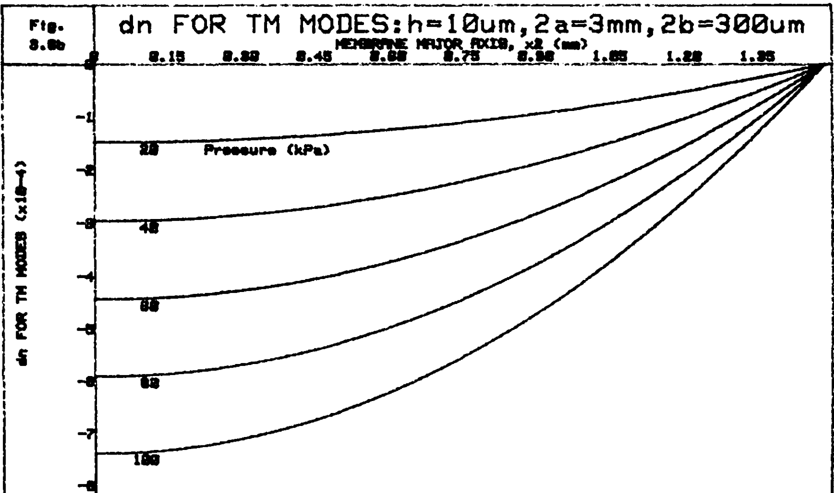
dn FOR TM MODES: h=10um, 2a=3mm, 2b=300um
MEMBRANE MAJOR AXIS, x2 (mm)
dn FOR TM MODES (x10-4)
Pressure (kPa)
20
40
60
80
100

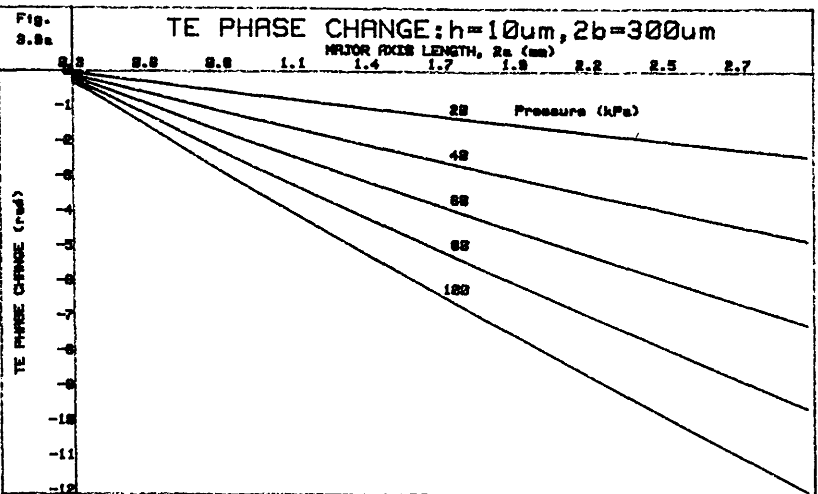
TE PHASE CHANGE: h=10um, 2b=300um
MAJOR AXIS LENGTH, 2a (mm)
TE PHASE CHANGE (rad)
Pressure (kPa)
20
40
60
80
100

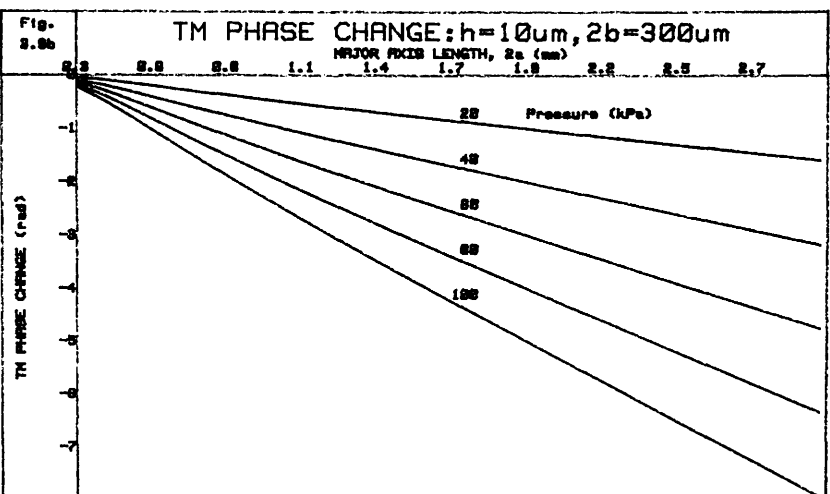
TM PHASE CHANGE: h=10um, 2b=300um
MAJOR AXIS LENGTH, 2a (mm)
TM PHASE CHANGE (rad)
Pressure (kPa)
20
40
60
80
100

(1) A phase difference of $\frac{1}{2}\pi$ produces circularly polarised light.

(2) A phase difference of π produces light linearly polarised at 90° to that at the input.

All values between those given above are elliptically polarised.

For the membrane dimensions 2mm x 8mm x 25μm a phase-shift of 1.5 radians is predicted for the TE and TM polarisations respectively. This leads to a relative phase-shift of 0.9 radians between the TE and TM polarisations (i.e 0.3π) is predicted for a change in pressure of 0.69atm. This pressure is the maximum actually achieved in the experimental apparatus described in Chap.5, where this theoretical prediction is compared experiments carried out for membranes actually fabricated.

3.10 Summary

A mathematical theory of elasticity is developed to model:

(1) the deflection of a membrane due to a uniform pressure differential across its thin dimension and

(2) the phase-shifts experienced by TE and TM polarisations in a straight waveguide crossing a membrane.

Calculations were carried out for a birefringent pressure sensor consisting of straight waveguides crossing the 2mm dimension of a 2mm x 8mm x 25μm membrane. Predicted phase-shifts of 2.4 radians and 1.5 radians for TE and TM modes are expected for an applied pressure of 69kPa. Hence the relative phase change between TE and TM is 0.9 radians (0.3π) for the birefringent pressure sensor. Experimental results for devices actually fabricated are given in Chap.5.

A membrane dimension of 3mm x 300μm x 10μm is proposed for the Mach–Zehnder interferometric sensor described in Sec.2.7.2. The sensing arm would be arranged along the 3mm dimension and in the centre of the membrane. The theoretical prediction for the phase–shifts experienced by TE modes in the sensing arm is 12 radians when a pressure of 1 atm is applied to the membrane. Assuming a detection limit of 10^{-6} radians (a literature standard) the sensitivity of the Mach–Zehnder pressure sensor is 8mPa.

Appendix A

The stiffness and compliance tensors of a crystal:

$$\begin{bmatrix}\sigma_{11}\\ \sigma_{22}\\ \sigma_{33}\\ \sigma_{23}\\ \sigma_{13}\\ \sigma_{12}\end{bmatrix}=\begin{bmatrix}c_{1111} & c_{1122} & c_{1133} & 2c_{1123} & 2c_{1113} & 2c_{1112}\\ c_{2211} & c_{2222} & c_{2233} & 2c_{2223} & 2c_{2213} & 2c_{2212}\\ c_{3311} & c_{3322} & c_{3333} & 2c_{3323} & 2c_{3313} & 2c_{3312}\\ c_{2311} & c_{2322} & c_{2333} & 2c_{2323} & 2c_{2313} & 2c_{2312}\\ c_{1311} & c_{1322} & c_{1333} & 2c_{1323} & 2c_{1313} & 2c_{1312}\\ c_{1211} & c_{1222} & c_{1233} & 2c_{1223} & 2c_{1213} & 2c_{1212}\end{bmatrix}\begin{bmatrix}e_{11}\\ e_{22}\\ e_{33}\\ e_{23}\\ e_{13}\\ e_{12}\end{bmatrix}$$

A.1

where $c_{ijkl}=c_{klji}$. The strain–stress relation is identical in form:

$$\begin{bmatrix}e_{11}\\ e_{22}\\ e_{33}\\ e_{23}\\ e_{13}\\ e_{12}\end{bmatrix}=\begin{bmatrix}s_{1111} & s_{1122} & s_{1133} & 2s_{1123} & 2s_{1113} & 2s_{1112}\\ s_{2211} & s_{2222} & s_{2233} & 2s_{2223} & 2s_{2213} & 2s_{2212}\\ s_{3311} & s_{3322} & s_{3333} & 2s_{3323} & 2s_{3313} & 2s_{3312}\\ s_{2311} & s_{2322} & s_{2333} & 2s_{2323} & 2s_{2313} & 2s_{2312}\\ s_{1311} & s_{1322} & s_{1333} & 2s_{1323} & 2s_{1313} & 2s_{1312}\\ s_{1211} & s_{1222} & s_{1233} & 2s_{1223} & 2s_{1213} & 2s_{1212}\end{bmatrix}\begin{bmatrix}\sigma_{11}\\ \sigma_{22}\\ \sigma_{33}\\ \sigma_{23}\\ \sigma_{13}\\ \sigma_{12}\end{bmatrix}$$

A.2

The factors of two are generated when equal components are taken into account in the full tensor expansion e.g:

$$\sigma_{11}=...+c_{1123}e_{23}+c_{1132}e_{32}+...=2c_{1123}e_{23} \qquad \text{A.3}$$

where, due to symmetry, $c_{ijkl}=c_{ijlk}$ and $e_{ij}=e_{ji}$.

References

[3.1] KIRKBY, P.A., SELWAY, P.R. and WESTBROOK, L.D.:'Photoelastic Waveguides and their Effect on Stripe-geometry GaAs/$Ga_{1-x}Al_xAs$ Lasers', Journal of Applied Physics, **50**, No.7, pp45674579, 1979

[3.2] YAMANOUCHI, K., WAKAZONO, K. and SHIBAYAMA, K.:'Optical Surface Wave Mode Converters and Modulators Utilizing Static Strain-Optic Effects', IEEE Journal of Quantum Electronics, **QE-16**, No.6, pp628-634, 1980

[3.3] SCHMIDT, R.V.:'Acoustooptic Interactions Between Guided Optical Waves and Acoustic Surface Waves', IEEE Transactions on Sonics and Ultrasonics, **SU-23**, No.1, pp22-33, 1976

[3.4] WEISS, J.D.:'Dielectric-waveguide Strain Guage: A Theoretical Study', Journal of the Optical Society of America, **11**, No.11, pp1941-1947, 1986

[3.5] HOCKER, G.B.:'Fiber-optic Acoustic Sensors with Increased Sensitivity by use of Composite Structures', Optics Letters, **4**, No.10, pp320-321, 1979

[3.6] CULSHAW, B., DAVIES, D.E.N. and KINGSLEY, S.A.:'Acoustic Sensitivity of Optical-fibre Waveguides', Electronics Letters, **13**, No.25, pp760-761, 1977

[3.7] BUCARO, J.A., DARDY, H.D. and CAROME, E.F.:'Fibre-optic Hydrophone', Journal of the Acoustic Society of America, **62**, No.5, pp1302-1304, 1977

[3.8] COLE, J.H., JOHNSON, R.L. and BHUTA, P.G.:'Fiber-Optic Detection of Sound', Journal of the Acoustic Society of America, **62**, No.5, pp1136-1138, 1977

[3.9] OSBOURN, G.C.:'Strain-Layer Superlattices:A Brief Review', IEEE Journal of Quantum Electronics, **QE-22**, No.9, 1986

[3.10] Saada, A.S.:"Elasticity: Theory and Applications". New York, Oxford Pergamon Press, 1974.

[3.11] Nye, J.F.:"Physical properties of Crystals and their Representation by Tensors and Matrices". Oxford Clarendon Press, 1985.

[3.12] BLAKEMORE, J.S.:", Journal of Applied Physics, **53**, No.10, ppR1-R181, 1982

[3.13] ADACHI, S.:'GaAs, AlAs and $Al_xGa_{1-x}As$:Material Parameters for use in Research and Device Applications', Journal of Applied Physics, **58**, No.3, ppR1-R29, 1985

[3.14] DIXON, R.W.:'Photoelastic Properties of Selected Materials and Their Relevance for Applications to Acoustic Light Modulators and Scanners', Journal of Applied Physics, **38**, No.13, pp5149-5153, 1967

[3.15] WHELAN, P.M. and HODGSON, M.J.:'Essential Principles of Physics', J.W. Arrowsmith Ltd, 1978

[3.16] ISAAC, J.J, De La RUE, R.M. and WONG, K.K.:'An Integrated Optical Pressure Sensor in III-V Material', Proceedings of the Fourth European Conference on Integrated Optics, pp213-216, Glasgow 1987

CHAPTER FOUR

Device Fabrication by Wet and Dry Chemical Etching

4.1 Introduction

The aim in this chapter is to describe the fabrication techniques for an optical pressure sensor realised in the GaAs/AlGaAs ternary system. Both waveguides and membranes were fabricated using wet chemical etching. However, due to the extensive etch depths required to form membranes (400μm), dry etching was restricted to waveguide fabrication. The final section of this chapter describes the alignment of an optical waveguide on the top surface of a wafer with a membrane window on the back surface. When possible, reference is made to practical work in order to give some idea of typical orders of magnitudes for etch rates, membrane areas, ridge widths etc, as well as some of the underlying difficulties that may be encountered during fabrication.

4.2 Chemical Etchant Systems For GaAs/AlGaAs

Breaking the strong covalent bonds in the zinc-blende lattices of III-V semiconductor materials usually requires the use of an oxidising agent. The methods for dealing with the solid etch products produced by wet and dry etching are quite different. In wet chemical etching the redox reaction process involves the conversion of GaAs to a higher oxidation state which is soluble in the liquid etchant system. Dry etching occurs in a gaseous environment and thus requires etch products which are volatile and hence leave the surface clear for further etching.

4.2.1 Wet Chemical Etching

Redox Reaction

The oxides of gallium, which include Ga_2O_3, $Ga_2O_3(H_2O)$ and Ga_2O (a suboxide) are all amphoteric i.e soluble in both acidic and alkaline solutions, but insoluble in water. They also dissolve in some organic solvents such as methanol[1]. The oxides of arsenic are As_2O_3 and As_2O_5 which are highly soluble in water, forming arsenic acid. The more common oxidising agents include hydrogen peroxide, H_2O_2, nitric acid[2], HNO_3, cromates[3], $Cr_2O_7^-$, and the halides[4], Br^-. Some acids or alkalis added to the oxidants act as complexing agents allowing the formation of a stable complex ion or molecule with the oxides, which then become soluble in the etchant medium. For example, when using hydrogen peroxide, as the oxidant, adding sulphuric acid, H_2SO_4, or ammonium hydroxide, NH_3OH, will ensure the oxidation and dissolution of the gallium.

Experiments carried out by Tijburg et al[5] have shown interesting features in the behaviour of AlGaAs in varying pH solutions. There are marked variation in the etch rate of an oxidising solution with the concentration of aluminium in AlGaAs which has been termed selectivity. Using GaAs and $Al_{0.3}Ga_{0.7}As$, i.e material with 30% aluminium in GaAs, the following trends were observed[5]:

$pH > 9$: Etch rate of GaAs is much greater than the etch rate of $Al_{0.3}Ga_{0.7}As$ i.e GaAs is etched selectively with respect to $Al_{0.3}Ga_{0.7}As$.

$5 < pH < 9$: $Al_{0.3}Ga_{0.7}As$ is etched selectively with respect to GaAs.

$pH < 5$: There appears to be no selectivity.

This property was used in membrane fabrication and is discussed in

Sec.4.5.

Photoresist Mask – AZ1450J

The photoresist, AZ1450J, is used as a mask for many wet-chemical etching systems. There are a number of disadvantages, but these can be allowed for. The mask is attacked to some extent by alkaline solutions[15] (it should be noted that the developers used are themselves alkalis). This attack takes the form of a migration of adsorbed etchant molecules within the mask, weakening it internally, and is dependent on the duration of contact between the mask and solution. In addition, a phenomenon known as undercutting[7] occurs since there are no chemical bonds at the mask/substrate interface. Interfacial adhesion is maintained by van der Waals forces. The species present in the etch can form stronger van der Waals bonds with either the mask or the substrate leading to migration of the etchant under the mask. This problem can be alleviated by the use of an appropriate adhesion promoter. The breakdown of large areas of photoresist[7] may be due to differential stress build-up at the substrate/mask interface. Thermal or chemical action on the mask may result in tensile stress, relative to the substrate, leading to cracking. On the other hand, if the substrate has a thermal coefficient of expansion much less than that of the mask, then the resist may expand giving rise to the formation of bubbles.

GaAs/AlGaAs Etching Solutions

The solutions used in this thesis are based on hydrogen peroxide solution for the oxidising agent, with sulphuric acid and ammonium hydroxide acting as the complexing agents. This etching system was chosen because the chemicals are readily available and are relatively safe to use. De-ionised water was used as a dilutent to control the

etch rate and quench reactions:

1. HYDROGEN PEROXIDE - H_2O_2 - 30 % (percent by weight).
2. SULPHURIC ACID - H_2SO_4 - 98 %.
3. AMMONIUM HYDROXIDE - NH_3OH - 35 %.
4. DE-IONISED WATER.

4.2.2 Dry Chemical Etching

Redox Reaction

Reactive Ion Etching (RIE) relies on a combination of ion bombardment at low power and high radio frequencies plus surface chemical reactions for the removal of material[8]. Since the fluorides of group III elements are non– volatile at practical pressures[9], etchants based on chlorine dominate this area e.g $SiCl_4$[8–10], CCl_4[11] and CCl_2F_2[12]. The volatile products $GaCl_3$.... are swept out of the etch environment using argon.

Photoresist Mask – AZ1450J

In the case of dry etching there appears to be no problem with using resist as a mask. The etch rate difference (>10:1) between GaAs and AZ1450J is sufficient to ensure that for the fabrication of most practical guides the resist is virtually unaffected. At low pressures, 20mTorr, etch profiles are vertical and no undercut occurs[10]. Increasing the pressure (40mTorr) would produce undercut and reveal crystallographic planes identical to those described in Sec.4.3.5.

4.3 Material Preparation

4.3.1 GaAs/AlGaAs Epitaxial Layers

The wafers can be grown by a number of techniques including Metal–Organic Chemical Vapour Deposition (MOCVD)[13] or Molecular Beam Epitaxy[14] (MBE). The wafers are most commonly grown with $\langle 100 \rangle$ crystal orientation which yields good quality material. Two typical epitaxial layer configurations are shown in Fig.4.1a, but the idea is identical. In both, the largest proportion of light is guided in the top layer, Fig.4.1b, and the $Al_{0.4}Ga_{0.6}As$ layers are used, in conjunction with a selective etch, to ensure that etching is effectively stopped, Fig.4.1c. The 8% Al layer, Fig.4.1a(i) forms a single–mode guide at 1.3 μm with the top layer thus serving as an effective substrate, whereas in Fig.4.1a(ii) the 40% Al layer performs the dual role of effective optical substrate and etch stop.

4.3.2 Wafer Cleavage Planes

Epitaxial layers can be grown on wafers with a range of shapes and sizes, depending both on the technique of growth and the machines available. In order to conserve material, it was necessary to divide a wafer into manageable sections upon which the fabrication process could be carried out. For this work wafers were divided into sections larger than 5x5 mm^2 but smaller than 30x34 mm^2 (limited by the MOCVD apparatus), the size depending on whether only a membrane or a complete pressure sensor was to be fabricated.

As mentioned in Sec.4.3.1, the layers were grown on the crystal orientation $\langle 100 \rangle$. The cleavage directions in the wafer plane were $\langle 011 \rangle$ and $\langle 01\bar{1} \rangle$ and were at 90° to each other. A diamond scribe was used to cut a very shallow groove on either the wafer top

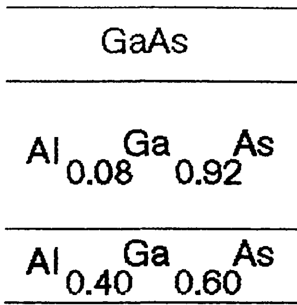

GaAs SUB

(i)

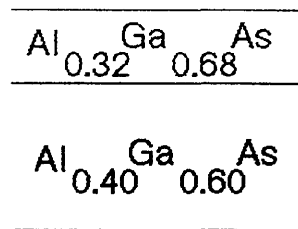

GaAs SUB

(ii)

(a)

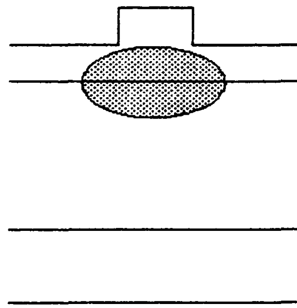

GaAs SUB

(b)

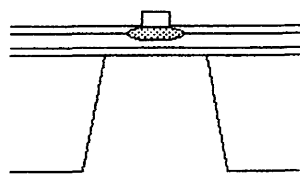

~400um

(c)

Fig.4.1

GaAs/AlGaAs Epitaxial Layers

or base along either of the <011> directions. This resulted in the wafer automatically cleaving along the groove, or doing so when the wafer was placed on a raised surface with one side of the groove supported while the other, free side, experienced an out-of-plane force. Fig.4.2 shows two techniques for cleaving, the first being the generally accepted method while the second was developed as a result of the present work. If the intention is just to cleave a wafer into smaller more manageable sections, then Fig.4.2a shows the result of scribing from one edge of the wafer to the opposite. The lattice follows the fault generated and because the diamond tip of the scriber is, atomically speaking, very large, the cleaved edge is rough to the extent that, when viewed edge on with the eye, vertical lines can be seen where different parallel planes have been followed. On the other hand, if light is to be end-fired into the wafer then a smooth cleaved edge will result in less scatter. Fig.4.2b shows that only a small nick at the wafer edge is necessary to cleave a wafer when following the procedures described above. Apart from where the scriber was used, the cleaved edge is remarkably smooth and appears mirror-perfect, even under high magnification (x500)on an optical microscope.

4.3.3 Wafer Thickness Assessment

When etching through the back of a wafer, it is crucial to know, fairly accurately, its remaining thickness. Two fairly straightforward methods both involve the use of an optical microscope and together provided a useful cross-check. The first involved focussing on a cleaved edge and using calibrated cross-wires, together with a magnification of upto 1000 times, to determine the thickness to within a $1 \mu m$. In the second, a GaAs wafer was placed flat on a

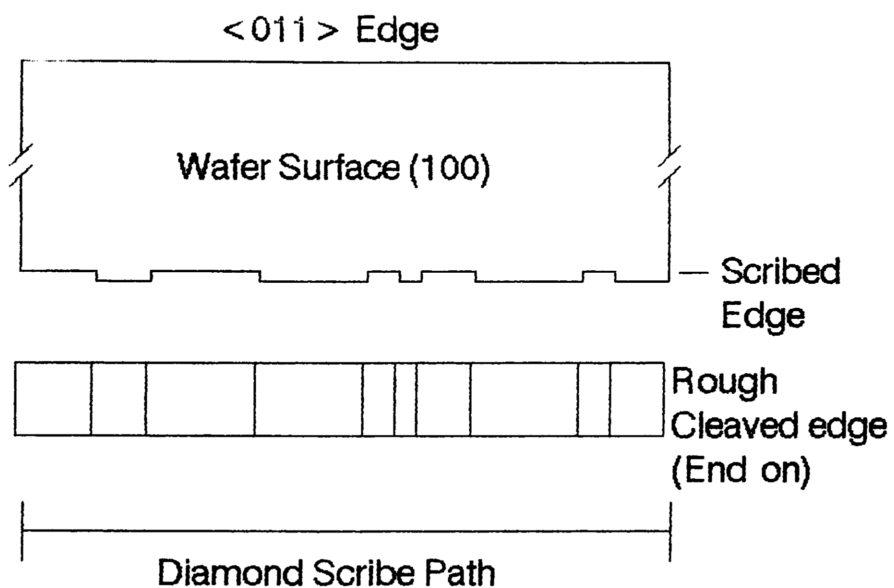

(a)

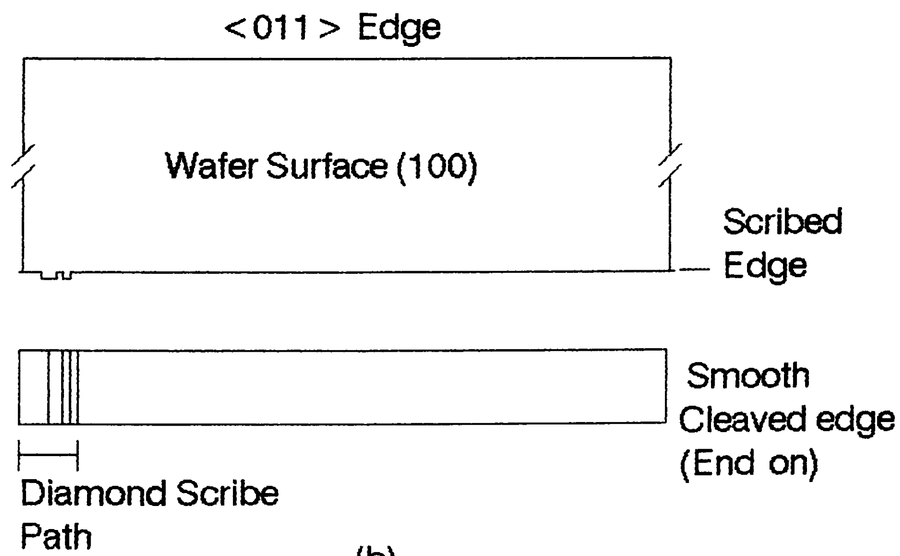

(b)

Fig.4.2

Effects of a Diamond Scribe on a Cleaved Edge

silicon wafer and focussing on the two wafer surfaces allowed the determination of the thickness to 1μm accuracy by using the vernier scale on the microscope. The average wafer thickness of the samples used was 400μm and it was found that, once the measurement was carried out for one section of a given wafer, it was unnecessary to repeat for other areas.

4.3.4 Sample Cleaning Prior To Photolithography

The most likely contaminants on a wafer are grease, or perhaps solvent or water residues. The cleaning procedure, Tricleaning, which is described in Appendix A, was sufficient for most cases and began after the wafer had been cleaved to its final size.

4.3.5 Differentiating Between $\langle 011 \rangle$ and $\langle 01\bar{1} \rangle$ Directions

For $\langle 100 \rangle$ orientation GaAs, a wafer is cleaved by scribing along the $\langle 011 \rangle$ or $\langle 01\bar{1} \rangle$ directions. Some growth facilities do provide this information in the form of an edge, to an otherwise circular wafer, the orientation of which is known. But with an already cleaved rectangular wafer, and no information, the simplest way of determining the orientation is by wet-chemical etching. Very small sections of wafer can be used – as small as 2x3 mm^2 – the only limit being the ability to cleave.

Two sections of wafer, 2x3 mm^2 were cleaved so that the longest dimension of one wafer was in either the $\langle 011 \rangle$ or $\langle 01\bar{1} \rangle$ direction while the other wafer had a long dimension perpendicular to it. Half of each wafer was coated with photoresist as shown in Fig.4.3 following the photolithographic and etching steps described in Appendix B and in Fig.4.4a. The wafers were cleaved along the dotted lines

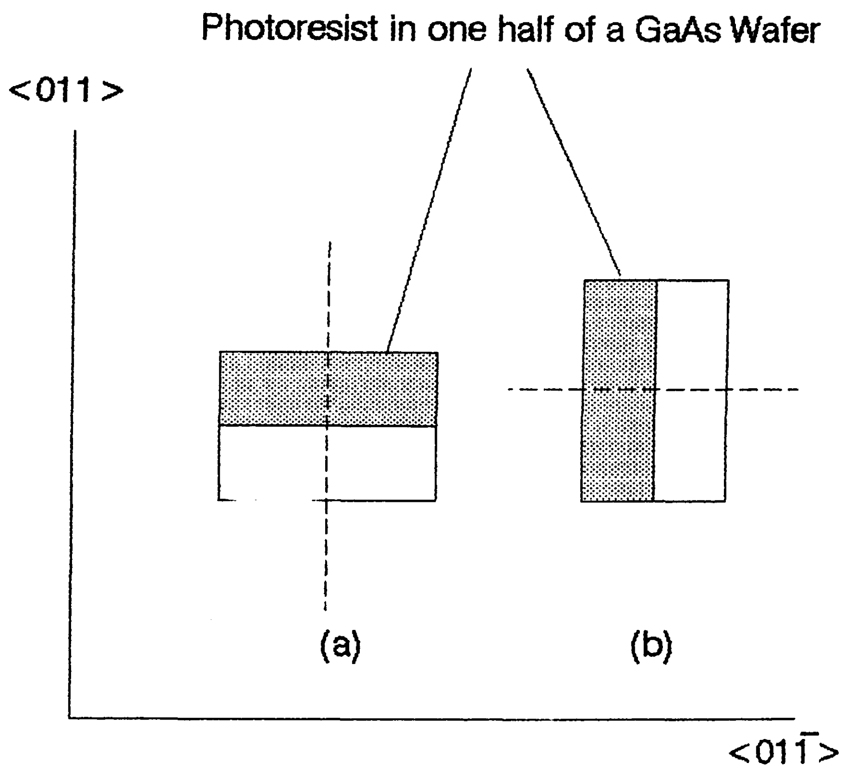

Fig.4.3

Dertermination of the Orientation of GaAs by Etching and Cleaving

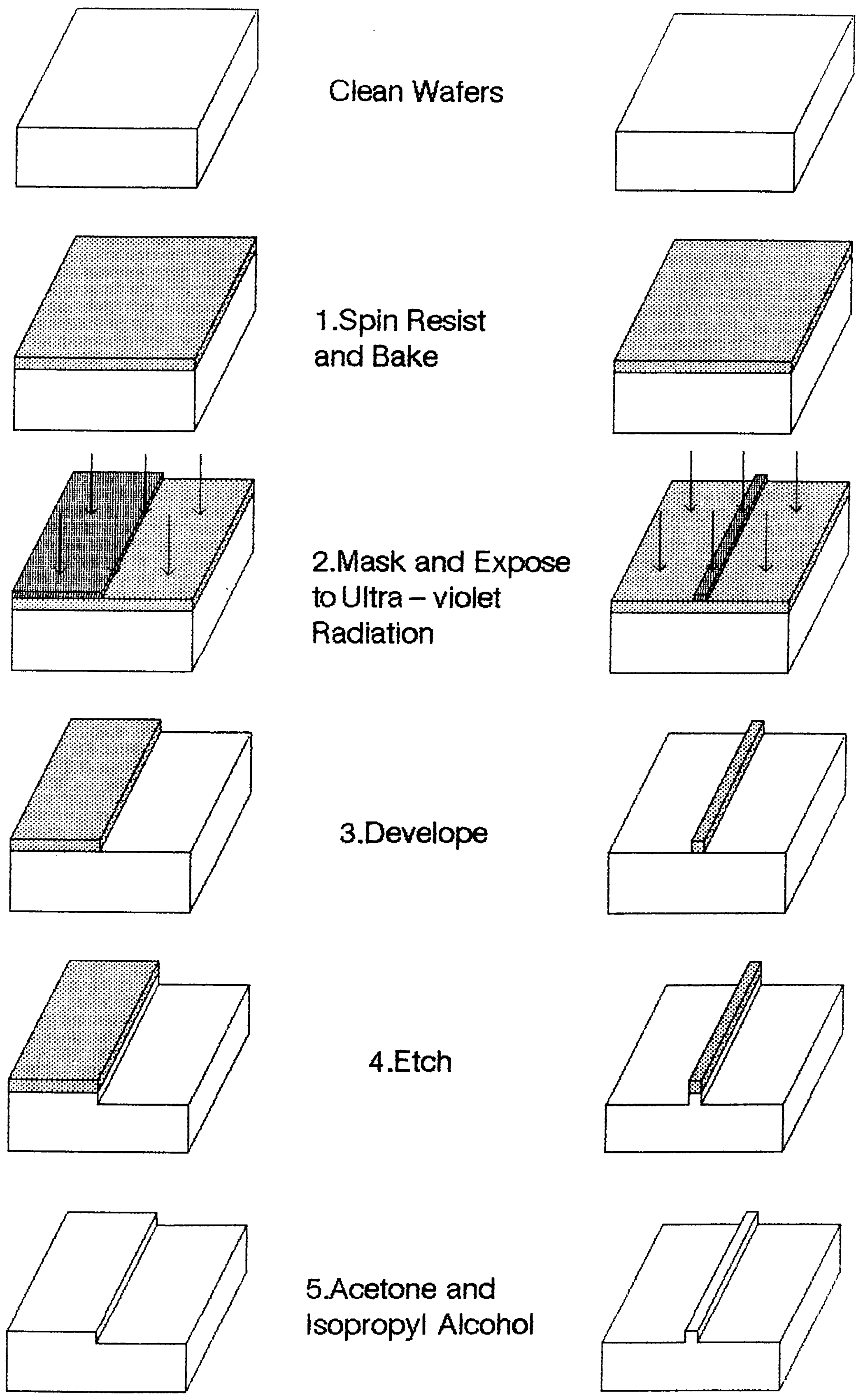

Fig.4.4

Photolithographic and Etching Processes for (a) GaAs Orientation Determination and (b) Waveguide Fabrication

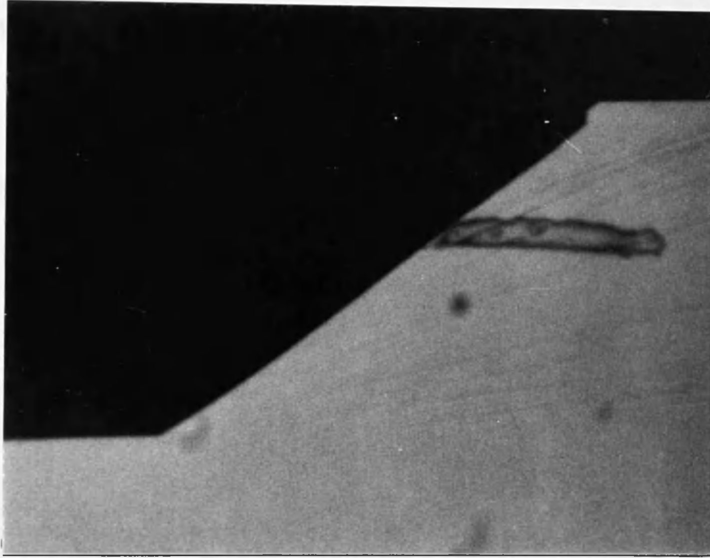

Fig.4.5a

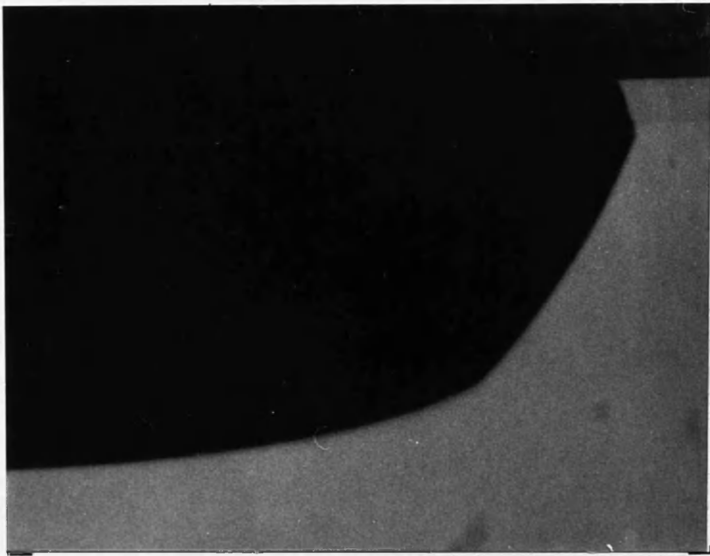

Fig.4.5b

The (a) <011> and (b) <01$\bar{1}$> cross-sections of a GaAs wafer etched with acidic hydrogen peroxide to a depth of 50μm.

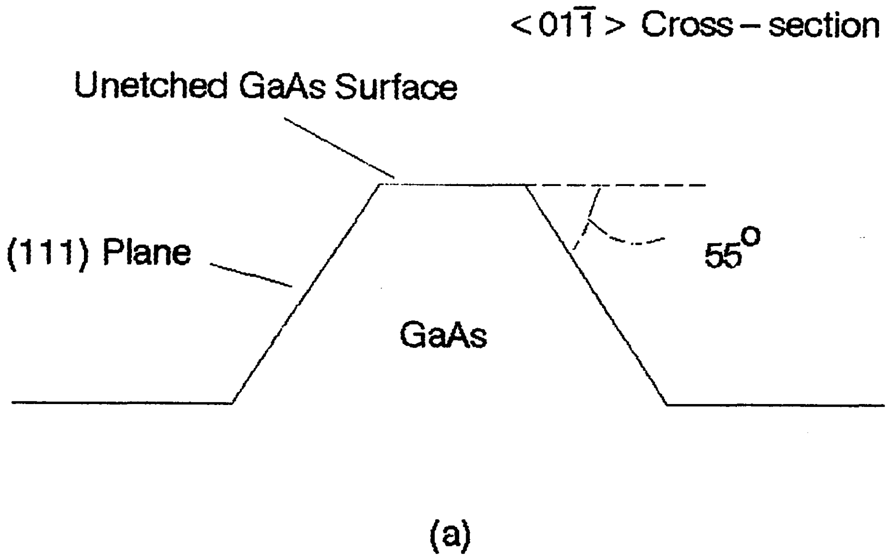

(a)

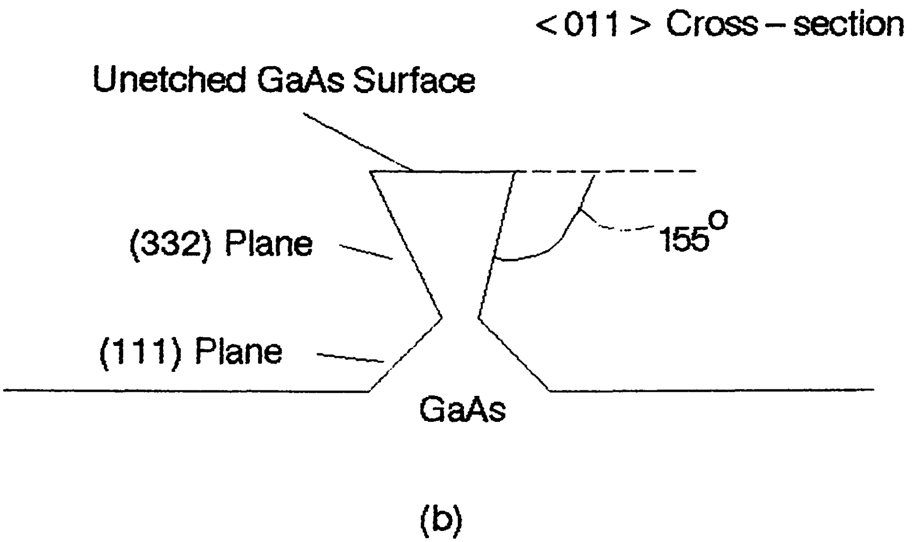

(b)

Fig.4.6

Preferential Planes Revealed in (100) GaAs when etching with Acidic Hydrogen Peroxide

shown in Fig.4.3 and the cleaved edge viewed under an optical microscope so revealing the preferential planes exposed by the etching.

Results:

Figs.4.5a–b show the etch profiles, as seen under an optical microscope, for the $\langle 01\bar{1} \rangle$ and $\langle 011 \rangle$ directions respectively. The profiles are quite different and are in good agreement with the profiles obtained by D. W. Shaw[16]. If instead of one edge, a line of photoresist is used, for example during ridge waveguide fabrication, the profiles for directions $\langle 01\bar{1} \rangle$ and $\langle 011 \rangle$ are shown respectively in Figs.4.6a–b. Ridge waveguides with the profile shown in Fig.4.5d are not normally chosen for guide fabrication (although under the right conditions guides are possible) since a narrow waist weakens the ridge especially for very narrow guides and/or too deep an etch.

The planes revealed in the $\langle 01\bar{1} \rangle$ cross section, Fig.4.6a, are the (111) planes which lie at about 55° to the horizontal. These surface planes contain only gallium or arsenic atoms triply bonded to the lattice (a single bond being very unstable). The planes containing only Ga atoms are known as (111)A and those containing only As are known as (111)B. A triply bonded gallium atom has a full outer shell which makes it a very stable entity and hence difficult to be oxidise. The gallium planes are therefore the slowest etching planes. On the other hand, the triply bonded arsenic atoms have two electrons in the outer shell which make them highly susceptible to oxidation. Once removed the next layer contains gallium atoms which are singly–bonded to the lattice and are fairly easily dislodged. Hence the planes containing only arsenic atoms are the faster etching planes. The planes revealed in the $\langle 011 \rangle$ cross section, Fig.4.6b,

are slightly more difficult to account for. Shaw[16] gives their angles as 155° to the horizontal and attributes them to (332) planes.

4.4 Waveguide Fabrication

4.4.1 Wet Chemically Etched Waveguides

The techniques described in this section are suitable for a wide range of waveguide widths. Chemical etching does have one inherent disadvantage in that the observed preferential etching using the hydrogen peroxide system will result in the walls of a curved guide having a profile which varies along its length, lying anywhere between those shown in Fig.4.6a–b. For non–prefential etching, dry etching can be used, Sec.4.4.2, or experimentation with other wet–chemical etching systems can be tried.

A variety of waveguides were etched during this project including 2μm to 10μm straight guides and Mach–Zehnder interferometers in which guide widths ranged from 2μm to 6 μm incorporating S–bends with radii of 40mm curvature providing arm separations of 300μm. Ridge heights were $\angle$ 1μm and this dictated the etch compositions. The acidic hydrogen peroxide system was used, once again selecting the etchant composition based on work done by Shaw[16] plus additional experiments to verify that the etch rates were behaving as predicted. The masks used in the photolithographic process were produced by electron beam lithography and consisted of various chrome lines and Mach–Zehnder waveguides on a glass plate. The photolithographic and etching techniques are described in Appendix C and are depicted in Fig.4.4b. The wafer ends are then cleaved in preparation for coupling light into the guides.

Results:

A number of Scanning Electron Micrographs were taken. Fig.4.7 shows both the profile and wall roughness for a $3\mu m$ wide guide etched to a depth of $0.3\mu m$. Fig.4.8 shows another guide which is $6\mu m$ wide and was etched to a depth of $0.6\mu m$. Preferential etching is clearly evident in both micrographs and reveals the (111)A Ga planes described in Sec.4.3.5 at approximately 55° to the surface.

Fig.4.9 shows the result of undercutting in both a straight waveguide and a Y−junction waveguide. The intention was to etch a $2\mu m$ wide guide in order to produce a ridge height of $1\mu m$. The result was a $0.5\mu m$ high triangular ridge, due to the etchant migrating under the photoresist mask and finally lifting it completely. The preferential planes are still intact but the top of the ridge narrows until it forms a point. Shaw[16] found that for every micron etched, there is a corresponding $0.94\mu m$ of undercut for the particular etchant composition used − almost a 1:1 ratio. Wider lines and/or shallower etches alleviate the problem. In Fig.4.10 two Y−junctions formed by $3\mu m$ and $6\mu m$ wide waveguides, are shown etched to a ridge height of $0.3\mu m$ and the morphology of the guide surface and the ridge walls is very good.

4.4.2 Reactive Ion Etched Waveguides

Straight waveguides and Y−junctions etched using dry etching have the inherent advantage of vertical wall profiles. This is especially important for the S−bends of the Y−junctions where the guide profile remains intact throughout the curved sections of the guides. Figs.4.11a−b show typical dry−etched waveguides characterised by their vertical walls (cf Figs.4.7−8). Fig.12 shows a Y−junction

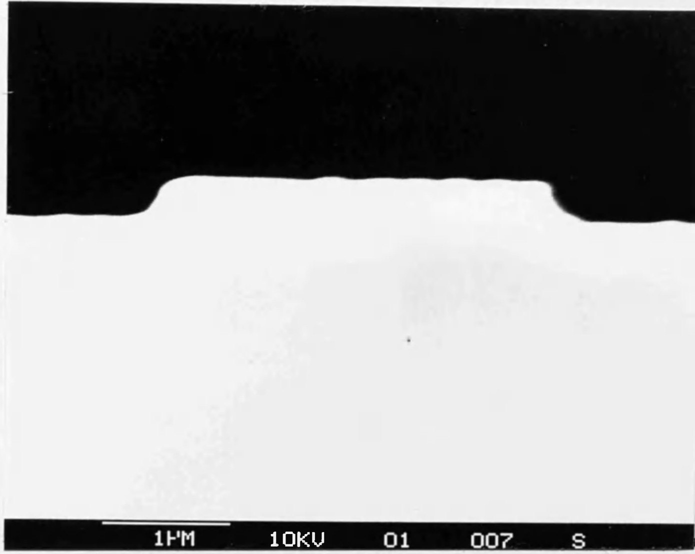

Fig.4.7a

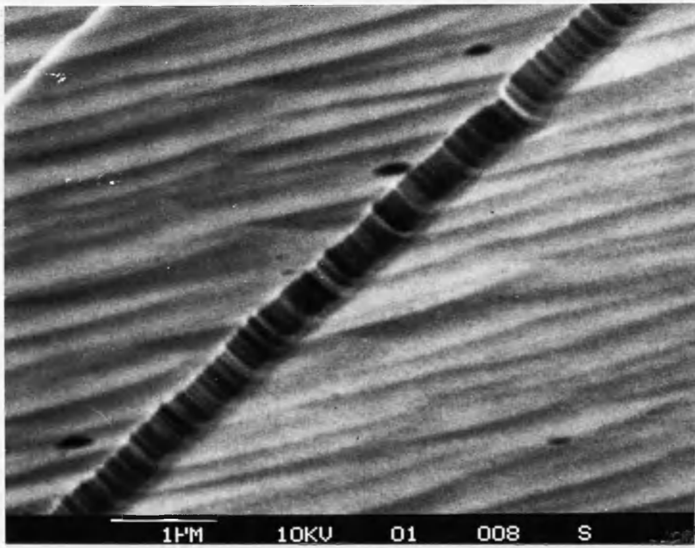

Fig.4.7b

SEM micrographs of a wet-chemically etched 3μm wide waveguide with a 0.3μm ridge height showing (a) the wall profile and (b) the wall roughness.

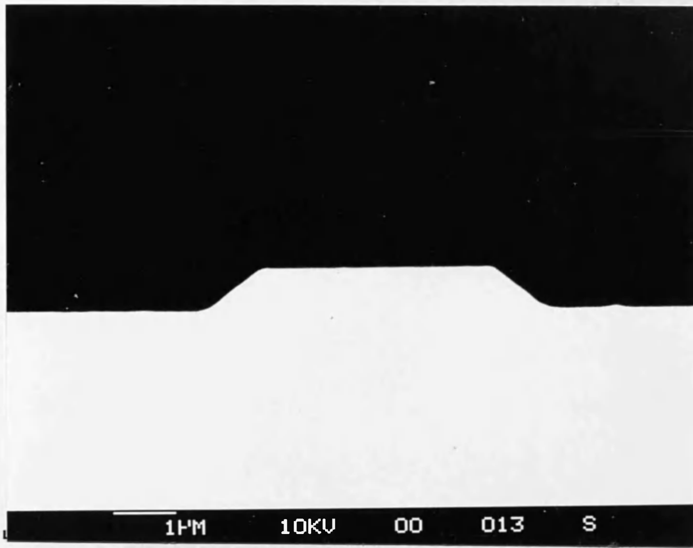

Fig.4.8a

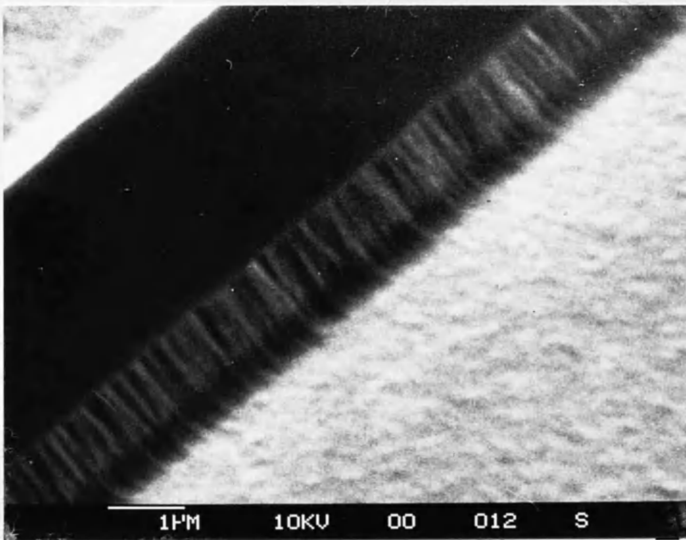

Fig.4.8b

SEM micrographs of a wet–chemically etched 6μm wide waveguide with a 0.6μm ridge height showing (a) the wall profile and (b) the wall roughness.

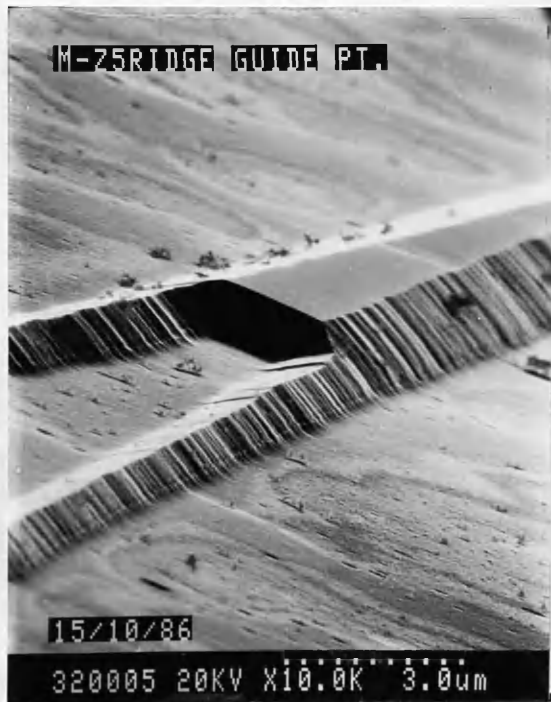

Fig.4.9

Undercut in Straight and Y– Junction waveguides etched using acidic hydrogen peroxide

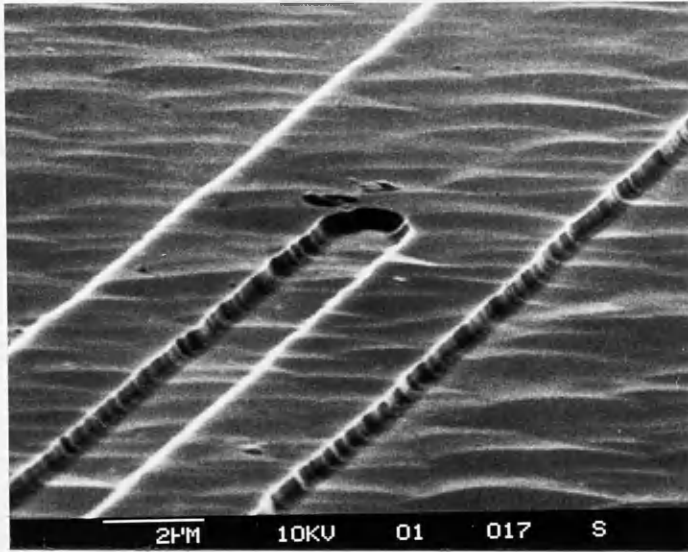

Fig.4.10a

SEM micrographs of a Reactive Ion Etched Y–junction formed by $3\mu m$ wide waveguides etched to a depth of $0.3\mu m$.

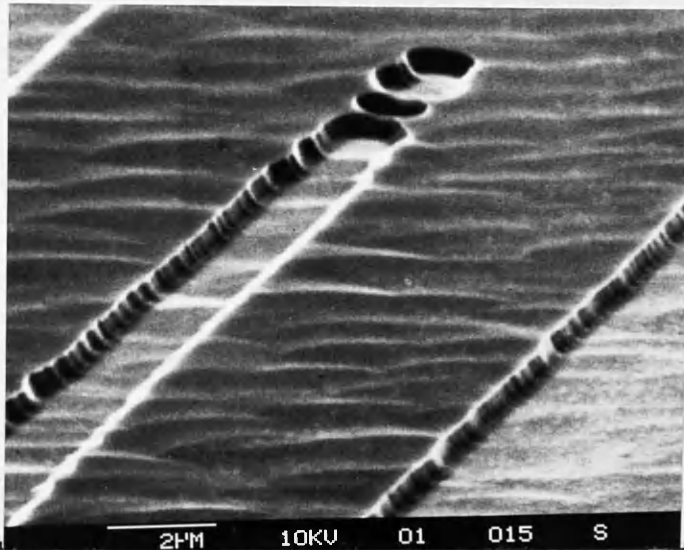

Fig.4.10b

SEM micrographs of a Reactive Ion Etched Y–junction formed by $6\mu m$ wide waveguides etched to a depth of $0.3\mu m$.

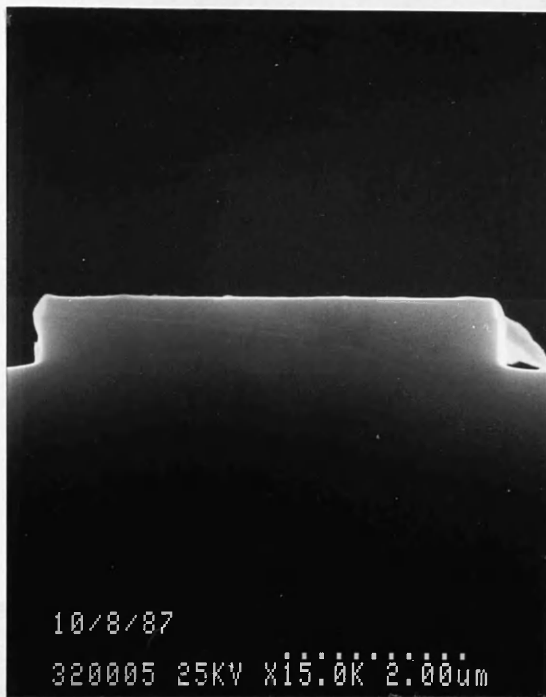

Fig.4.11a

Fig.4.11b

SEM micrographs of a Reactive Ion Etched 5μm wide waveguide with a 0.6μm ridge height showing (a) the wall profile and (b) the wall roughness.

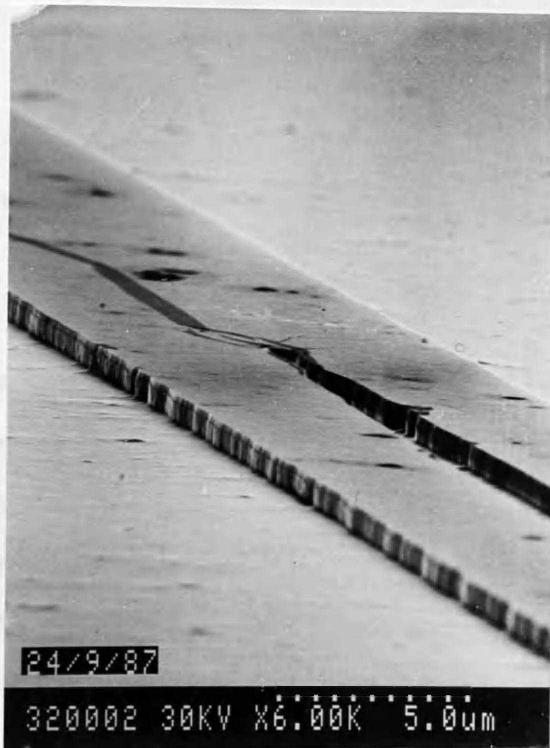

Fig.4.12
SEM micrographs of a Reactive Ion Etched Y– junction formed by $5\mu m$ wide waveguides etched to a depth of $0.6\mu m$.

etched to a depth of 0.6μm. A direct comparison with Fig.10 does not reveal any significant difference between Reactive Ion Etched and wet-chemically etched waveguides. But it must be borne in mind that attempting to etch 0.6μm chemically results in over a micron reduction in the width of the waveguides and, in addition, the profiles of the S-bend waveguides is not constant along their length, Sec.4.4.1.

4.5 Membrane Fabrication

The masks were produced by electron beam lithography and consisted of transparent windows in SMC chrome. This particular type of chrome is transparent to visible light but opaque to the ultra-violet radiation used in photolithography. Thus it is possible to see the wafer during alignment. A variety of rectangular windows were used, with the smallest dimension being 300μm and the largest 8mm depending on sensitivity requirements. The alignment procedure was fairly critical at some stages and is described in the next Sec.4.6.

Fig.4.1 indicates the necessity to etch through as much as 400μm upto the etch stop. The technique was fairly similar to that adopted by S. Mackie et al[17] and involved using a fast non-selective etch[16] to remove most of the substrate to within 20μm of the top surface. A slow selective etch[18] was then employed to approach the etch stop boundary and to effectively stop there. The photolithographic process is described in Appendix D and in Fig.4.13.

Results:

There is an upper limit on the time that the wafer can be left in the selective etch. As mentioned in Sec.4.2, photoresist is attacked by

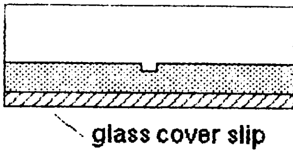

1.Spin resist onto wafer top, spin resist onto glass cover slip and place resist surfaces in contact.

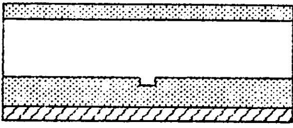

2.Spin resist onto wafer base.

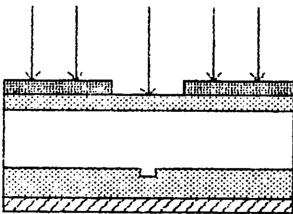

3.Mask and expose to ultra – violet radiation.

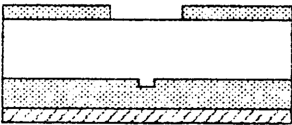

4.Develope resist using standard developer.

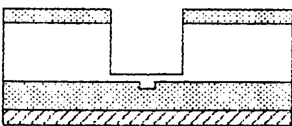

5.Carry out a two – stage wet chemical etch to remove most of the substrate.

6.Rinse with acetone and isopropyl alcohol to remove the remaining resist.

Fig.4.13

Photolithographic and Etching Processes for Membrane Fabrication

alkaline solutions and there is certainly evidence of this for etching times much longer than 10 mins. Bubbles are seen to form in the resist which then begins to peel and lift. This problem can be dealt with by evaporating a 0.01 μm layer of gold, as a mask, directly onto the wafer base before etching. The gold does not affect the operation of the pressure sensing device and so need not be removed at the end of the process.

The blue colour of the AlGaAs layer, with a high concentration of aluminium, is due to the band gap of the material. The band edge of GaAs lies at about 870nm and thus at shorter wavelengths it is highly absorbing. GaAs is transparent to infra-red radiation but highly reflecting to the visible spectrum. The band edge of AlAs, however, is at around 570nm, which is well into the red end of the visible spectrum. Thus, AlAs is transparent to red light and the infra-red spectrum while highly reflecting to the blue end. Therefore, the surface of a high Al concentration AlGaAs layer appears bluish.

The graphs of Fig.4.14 were obtained from a large number of samples and show the etch depth in GaAs versus time for the fast non-selective and the slow selective etches described above. The average etching rates are 10μm/min in Fig.4.14a and 3μm/min in Fig.4.14b. Both graphs appear to be fairly linear over the ranges shown but there are two points to note:

(a) The initial gradient of Fig.4.14a is greater than that for longer periods of etch. This is due to the elevated temperature of the non-selective etching solution when it is first made up (which can be as high as 40°C). The increase in temperature is the result of an

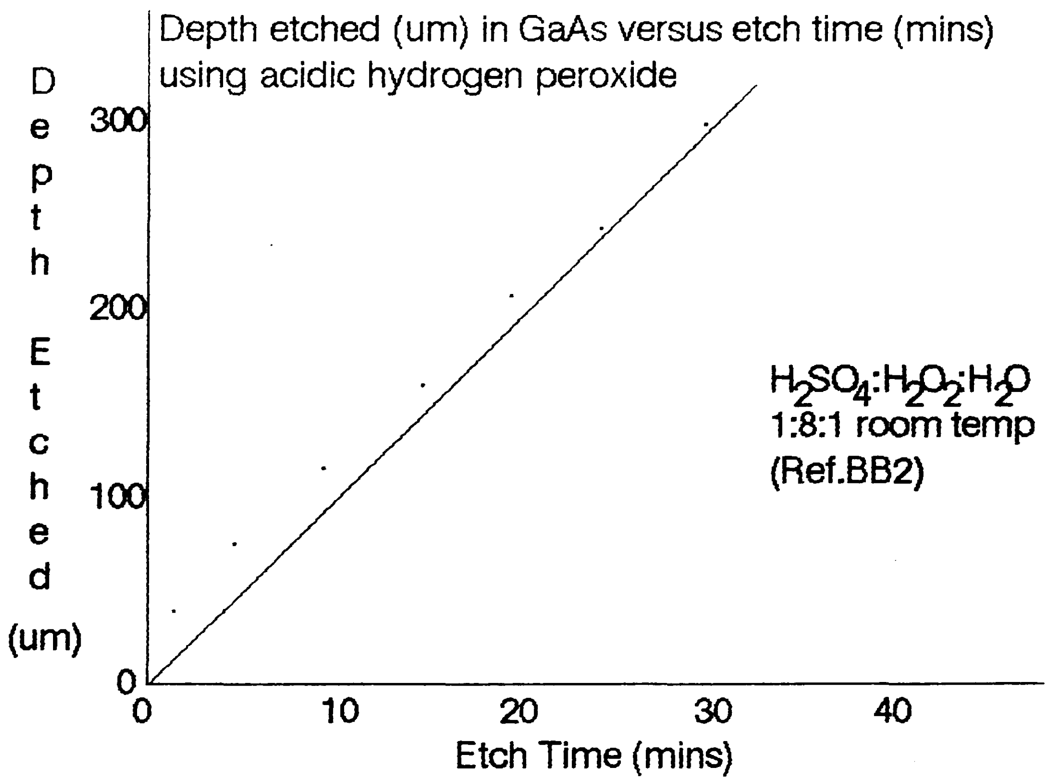

Fig.4.14a

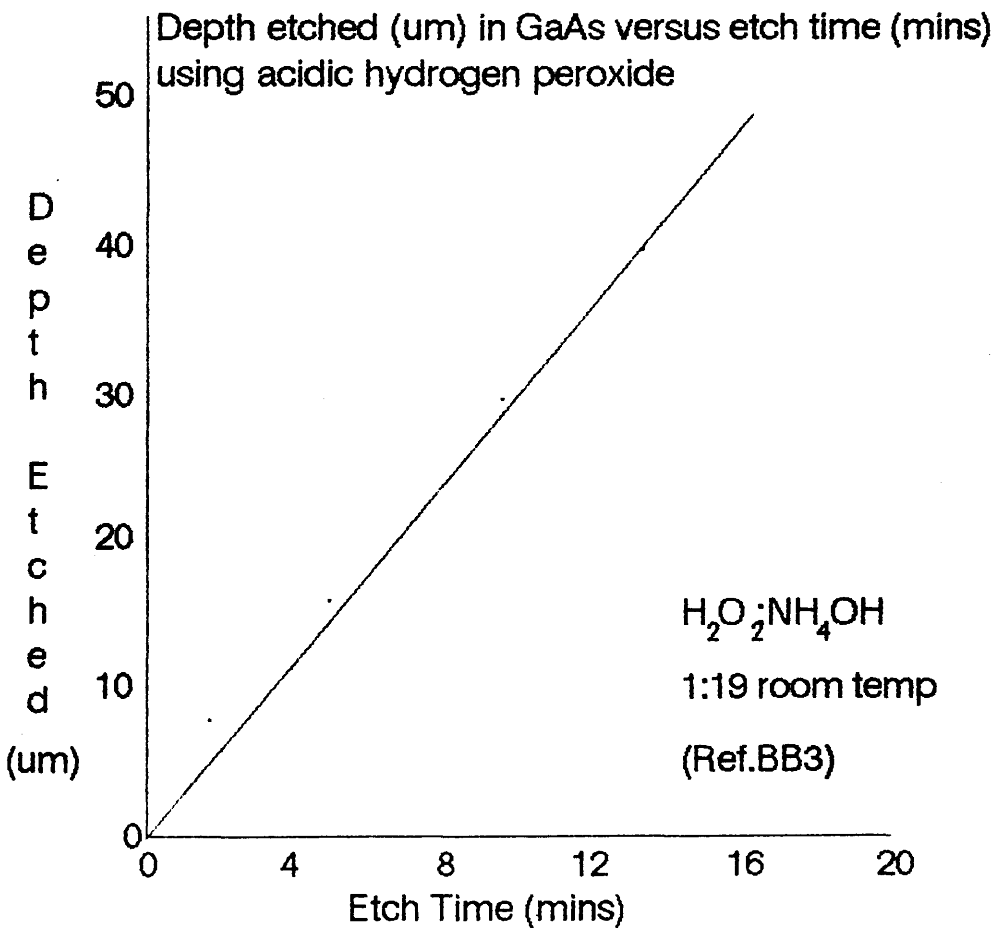

Fig.4.14b

exothermic reaction.

(b) Although there is no evidence on these particular graphs, longer etching times produce sub-linear values[15] due to the dissociation of H_2O_2.

Fig.4.15a shows the surface quality of a shallow etched surface (40μm deep) and Fig.15b a deep etched surface (300μm deep) in GaAs using the non-selective etch. Fig.4.15b indicates that the surface incongruities are reduced by prolonged etching, although the crystal plane preferences are still apparent, magnified in Fig.4.15c.

An example of an etch stop surface is shown in Fig.4.16 where the elliptical nature of the membrane base boundary is evident. In particular, the boundary formation stages can just be seen. The surface of the etch stop shows no indication of preferential etching because it has not been etched appreciably within the time limits used during the fabrication process.

In Fig.4.17a, the cleavage planes are highlighted by a broken membrane and show that, although shattered by a uniform surface pressure (provided by an air gun), the $<01\bar{1}>$ and $<011>$ planes are still apparent. Fig.4.17b-c were achieved by carefully cleaving a wafer directly through the membrane along the $<01\bar{1}>$ and $<011>$ directions respectively. Again the profiles indicated in Sec.4.3.5 and Fig.4.5 are clearly shown.

The thinnest point of a cleaved membrane is shown in Fig.4.18a. The wafer top surface is at the top of the photograph and the bright band shown towards the base of the photo is an $Al_{0.4}Ga_{0.6}As$ etch

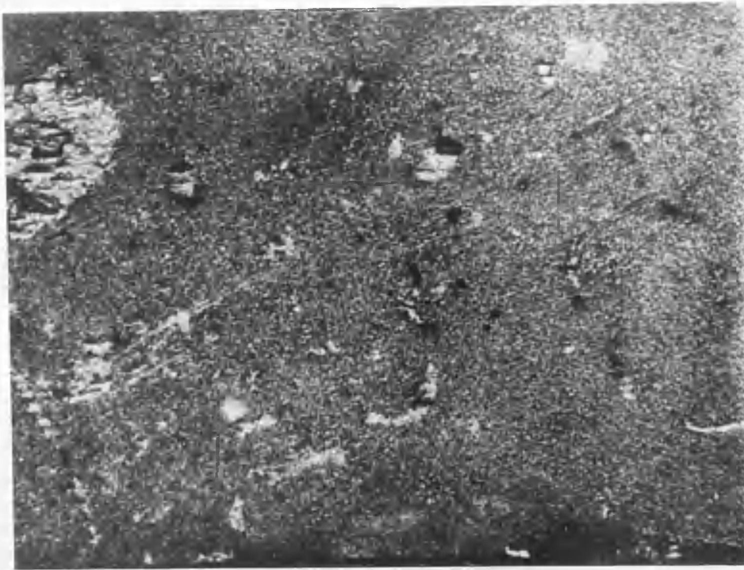

Fig.4.15a

Surface of a GaAs well wet–chemically etched to a depth of 40μm using acidic hydrogen peroxide.

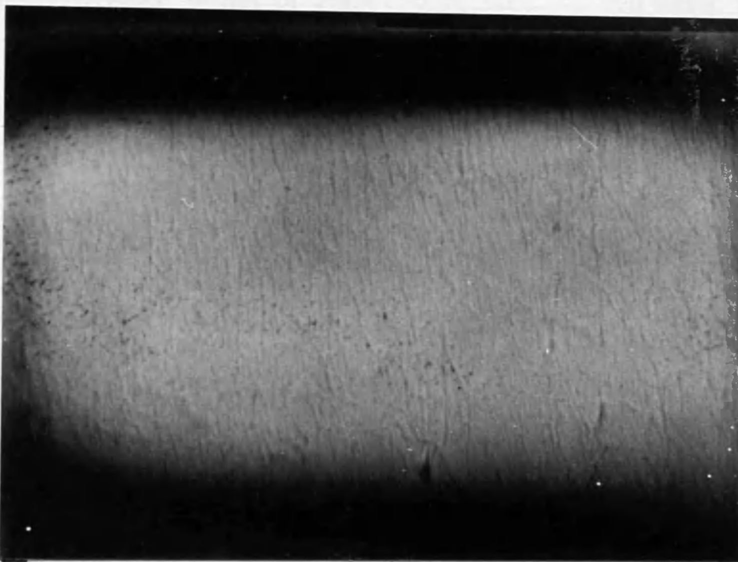

Fig.4.15b

Surface of a GaAs well wet–chemically etched to a depth of 300μm using acidic hydrogen peroxide.

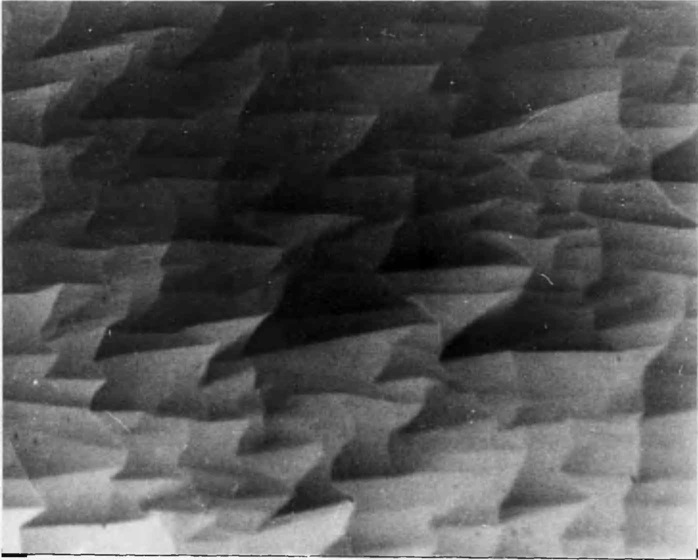

Fig.4.15c

Crystallographic planes of Fig.4.15b revealed by increasing the magnification by x200.

Fig.4.16

Surface of an $Al_{0.6}Ga_{0.4}As$ etch stop layer after using the selective etch alkaline hydrogen peroxide.

Fig.17a

A broken membrane revealing the $\langle 01\bar{1} \rangle$ and $\langle 011 \rangle$ planes.

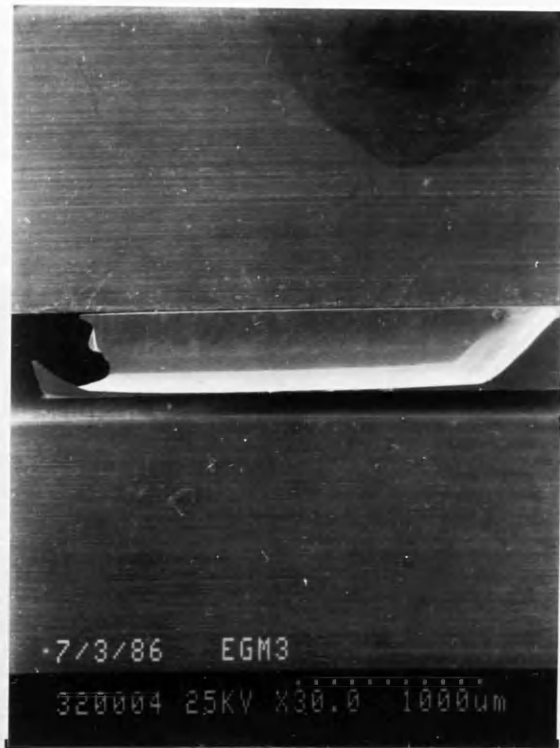

Fig.4.17b

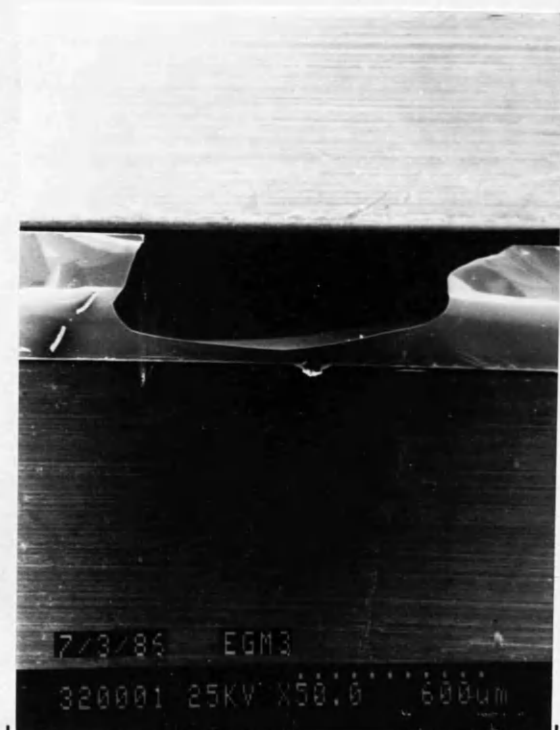

Fig.4.17c

The (a) $\langle 01\bar{1} \rangle$ and (b) $\langle 011 \rangle$ cross–sections of a cleaved membrane fabricated by wet–chemically etching a GaAs wafer.

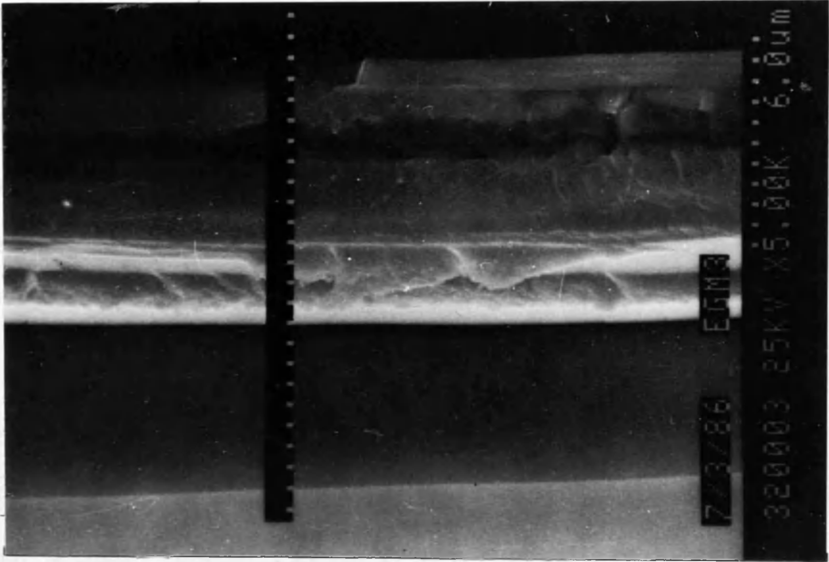

Fig.4.18a

A cleaved membrane where the membrane base is formed by the $Al_{0.6}Ga_{0.4}As$ etch stop (bright band). The wafer top surface is at the top of the photograph

stop layer (areas below this layer are outside the plane of the membrane cross section). This membrane is approximately 6–7μm thick at its thinnest point but, due to the scale of the membrane boundaries, the profile from one edge to the other had to be obtained by measuring the membrane at various points using an SEM. Fig.4.18b shows the results which indicate that this particular membrane has a gradual thickness taper, probably due to its early removal from the selective etchant. The membrane would not be completely flat over its entire surface unless the selective etch were left for extended periods of time.

4.6 Waveguide/Membrane Alignment

For very small membranes or complicated structures involving Mach–Zehnder interferometers, a mask aligner almost certainly has to be used. A special mask pair was designed with carefully constructed markers allowing a reference point (the corner of a wafer which can be located from both sides) to assist in the alignment.

The alignment technique is described in the simplified diagram of Fig.4.19. The waveguides were always fabricated first in order to prevent possible membrane collapse during fabrication. The alignment markers were lined up, as shown in Fig.4.16a, with one corner of the wafer formed by two intersecting cleaved edges. The waveguides were then fabricated as described in Sec.4.4. Fig.4.16b shows the alignment of the membrane on the base of the wafer. The necessity for using SMC chrome is evident when one realises that if the chrome is totally opaque to the visible spectrum, then only the wafer directly below a window is visible and alignment becomes impossible.

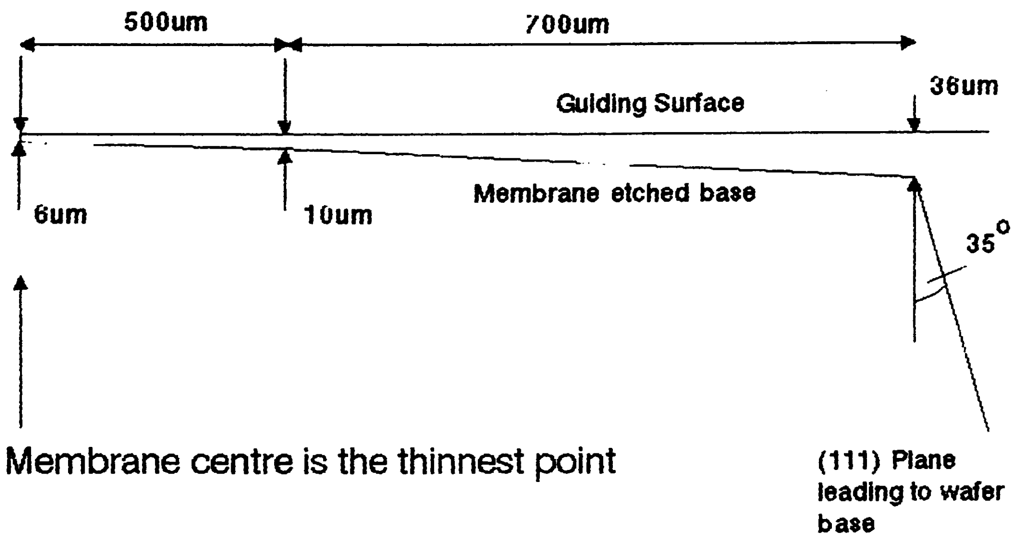

Fig.4.18b

A schematic of a typical membrane cross – section showing a gradual taper to mask edge. The length from membrane centre to edge is taken as 1.2um.

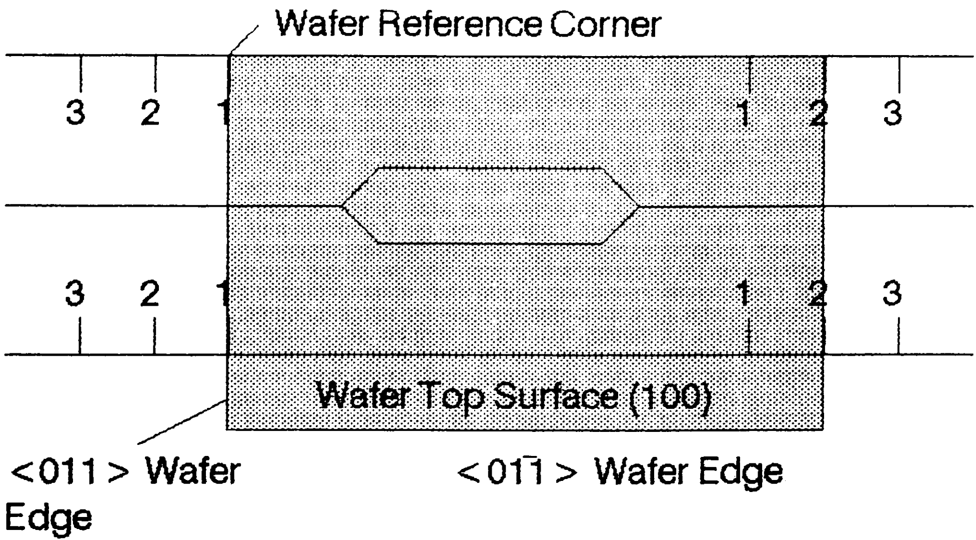

(a)

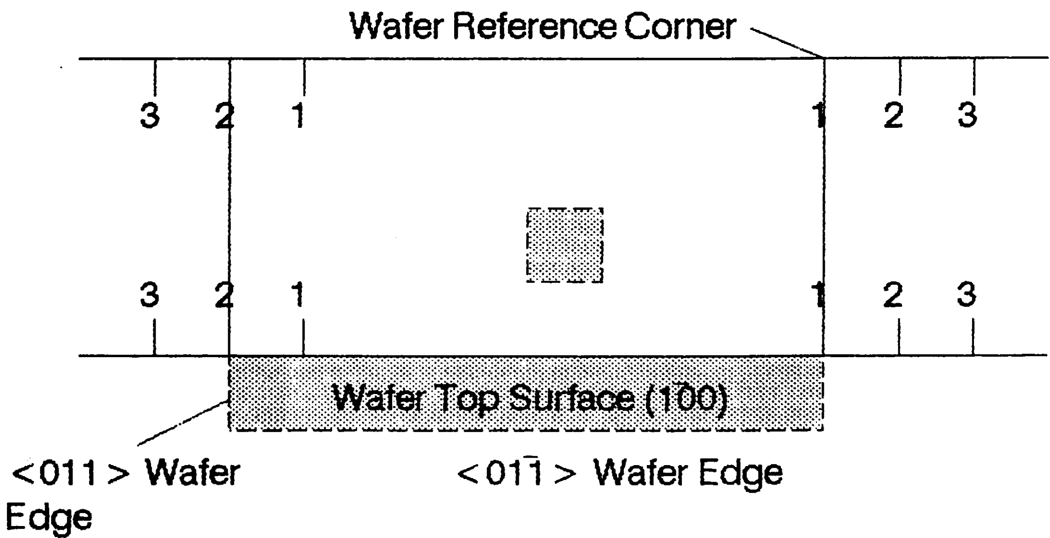

(b)

Fig.4.19

Membrane Window Alignment to Ridge Waveguides

This alignment process can be made easier by using an infra-red mask aligner which allows features on both sides of a GaAs wafer to be seen simultaneously i.e the waveguides on the top surface are visible at the same time as the membrane window mask. This facility removes the need for using the corner of a wafer as a reference and makes alignment simpler.

4.8 Summary

This chapter has described, in detail, the technology for the fabrication of a pressure sensor device in the GaAs/AlGaAs system. This technology could readily be adapted to other III-V semiconductors once a suitable etching system had been chosen. Waveguides fabricated by both wet-chemical etching and dry etching were described and compared. In general dry etched waveguides have vertical walls regardless of orientation while those produced by by wet-chemical etching led to ridge waveguide profiles which were dependent on the alignment of the waveguides relative to the <011> and <01$\bar{1}$> crystal directions. Membrane fabrication was carried out by selective wet-chemical etching using acidic hydrogen peroxide (10μmmin etch rate) to remove most of the substrate followed by alkaline hydrogen peroxide (3μm/min etch rate) to selectively stop at the $Al_{0.4}Ga_{0.6}As$ layer called the etch stop.

Scanning Elecron Micrographs indicate that the membrane base is not completely flat and is dependent on he length of time that the selctive etchant is allowed to clear the etch stop. Removing the wafer from the etch early, produces a membrane whose effective thickness is greater than that defined by the epitaxial layer etch stop.

Appendix A

Tricleaning:

1. *Boil in a beaker of trichloroethylene for five minutes to remove any heavy waxes that might be present.*
2. *Place wafer in a pre—heated beaker of acetone (in which trichloroethylene is soluble) and boil for five minutes.*
3. *Finally place in a pre—heated beaker of iso—propyl alcohol (in which acetone is soluble) for five minutes.*

When removed from the final beaker the temperature of the wafer will assist in rapid drying although it is better to use an air—gun to speed up the drying process.

Appendix B

Photolithography: Determination of Material Orientation (Fig. 4.5a):

1. *Positive photoresist, AZ1450J, is spun onto a GaAs wafer at 5000 rpm for 30 seconds providing a 2μm thick layer. The wafer is then baked for 40 minutes at about 85°C.*
2. *The mask consists of a wide chrome line on glass which does not allow ultra—violet radiation to reach one half of the wafer. On one wafer the longest edge is parallel to the <011> wafer edge and on the other it is parallel to the <01T> wafer edge. A mask aligner can be used but the eye is sufficient.*
3. *Standard developer dissolves the resist that has been exposed to the u.v radiation.*
4. *The wafers are placed in a freshly made up solution of:*

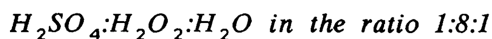

$H_2SO_4:H_2O_2:H_2O$ *in the ratio 1:8:1*

at room temperature for five minutes (in this case, no stirring is necessary) giving an etch depth of about 50µm. De–ionised water is used to quench the reaction. This depth is sufficient for preferential planes to be observable on a relatively low magnification microscope.

5. *Finally, acetone removes the remaining resist and isopropyl alcohol is used to remove the acetone and make air drying easier. (Acetone evaporates far more quickly than isopropyl alcohol, resulting in solvent stains).*

Appendix C

Photolithography: Waveguide Fabrication:

1. *Positive photoresist, AZ1450J for good line resolution, is spun onto a GaAs wafer at 5000 rpm for 30 seconds providing a 2µm thick layer. The wafer is then baked for 40 minutes at about 85°C.*
2. *A mask aligner is used to align the straight guides and the straight sections of the Mach–Zehnder structures along the $\langle 01\bar{1} \rangle$ direction. The wafers are then exposed to ultra–violet radiation.*
3. *Standard developer dissolves the resist that has been exposed to the u.v radiation.*
4. *Ridge heights $\leqslant$ 1µm are required. Too fast an etch might lead to over etching or cause the wafer immersion speed to become an important factor. The wafers are placed in a freshly made up solution of:*

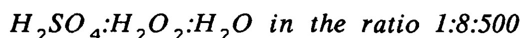

H_2SO_4:H_2O_2:H_2O *in the ratio 1:8:500*

at room temperature, with no stirring, leading to an etch rate

of about $0.065\mu m/min$. De–ionised water (DI water) is used to quench the reaction.

5. Finally acetone removes the remaining resist and isopropyl alcohol is used to remove the acetone making air–drying easier.

Appendix D

Photolithography: Membrane Fabrication:

1. *Positive photoresist, AZ1375, a relatively thick resist, is spun onto a GaAs wafer at 1000 rpm for 10 seconds providing a layer $\geqslant 5\mu m$ thick, thus protecting the top guiding surface. One side of a microscope cover slip is also coated in the same way. The two resist surfaces are placed in contact giving the top surface of the wafer added protection. The wafer is then baked for 60 minutes at about 85°C.*
2. *The wafer base is the only exposed area and it too is given a coating of AZ1375 at 5000 rpm for 30 seconds and baked for 40 minutes.*
3. *A mask aligner is used to align the rectangular edges of the windows along the $\langle 01\bar{1} \rangle$ and $\langle 011 \rangle$ wafer edges by looking through the SMC chrome. The wafers are then exposed to ultra violet radiation.*
4. *Standard developer is used to dissolve the resist that has been exposed to the u.v radiation.*
5. *For the fast non–selective etch[14] the wafers are placed in a freshly made up solution of:*

$H_2SO_4:H_2O_2:H_2O$ *in the ratio 1:8:1*

at room temperature with magnetic stirring leading to an etch rate of about $10\mu m/min$.

(a) The wafer is placed in the solution for 10 mins, rinsed in DI water and air–dried. An optical microscope is focussed onto the etched surface followed by the unetched surface and the vernier scale difference used to determine the etch depth more accurately (Sec. 4.3.3).

(b) The wafer is placed in a new solution of the etch in order to etch directly to within 50–100μm of the etch stop, based on the etch rate determined in (a). Another etch depth check should be made.

(c) Finally, based on the above calculations the wafer is etched to within 20μm of the etch stop.

(The above steps are followed to eliminate error in the etch depth which would be disastrous once in the vicinity of the etch stop. For a given section of a wafer, determining the etch procedure in two steps is adequate for all other sections of the same wafer).

For the slow non–selective etch[16] *the wafer is placed in a freshly made up solution of:*

$NH_3OH{:}H_2O_2$ *in the ratio 1:19*

at room temperature giving an etch rate of 3μm/min with no stirring. The wafer is left in the solution until the dark blue surface of the AlGaAs etch stop is seen, appearing as a gradually widening circle which becomes an ellipse if a rectangular boundary is present, and is normally removed at this stage. (If left longer the membrane base would become rectangular). DI water is used to quench the etching reaction.

6. *Finally acetone removes the remaining resist and isopropyl alcohol is then used to remove the acetone, making air–drying easier.*

References

[4.1] HOWES, M.J. and MORGAN, D.V. (Eds):'GaAs: Materials, Devices and Circuits'. Wiley series, 1985.

[4.2] TUCK, B., MILES, J.S.K., HARTWILL, A.J.:'Chemical Etching of (100) GaAs in the HNO_3:HF:H_2O System'. Journal of Materials Science, **11**, pp847–854, 1976.

[4.3] ADACHI, S., KANAGUCHI, H., IWANE, G.:'A New Etchant System, $K_2Cr_2O_7$:H_2SO_4:HCl for GaAs and InP'. Journal of Materials Science, **16**, pp2449–2456, 1981.

[4.4] STANO, A.:'Chemical Etching Characteristics of InGaAs/InP and InAlAs/InP Heterostructures'. Journal of the Electrochemical Society: Solid State Science and Technology, **134**, No.2, pp448–452, 1987.

[4.5] TIJBURG, R.P. and DONGEN, T. van:'Selective Etching of III–V Compounds with Redox Systems'. Journal of the Electrochemical Society: Solid State Science and Technology, **123**, No.5, pp687–691, 1976.

[4.6] KERN, W., DECKERT, C.A.:'Thin Film Processes:V–1, Chemical Etching'.

[4.7] IIDA, S., ITO, K.:'Selective Etching of GaAs Crystals in H_2SO_4:H_2O_2:H_2O System'. Journal of the Electrochemical Society: Solid State Science and Technology, **118**, No.5, pp768–771, 1971.

[4.8] SONEK, G.J., JIAN–ZHONG, L., WOLF, E.D. and BALLANTYNE, J.M.:'$SiCl_4$ Reactive Ion Etching for GaAs Optical Waveguides', Journal of Lightwave Technology, **LT–3**, No.5, pp1147–1150, 1985

[4.9] LI, J.Z., ADESIDA, I. and WOLF, E.D.:'Evidence of Crystallographic Etching in (100)GaAs using $SiCl_4$ Reactive Ion Etching', Journal of Vacuum Science and Technology B, **3**, No.1, pp406–409, 1985

[4.10] LI, J.Z., ADESIDA, I. and WOLF, E.D.:'Orientation Dependent Reactive Ion Etching of GaAs in $SiCl_4$', Applied Physics Letters **45**, No.8, pp897–899, 1984

[4.11] HIKOSAKA, K., MIMURA, T. and JOSHIN, K.:'', Japan Journal of Applied Physics, **20**, p847, 1981

[4.12] SEMURA, S. and SAITOH, H.:'',Journal of Vacuum Science and Technology A, **2**, p474, 1984

[4.13] LUDOWISE, M.J.:'Metalorganic Chemical Vapour Deposition of III–V Semiconductors', Journal of Applied Physics, **58**, No.8, ppR31–R409, 1985

[4.14] WOOD, C.E.C.:'Molecular Beam Epitaxy III–V Compounds:Dopant Incorporation, Characteristics and Behaviour', Proceedings of the Nato Advanced Studies Institute, Erice, Italy, 1983

[4.15] GANNON, J.J. and NEUSE, C.J.:'A Chemical Etchant for the Selective Removal of GaAs through SiO_2 masks'. Journal of the Electrochemical Society: Solid State Science and Technology, **121**, No.9, pp1215–1219, 1974.

[4.16] SHAW, D.W.:'Localised GaAs Etching with Acidic Hydrogen Peroxide Solutions'. Journal of the Electrochemical Society: Solid State Science and Technology, **128**, No.4, pp874–880, 1981.

[4.17] MACKIE, W.S., BEAUMONT, S.P., WILKINSON, C.W. and Roberts, J.S.:'High Resolution Lithography on Thin Active Semiconductor Membranes'. Proceedings 10th

Electron and Ion Beam Science and Technology Conference, Montreal, 1982.

[4.18] GRIFFITHS, R.J.M., BLENKINSOP, I.D. and WIGHT, D.R.:'Preparation and Properties of GaAs Layers for Novel FET Structures'. Electronics Letters, **15**, No.20, pp629–630.

CHAPTER FIVE

Experimental Results and Interpretations

5.1 Introduction

In this chapter some of the theoretical models discussed earlier are compared with experiment. All experiments involve some aspect of the proposed Mach– Zehnder pressure sensor and the understanding of each is essential to future characterisation and optimisation of devices which use some or all of the components.

5.2 Deflection– Pressure Tests

5.2.1 Objectives

In Sec.3.7, a relation between the central deflection of a membrane and uniform applied pressure, is derived. An experiment was designed to study this relation and plot the deflection– pressure curve for a membrane of known dimensions.

5.2.2 Experimental Procedure

The deflection was measured by using a microscope to observe the surface of a membrane through an optical flat (a glass plate flat to one– tenth of the light used) with monochromatic light. Focussing the microscope on the optical flat reveals Tolansky interference fringes between light reflected from the deflected membrane surface and that reflected by the optical flat, Fig.5.1a. The optical flat is coated with a thin layer of aluminium which allows 40% transmission for the wavelength of the mercury lamp used, 546.1nm. This transmission value provided good contrast between the dark and bright fringes i.e the surface of the GaAs wafer and the optical flat formed a Fabry– Perot cavity. A deflected membrane with an elliptical boudary

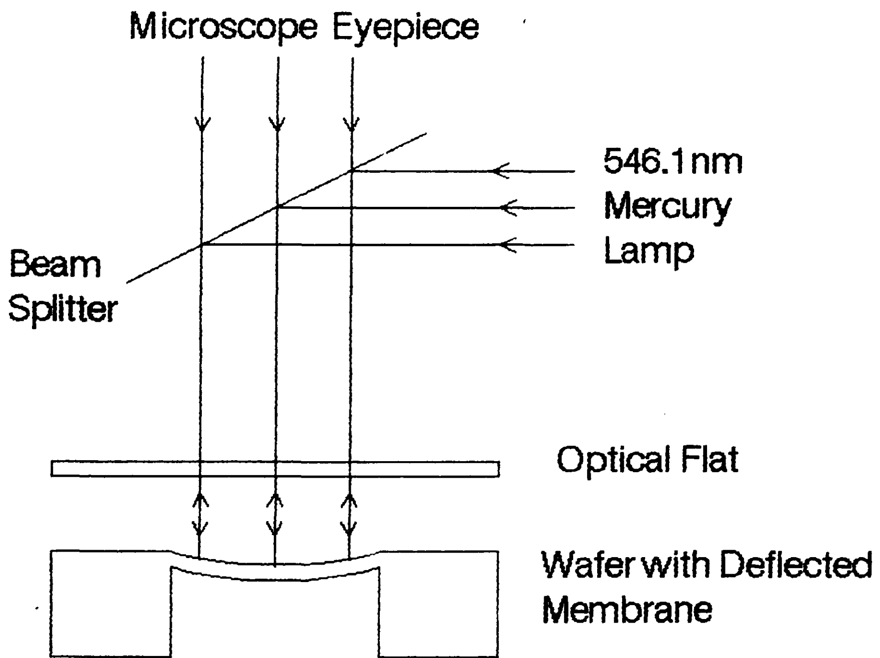

Fig.5.1a

Tolansky Microscope

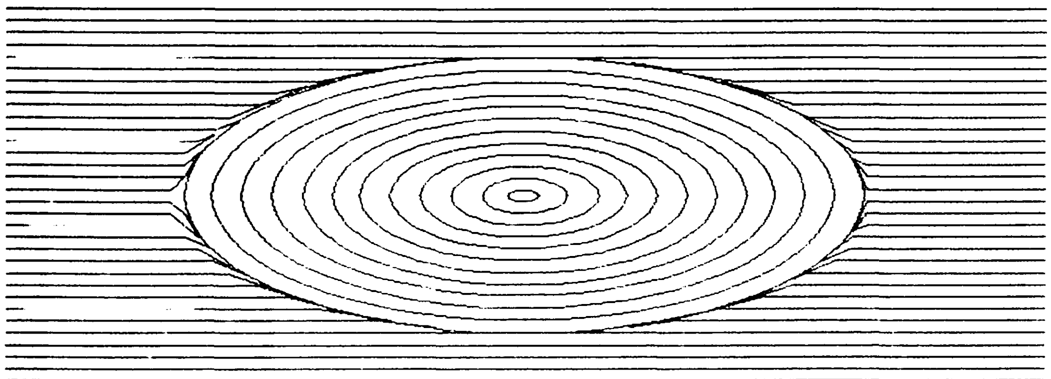

Fig.5.1b

Schematic of the Interference pattern observed in the Tolansky Microscope

produces a set of concentric ellipses, schematically represented in Fig.5.1b. An increase in the central deflection of the membrane results in the production of more rings apparently from the central region which shifts through light and dark fringes when the membrane centre moves by $\lambda/2$, where λ is the wavelength of the light used (546.1nm). By counting the fringes during pressure deformation one obtains the deflection–pressure curve. The microscope and vacuum set–up is shown in Fig.5.2. The wafer is vacuum sealed to the sample holder using a low temperature wax (e.g Paraplase, melting point ≃ 57°C). The vacuum is provided by a small solenoid diaphragm pump. When the control valve is fully open the pressure difference across the membrane is small, ≃1/40 psi, but when fully closed the system is evacuated to produce a theoretical maximum pressure difference of one atmosphere. A differential pressure gauge of maximum range 2psi is used to measure the pressure differences and, consequently, the pressure difference was restricted to this value. For this particular experiment, the epitaxial wafer in Fig.5.3 was used to produce membranes the thicknesses of which were controlled, by the etch stop, to 6.7μm:

Layer	Thickness	
GaAs	1.2μm	
$Al_{0.08}Ga_{0.92}As$	2.5μm	
$Al_{0.60}Ga_{0.40}As$	3.0μm	Etch Stop
GaAs Substrate		

Fig.5.3

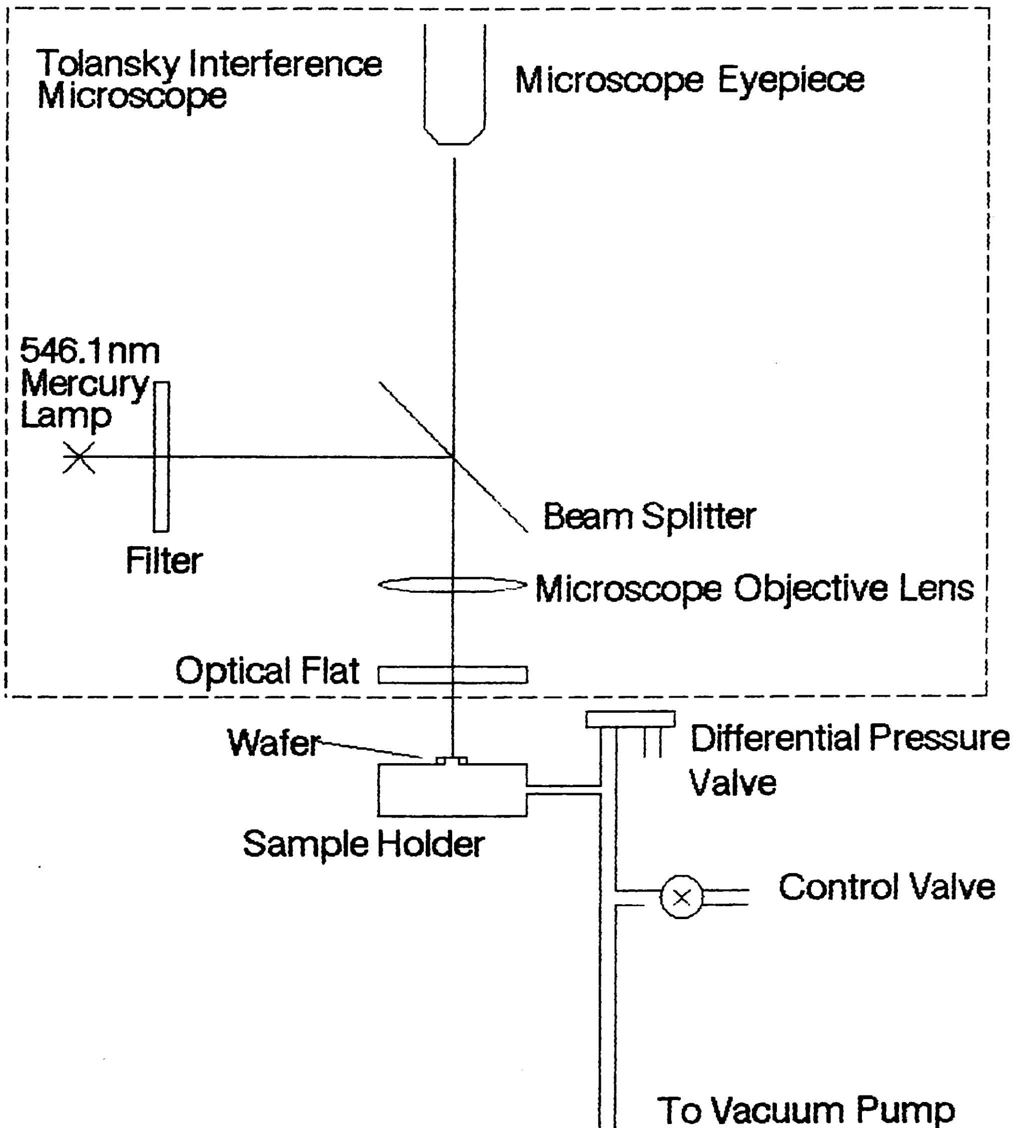

Fig.5.2

Microscope and vacuum system

5.2.2 Discussions of Results

The experimental data points in Fig.5.4 are for an elliptical membrane of dimensions 2mm x 1mm x 6.7μm. The line is the best fit provided by the theoretical model given in Chap.3, Eqn.3.55. There is good agreement between the experimental and theoretical results. The difference in the membrane thickness between the experimental curve obtained for the fabricated membrane and the theoretical prediction may lie in the fact that the membranes are not completely flat. Measurements of the taper in a fabricated membrane (via SEM micrographs) are given in Fig.4.18b. In this case, the membrane centre is 6.7μm thick but this gradually increases to 36μm at the membrane edge where the step wall profile gradient begins.

There is a permanent deflection to the membrane producing a central deflection of $\simeq$14μm calculated by counting the number of fringes seen across the membrane surface when no pressure is applied to the system. In general membranes etched to within 10μm of the etch stop showed no signs of sagging. But when the selective etch was used to clear the etch stop of the remaining 10μm of GaAs substrate, the permanent deflection became evident. It is believed that this deflection is due to stress relaxation at the etch stop interface when the GaAs substrate is removed. The lattice constant of $Al_xGa_{1-x}As$ is greater than that of pure GaAs [1] and during the growth process the initial layers of AlGaAs on the substrate undergo tensile stress in order to lattice match with the lower layers. When the substrate is selectively etched away, the layers expand once again and the lower surface curves, resulting in the whole membrane surface experiencing a permanent deflection.

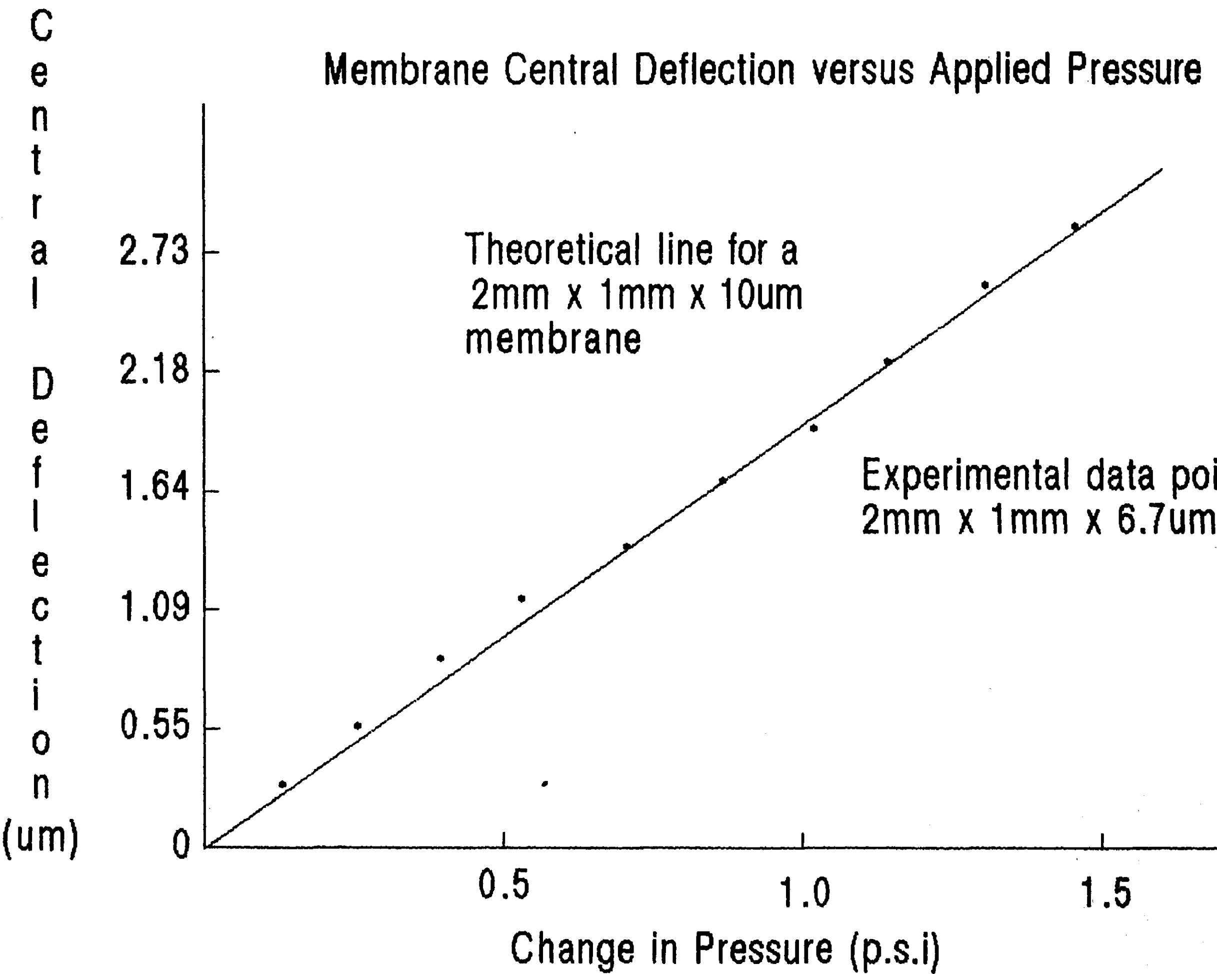

Fig.5.4

5.3 Straight Waveguide Observations

5.3.1 Objectives

During the design stages of the Mach–Zehnder pressure sensor, single–mode waveguide structures were required in order to minimise the number of complicating factors, for example mode conversion. In addition, single–mode guides in the compact Mach–Zehnder interferometer are essential for the device to function efficiently, Sec.2.7. Here, techniques are described for studying the single–mode behaviour of a guide and distinguishing such guides from multimode guides.

5.3.2 Experimental Procedure

To determine whether a guide is single–mode or multimode at a particular wavelength, one must scan light across the guide input in an attempt to excite all possible modes which are supported. For a single–mode guide, movement from central alignment of the laser light and guide input results in a decrease in light amplitude at the guide output but no change in the mode profile. Multimode guides do not show such simple behaviour. A guide which supports the fundamental and the lowest order asymmetric mode exhibits, given a centrally aligned input, a single lobe; but on moving the laser beam off–centre produces the two lobes characteristic of the lowest order asymmetric mode.

Two systems were used at various stages of the project – one which used white light sources that were provided by two horizontal microscope systems, Fig.5.5, was built at The University of Glasgow[3]. The microscopes were arranged not only to couple coherent infra–red light into and out of the guides, but also to allow the ridge

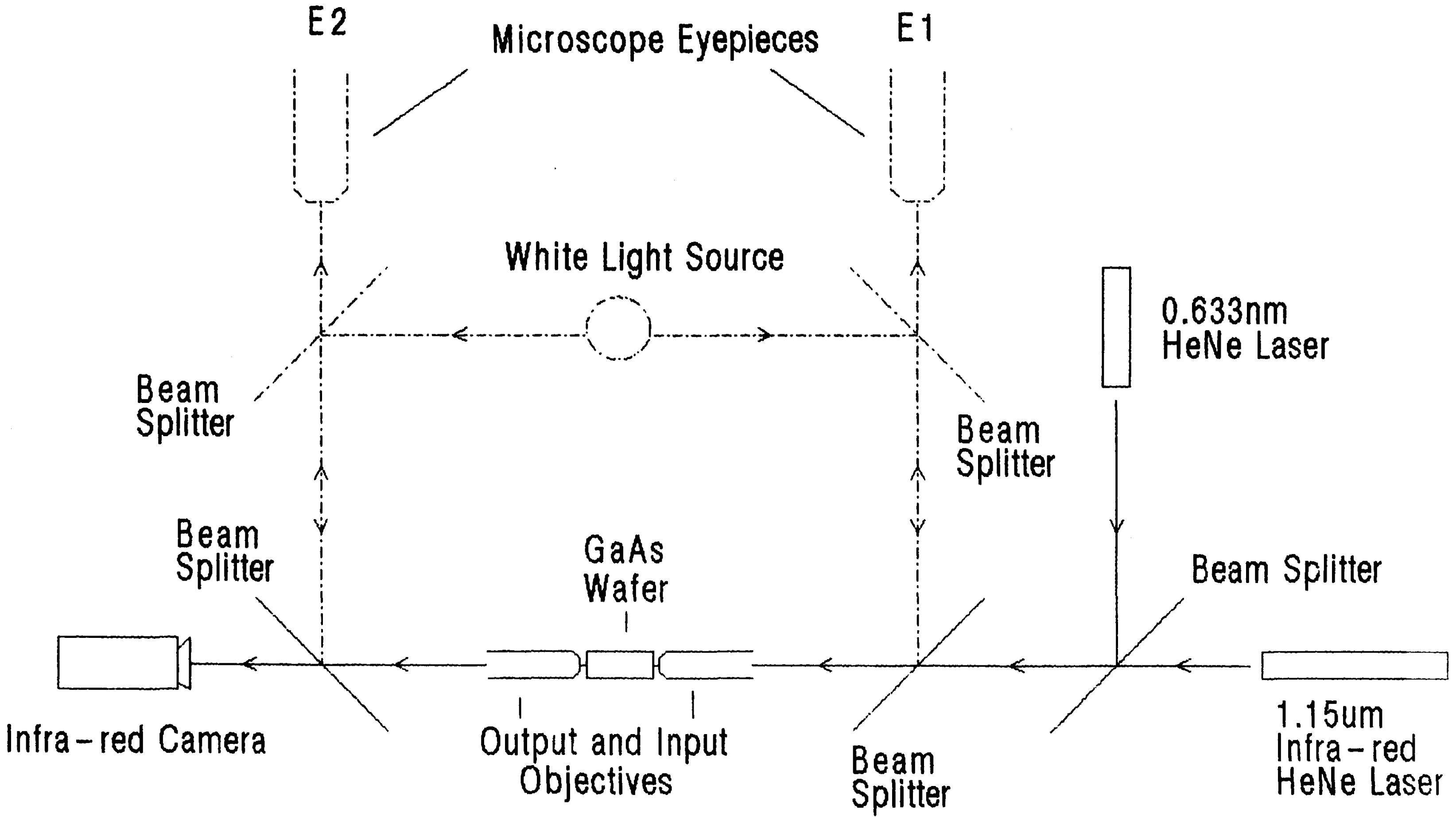

Fig.5.5

Waveguide End-fire Apparatus

waveguides to be seen by the observer at O1 and O2, via white light reflected from the cleaved edges. The second, more basic system, is identical to Fig.5.5 without white light sources to assist in alignment.

The dual microscope system was operated as follows; the infrared laser (1.15μm) was shuttered in order to protect the eyes of the observer and the visible HeNe laser (0.633μm) was passed through a filter to reduce its intensity since its reflection was seen in eye–piece, E1. The sample was orientated relative to the input and output objectives so that both the input and output of a ridge waveguide were seen in eyepieces E_2 and E_1 respectively. To assist in this effort an overhead, low magnification, viewer was used to ensure that the guide was aligned with the central regions of the microscope apertures. Once orientation was established the visible red laser, the path of which coincides with that of the infra–red laser, was then focussed onto the edge of the wafer and centred on a ridge waveguide. The visible red laser was then switched off and the output microscope objective re–focussed onto a camera thus producing the output of the ridge waveguide, since the camera is sensitive to a wide band of wavelengths. The white light source was then removed and the infra–red laser unshuttered to study guiding. Minor changes in the focus of the input objective is required to maximise the input coupling. This is due to the different focal points of the visible and infra–red lasers.

The second, simpler end–fire set–up, requires a great deal of familiarity with the various visible and infra–red light patterns which appear on the camera due to relative positions between the wafer edge and the input laser beams. With practice one can determine the

region in which waveguides exist and, using Lloyd's mirror interference[2] patterns, alignment can be achieved fairly quickly. The Lloyd's fringes are due to interference between light which undergoes glancing total internal reflection from the wafer surface and light direct from the lasers both of which are brought to focus on the camera.

5.3.3 Results

Guides produced by both Reactive Ion Etching and Wet Chemical Etching are studied, Fig.5.6:

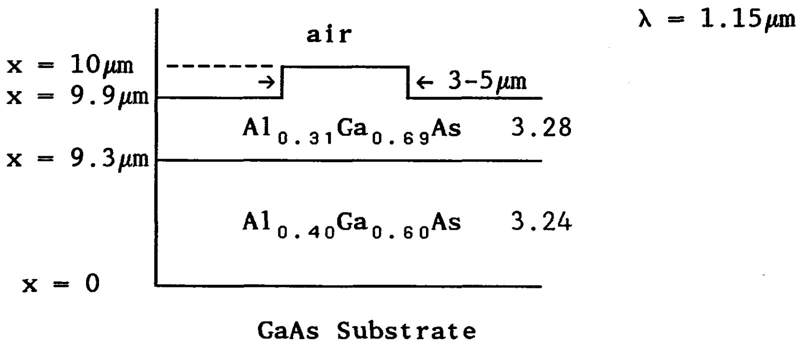

Fig.5.6a

Reactive Ion Etched Structure

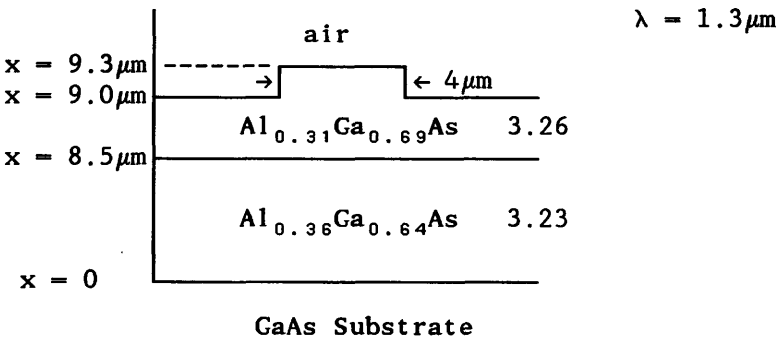

Fig.5.6b

Wet Chemical Etched Structure

Reactive Ion Etched Ridge Waveguide, Fig.5.6a

Ridge waveguides in the range from 3μm to 6μm widths were studied but the most interesting, were widths 4μm and 6μm, because it is between these two values that the ridge guides were observed to undergo a transition from a structure which supports a single-mode to one that supports two modes. Figs.5.7-8 show the results of scanning the laser beam across the guide inputs for both the 4μm and 6μm ridge waveguides. The single-mode 4μm wide guide, Fig.5.7, shows only one lobe, characteristic of the fundamental mode, throughout its scan although there appears to be slight asymmetry in Fig.5.7b where the input beam is displaced from the guide centre. The excitation of the first asymmetric mode can be seen in Fig.5.8. In Fig.5.8c the central region of the first asymmetric mode does not fall to zero. It is believed that some excitation of the fundamental mode persisted. 5μm wide guides which were also analysed showed behaviour indistinguishable from that for the 4μm wide ridge.

The results agree fairly well with those predicted by the effective index method. The effective index method indicates a switch from a structure which supports two modes to one which is single-mode occuring between 3μm and 4μm for the structure in Fig.5.6a. The lowest order asymmetric mode is, however, weakly guided, Sec.2.5.2. This work was carried out at 1.15μm which was available for the system shown in Fig.5.5.

Chemically Etched Ridge Waveguide, Fig.5.6b

This guide, etched using techniques described in Chap.4, was not as thoroughly tested as that in Fig.5.6a, but nevertheless the output of this guide at 1.3μm, Fig.5.9, shows that the structure supports a

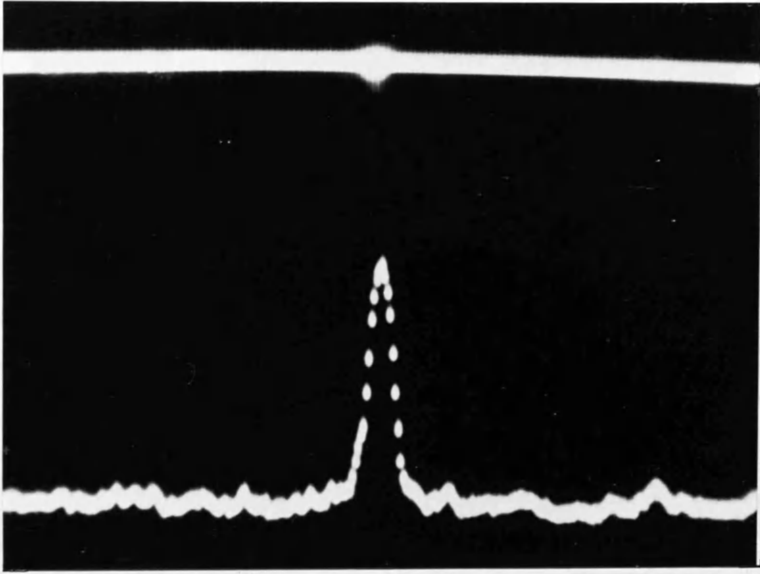

Fig.5.7a

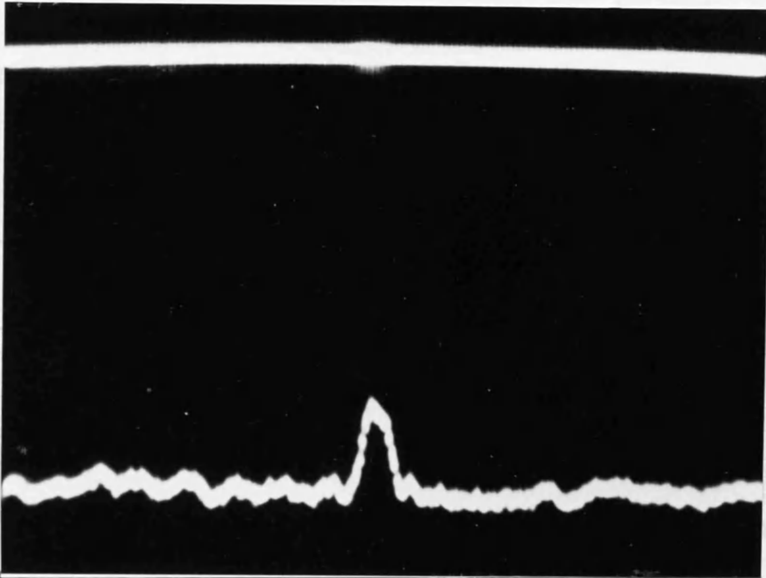

Fig.5.7b

The output of a $4\mu m$ wide single-mode waveguide where the input beam is (a) aligned centrally to the ridge and (b) offset with respect to the ridge.

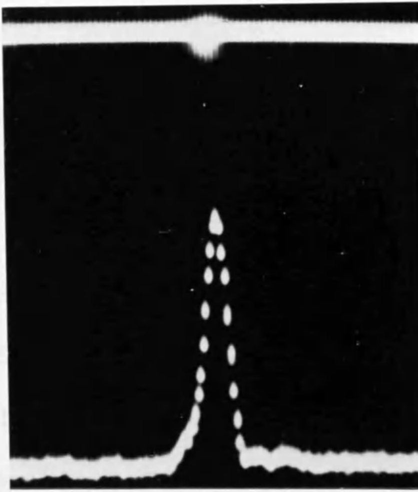

Fig.5.8a

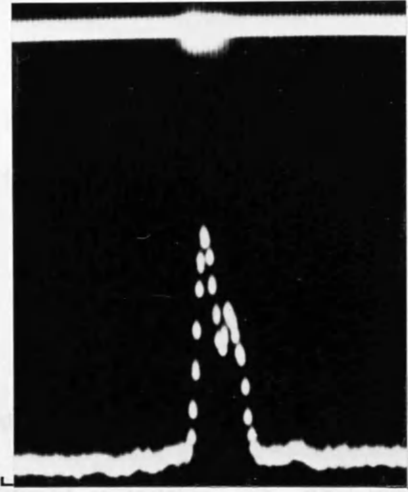

Fig.5.8b

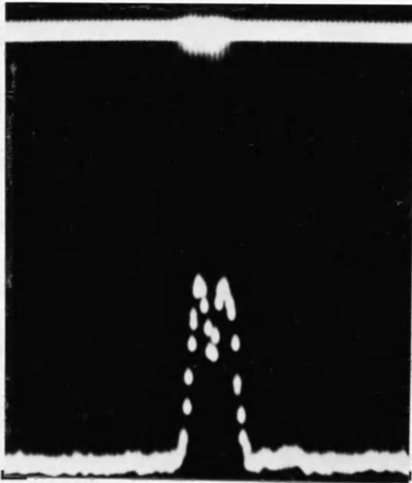

Fig.5.8c

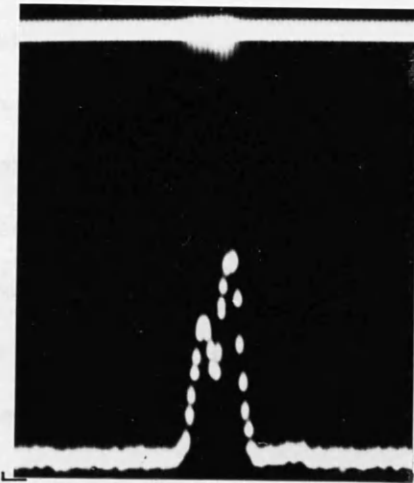

Fig.5.8d

The output of a multimode Reactive Ion Etched ridge waveguide as the input is scanned (in the wafer plane) using a 1.15μm infra-red HeNe laser.

fundamental mode. Calculations made using the effective index method reveal that the guide is single-mode but due to the small difference in aluminium concentration of the guiding layers, 5% ($\Delta n \approx 0.02$), the vertical slab confinement is weak. This factor is aggravated by sloping walls and the effects of undercut inherent in the fabrication process. These factors contribute to the lowering of the propagation constant of the guides by reducing their effective widths[3].

5.4 Y-Junction Analysis

5.4.1 Objectives

The Y-junctions studied in this section are parts of the Mach-Zehnder waveguide configuration proposed for the pressure sensor which were cleaved in half to produce two Y-junctions, Chap.2. There had initially been some difficulty in studying Mach-Zehnder structures produced by chemical etching, due to apparent slab guiding across the waveguide outputs when the inputs were excited. The outputs were expected to be similar to those of single-mode ridge waveguides or at worst to support no guiding at all. Studies are presented in this section for Reactive Ion Etched and Wet Chemically etched Y-junctions and observations made using both 1.15μm HeNe light and a 1.3μm semiconductor laser. Some idea of the losses compared to straight waveguides were also obtained by comparing, directly, the output intensities of straight waveguides and Y-junction waveguides on the same wafers.

The Y-junctions are formed using S-bends of 40mm radius to provide arms separations of 300μm and an overall length of about 7mm. More details of these Y-junctions are presented in Chap.2 with numerical analyses to describe their behaviour.

5.4.2 Experimental Procedure

The Y– junctions are placed in the apparatus shown in Fig.5.5 and the single input guide is excited by scanning light across it. The output guiding arms are observed simultaneously, using a relatively low magnification, and individually under high magnification. To estimate the loss in the Y– junction waveguides, the combined intensity of both the output arms were optimised using a germanium detector and oscilloscope. The wafer was then translated to straight waveguides of the same geometry and the output would again be optimised and recorded.

5.4.3 Results

Wet Chemically Etched Y–Junction

The apparent slab guiding of light seen in Fig.5.10, is due either to light radiating from the S– bends used to separate the arms of the structure or scattering at the Y– junctions. The former case is particularly likely in the case of wet chemical etching since the ridge waveguide profiles are orientation dependent and so change as the guide curves, Sec.4.5. The scan line lies at the mid– point of the two output arms. For this particular experiment no white light sources were available which meant that direct visual determination of ridge waveguide position was unattainable. This difficulty can be overcome by fabricating a mask with both Y– junctions and straight guides. Thus, investigating a straight guide reveals the position of the direct line between input and output and, since the Y– junctions are symmetric, the centre is obvious.

The slab mode seen in Fig.5.10 stretches from one output arm to the

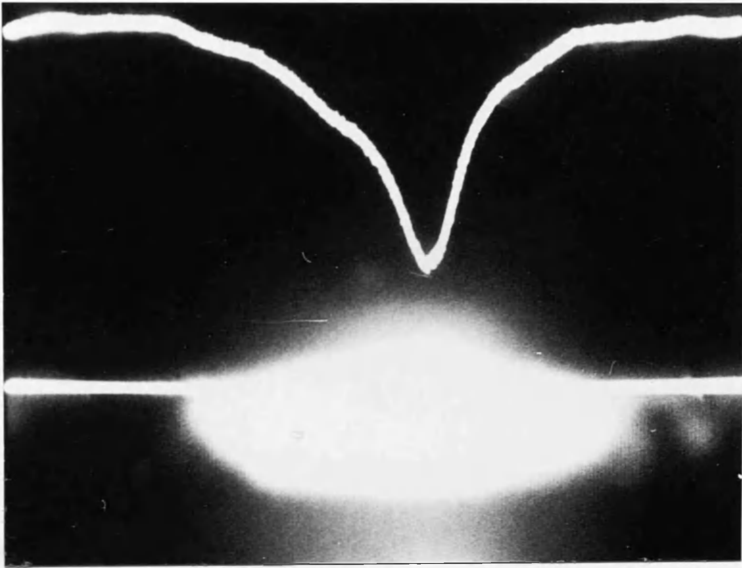

Fig.5.9

The output of a single mode wet–chemically etched 4μm wide ridge waveguide using a 1.3μm semiconductor laser.

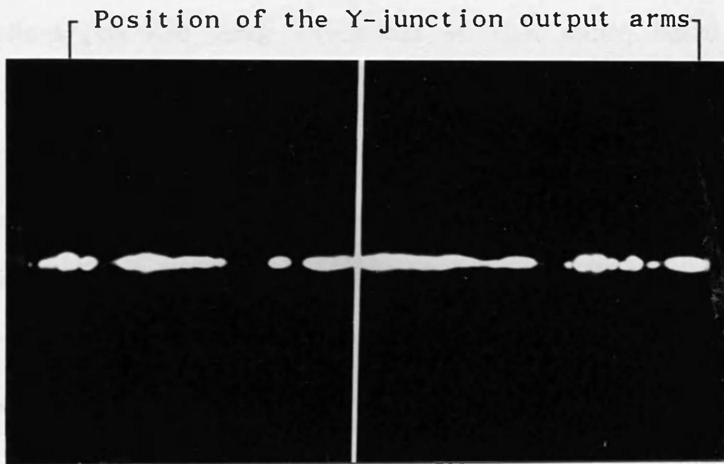

Fig.5.10

Scattering of light between the output arms of a wet–chemically etched waveguide Y–junction (at 1.3μm).

next, indicating that the light is certainly being radiated throughout the entire S–bends. Further attempts at waveguide fabrication using wet chemical etching failed to produce better results. At this stage it was decided that, although wet chemical etching is suitable for most straight waveguide applications, curves (and hence S–bends) would prove difficult presenting stringent design parameters. But the author believes that Y–junctions incorporating S–bends are possible and may even become easily reproducible once a succesful design has been established.

Reactive Ion Etched Y–Junctions

The Y–junction waveguides, based on the structure shown in Fig.5.6a, exhibited good confinement of 1.15μm light in the output arms. Single mode and multimode Y–junction waveguides behave very differently as the input coupling is altered by scanning across the input guide.

Y–junctions produced using waveguides of 3μm width, based on the structure of Fig.5.6a, were excited at the input using 1.15μm wavelength light. The output arms were observed simultaneously using a Hammamatsu camera and are shown in Fig.5.11. Slight scanning movements across the guide input produced a simultaneous and equal fall in amplitude of the light in the output arms, which would be expected for a single–mode structure. The asymmetry of Fig.5.11 is shown to indicate that the behaviour of the Y–junction is not completely single–mode. As stated above, the peaks have identical heights throughout most of the scan, Fig.5.11a, but on either side of the simultaneous maximum height, there is an apparent switch of some light from one output arm to the next. But at no time do the

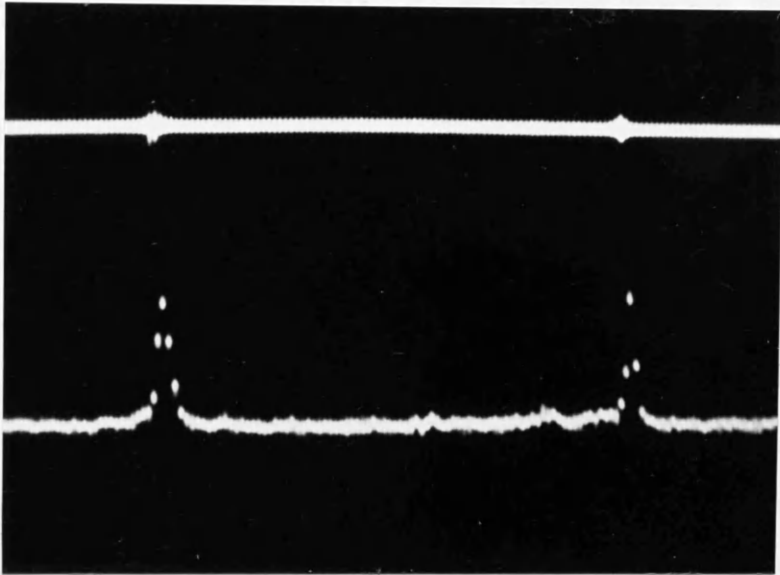

Fig.5.11a

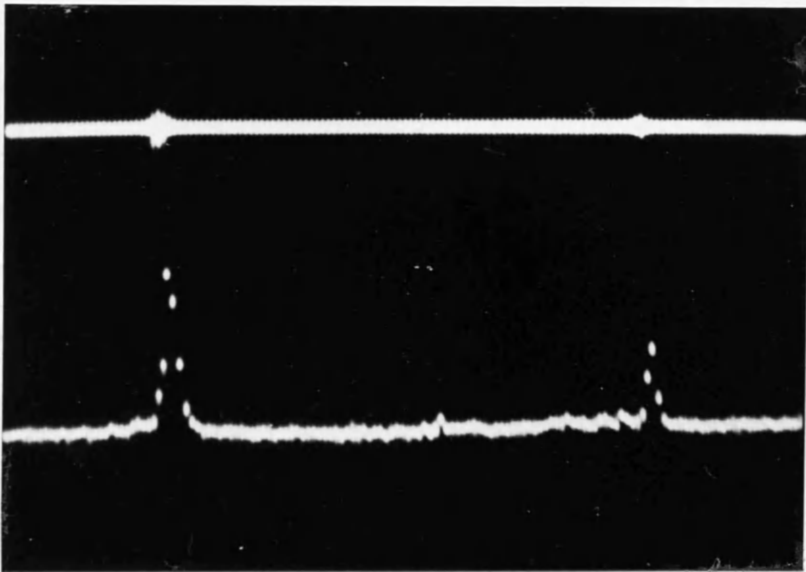

Fig.5.11b

The output of a single-mode Reactive Ion Etched waveguide Y-junction as the input is scanned (in the wafer plane) using a 1.15μm infra-red HeNe laser. A weakly guided asymmetric mode results in the slight asymmetry of Fig.11b.

relative heights of the peaks increase beyond that indicated in Fig.5.11b. The scanning movements were carried out in both the horizontal and vertical directions. In the vertical direction the peak intensity at each of the output guides increased and decreased with the same heights and the input was scanned. The difference between this behaviour and that of the 6μm multimode guides is quite striking.

The 6μm wide ridge waveguides forming the Y-junction outputs were also studied at 1.15μm. Scanning the laser beam horizontally (orientated to Fig.5.6a) across the guide input caused the light to move from one arm to the next. Some of the stages produced by scanning are captured in Fig.5.12. Before scanning begins, there is sufficient input off-set to produce zero output in both the arms. As the scan proceeds the output increases equally in both arms until the point shown in Fig.5.12a. Further scanning results in most of the light moving to one arm, Fig.5.12b. The two peaks then become equal once again, Fig.5.12c, (higher than the peaks in Fig.5.12a) before the light then appears in the other arm, Fig.5.12d. A close look at the peaks in both Figs.5.12b-d show hints of an asymmetric mode in the right hand output arm. This agrees with the behaviour of the 6μm wide straight waveguide of Sec.3.3. A vertical scan of the input guide results in the arms behaving identically and rising to a maximum when the laser beam is centralised relative to the ridge.

Loss measurements carried out for the dry-etched Y-junction waveguides indicated losses of 1dB relative to straight waveguides which had been fabricated on the same samples as the Y-junctions. However there was some difficulty in obtaining consistent results since it was found that, even between straight waveguides which were

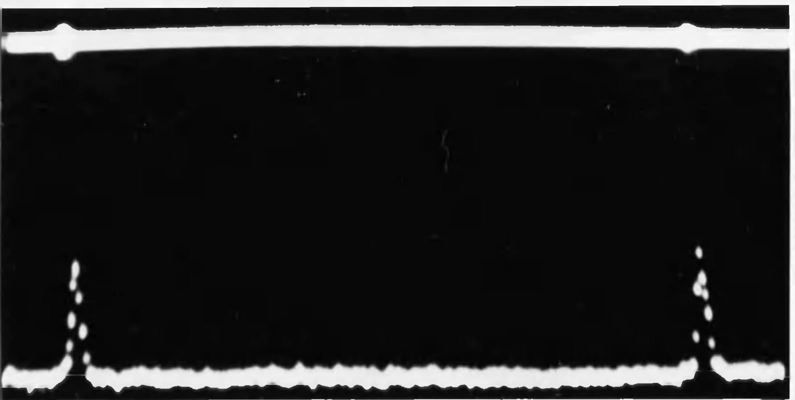

Fig.5.12a

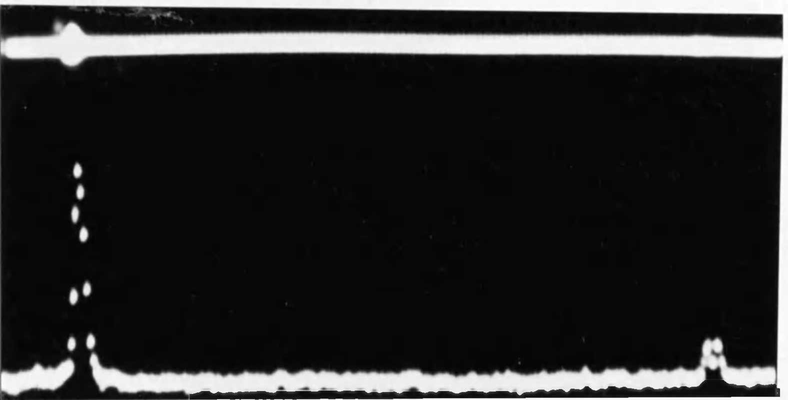

Fig.5.12b

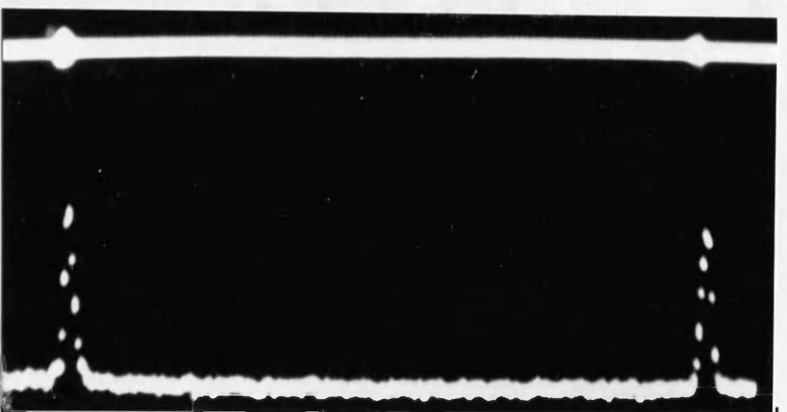

Fig.5.12c

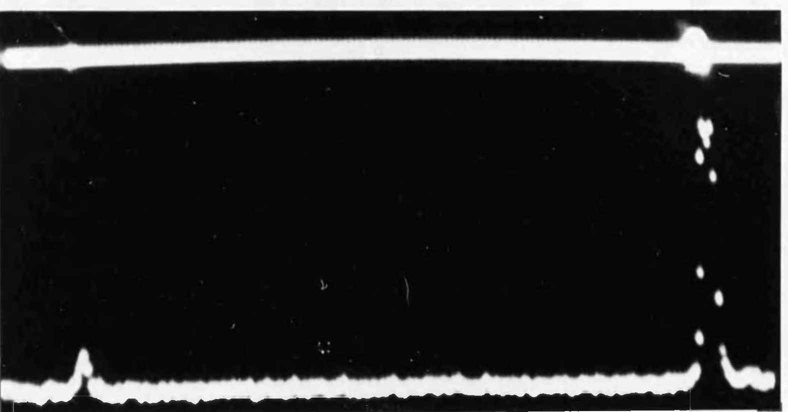

Fig.5.12d

The output of a multimode Reactive Ion Etched Y− junction waveguide as the input is scanned (in the wafer plane) using a 1.15μm infra− red HeNe laser.

supposed to be identical, there was some variation. Since the straight waveguides were being used as a standard, this resulted in values as large as 1.5dB at worst. To obtain consistent results requires a large number of samples in order to eliminate errors due to faulty cleaving which is believed to be the main cause for the variations observed.

5.5 Birefringent Pressure Sensor and External Interferometer

5.5.1 Objectives

Due to the initial difficulty in producing chemically etched Mach–Zehnder waveguide structures, a straight waveguide version of the pressure sensor was designed, based on the discovery that the TE and TM propagating modes undergo different phase shifts when traversing the stress field of a distorted membrane, Chap3.

5.5.2 Experimental Procedure

The experimental arrangement is shown in Fig.5.13. Light polarised at 45° to the crystal axes is launched into the guide, exciting both TE and TM polarisations equally. This is achieved by employing two polarisers in conjunction with the semiconductor laser which only provides one polarisation (orientated as TE in this experiment). A quarter–wave plate followed by a linear polariser at 45° to the plane of the TE mode of the laser achieved the necessary polarisation rotation for the input at the expense a reduction in the light intensity. The analysis given below assumes that losses for TE and TM polarisations are negligible but the principles still apply providing the losses are similar.

The output is observed through a linear polariser aligned to that at the input and hence giving maximum output intensity. The 45° linear

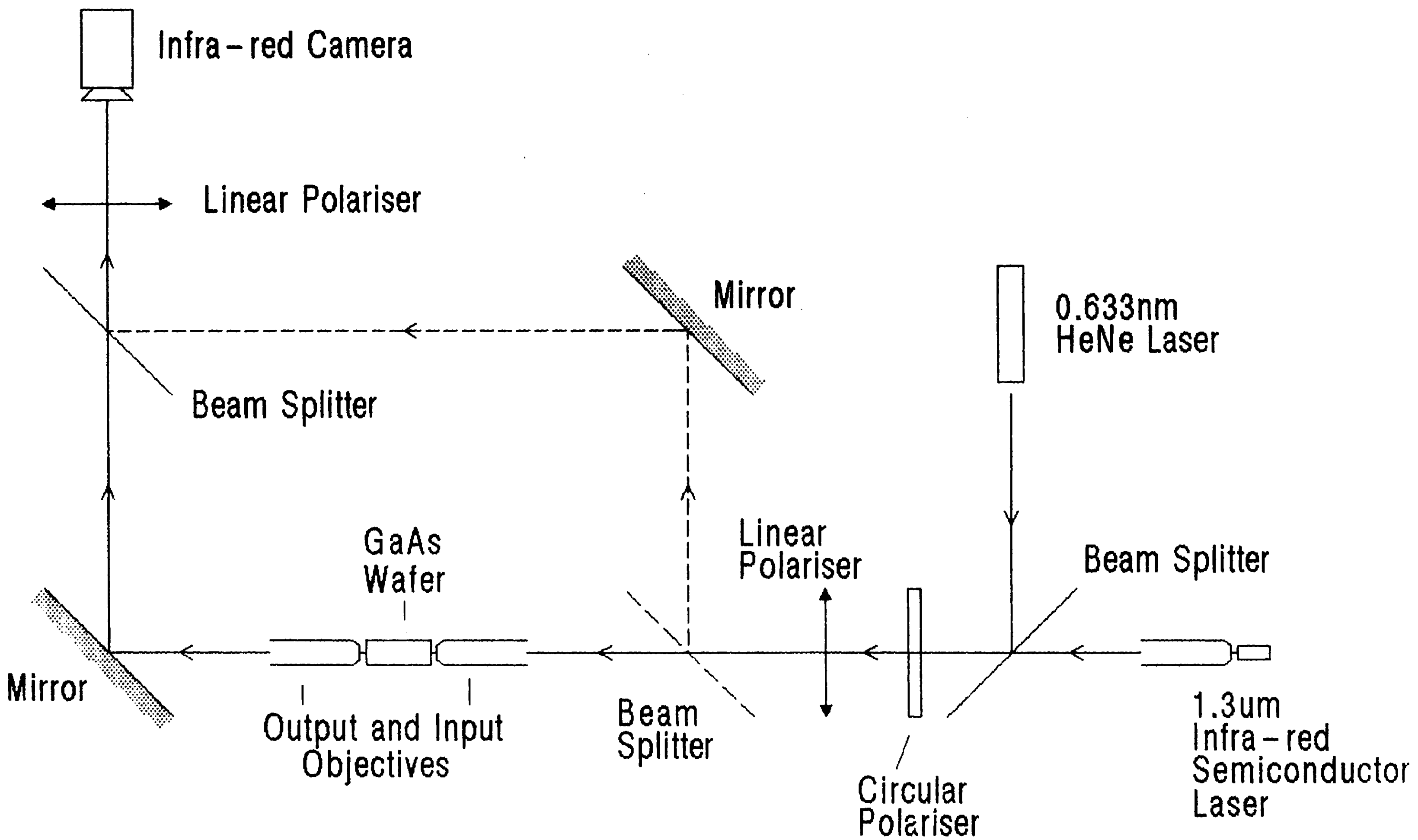

Fig.5.13

Birefringent Pressure Sensor and External Interferometer Apparatus

polarisation of the input beam implies that the phase difference between the TE and TM polarisations is zero. The behaviour of the birefringent pressure sensor is dependent on the relative phase difference between the TE and TM polarisations. Consider the three regimes given below:

(1) If the phase difference between the TE and TM polarisations becomes $\frac{1}{2}\pi$, after travelling through the device, then circular polarisation results. This leads to a reduction in the output intensity.

(2) A phase difference of π results in the output intensity dropping to zero since the output polarisation is now linear and at 90° to that of the input.

(3) Phase differences between those mentioned above lead to elliptical polarisation in the output beam.

The behaviour of the device can now be described for one complete cycle. As the TE and TM modes pass through the pressure-induced stress field of the membrane they experience a change of relative phase, Chap.3. As the phase difference increases the light intensity at the output decreases to zero when the relative phase is π radians. Further increase in the relative phase will bring the output back to a maximum where the phase difference is 2π.

An external bulk interferometer was also set up, shown with dashed lines in Fig.5.13. This system allowed the individual analysis of either TE or TM mode interference. The two paths are recombined on the polariser onto which the camera is then focussed.

5.5.3 Results

Birefringent Pressure Sensor Tests

The following results were obtained for sets of 2μm and 3μm wide ridge waveguides based on the epitaxial system shown in Fig.5.14. The guide crossed the central region of a membrane of dimensions 2mm x 8mm x 25μm along the 2mm direction and were separated by 50μm. There was no measurable difference in the behaviour of the waveguides.

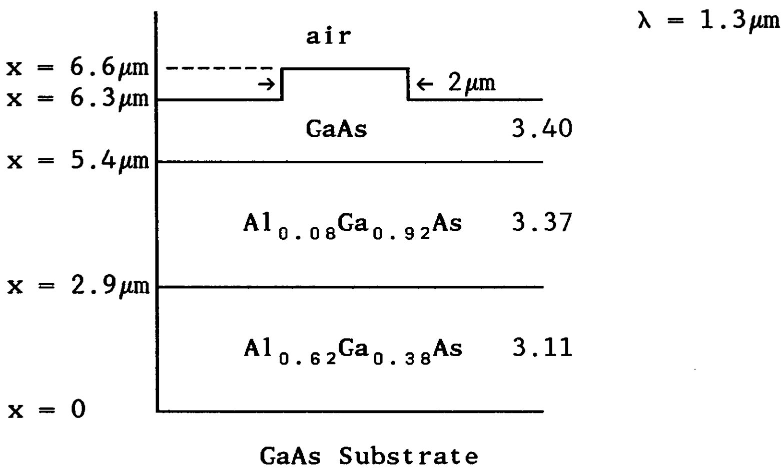

Fig.5.14

Fig.5.15 shows a plot of Amplitude versus pressure. The output was seen to fall by approximately half. From the sinusoidal form obtained, an estimate of P_{π} point was made i.e a π phase change was obtained for a pressure difference of ≃69kPa across the membrane. Substitution of the membrane parameters and light wavelength into the phase equations of Chap.3 indicate a relative phase change of 0.3π radians between TE and TM polarisations respectively.

The reason for the rather poor extinction ratio (−3dB) may be revealed by the effective index method which, when applied to this

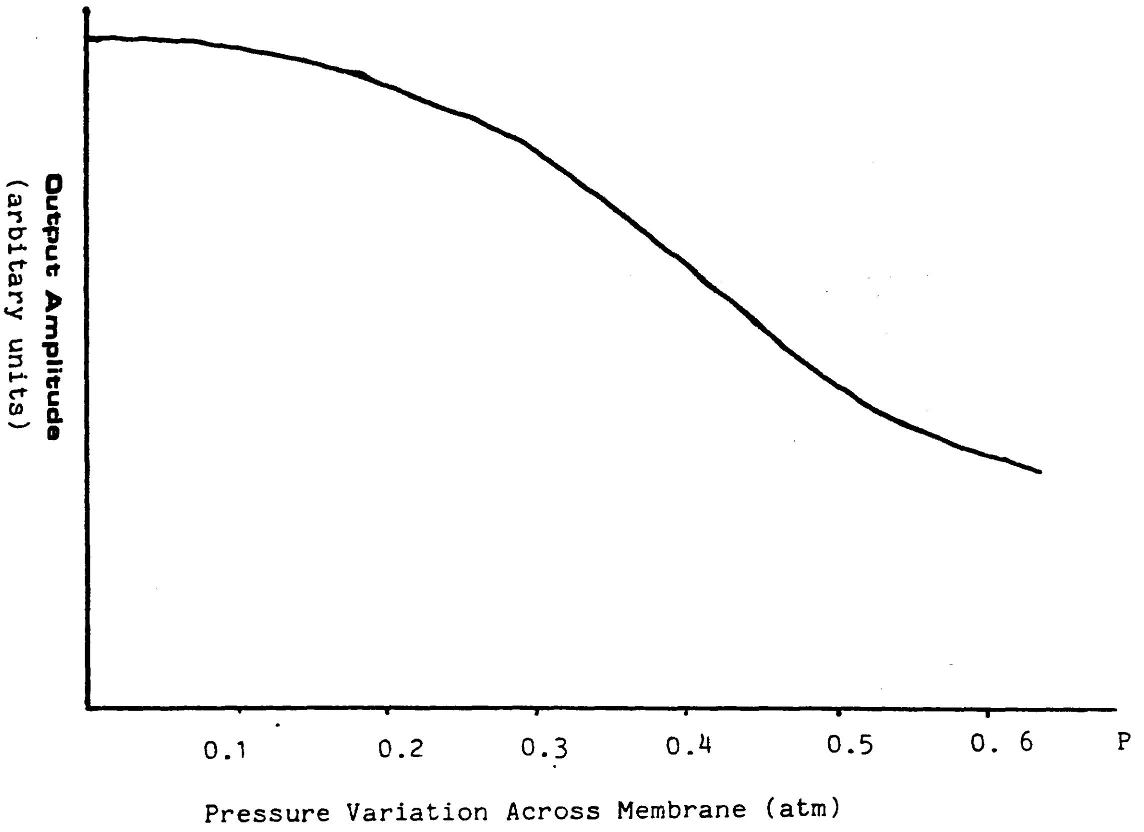

Fig.2.15

Output Amplitude of a birefringent pressure sensor (via pen-recorder)

structure indicates that it is multimode. As well as exciting the fundamental mode, higher-order modes are also supported which results in a background light output which never completely extinguishes even when the π phase difference is achieved for the fundamental modes.

The results for the bulk interferometer were obtained on camera to show the interference pattern that occurs when the guided mode and unguided modes are overlapped. Fig.5.16 shows the vacuum chuck and wafer arrangement with and without pressure applied to the membrane. The pressure across the membrane in the deflected position is 69kPa.

The scan line in the photograph centre has an amplitude plot to the left of the photograph. The first figure has a low amplitude, dark, region indicating destructive interference, while in the second figure constructive interference is seen. The individual phase shifts for the TE and TM polarisations are approximately equal, making it impossible to visually determine which is being studied without checking the orientation of the linear polariser. The lack of contrast in the image on the camera may again be due to the multimode nature of the guide. Other modes in the waveguide would not necessarily interfere destructively under the same conditions as the fundamental mode.

In Fig.5.17 the difference between no pressure, Fig.5.17a, and 34kPa, Fig.5.17b is shown to highlight the π phase shift. Thus, using the external interferometer P_{π} is given by 34kPa which is half the pressure required when using the birefringent pressure sensor. There

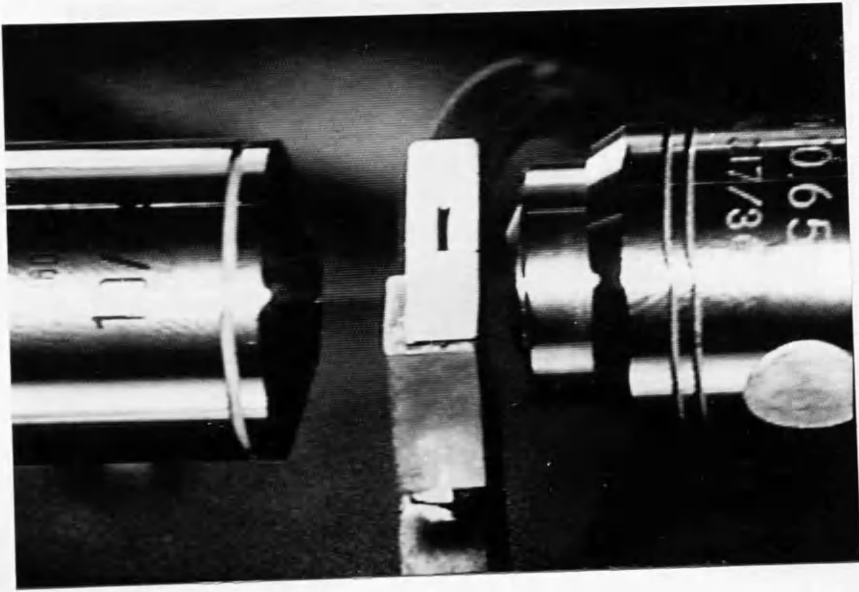

Fig.5.16a

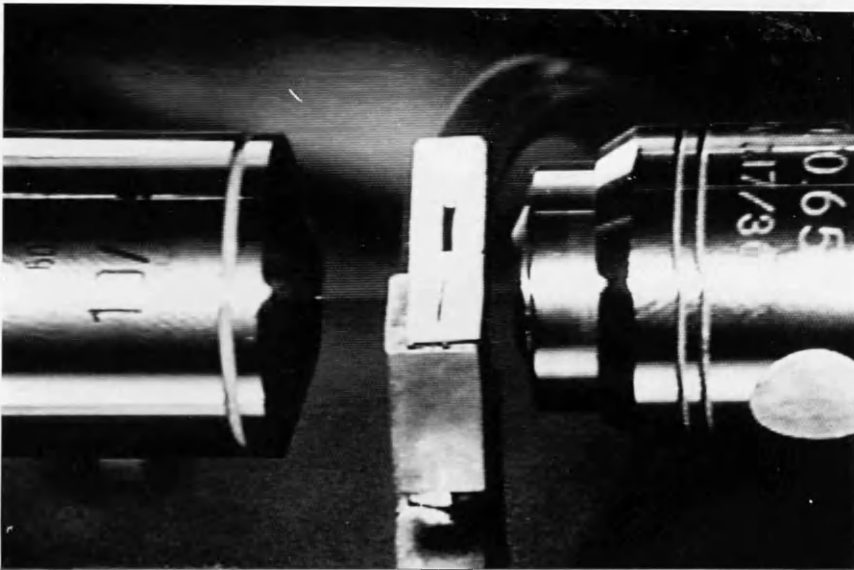

Fig.5.16b

Straight waveguides on a GaAs wafer waxed to a sample holder which can be evacuated. Two identical membranes were fabricated, one aligned to the sample holder while the other was broken to reveal its position. Evacuation of the sample holder reveals the position of the unbroken membrane (Fig.5.16b.

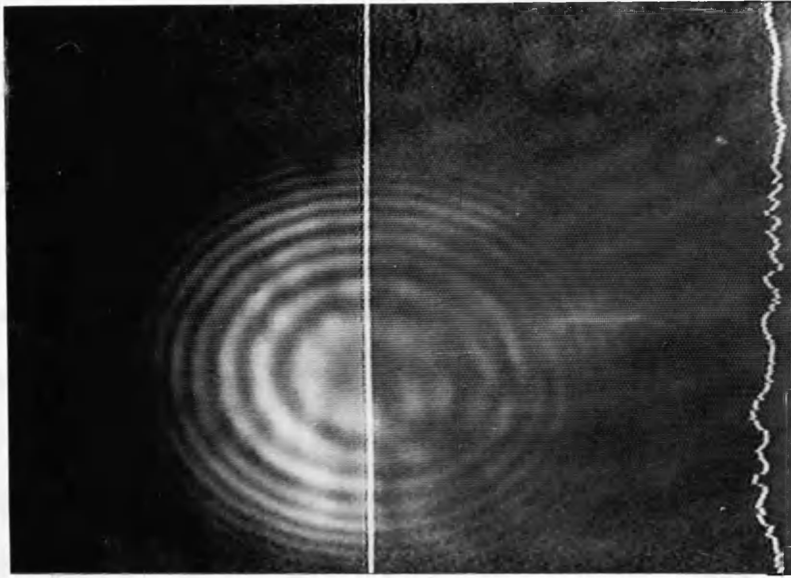

Fig.5.17a

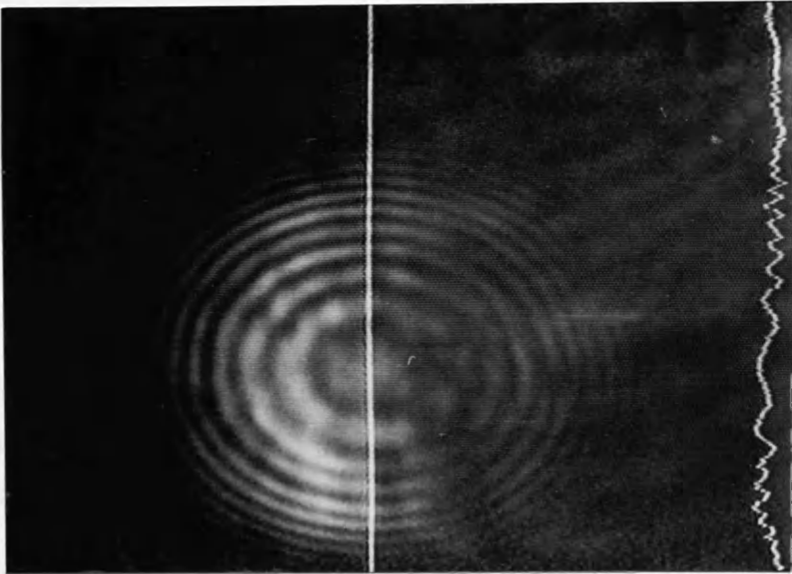

Fig.5.17b

Interference patterns at the output of a birefringent pressure sensor placed in an external interferometer. The scan line indicates:

(a) a central dark fringe when no pressure is applied to the membrane and

(b) a central bright fringe with a pressure differential of 34kPa across the membrane.

is a distinct difference in the sensitivity of the birefringent and bulk interferometer tests as predicted by the theoretical model developed in Chap.3. Using just the TE mode or TM mode provides approximately twice as much phase-shift and both the phase shifts of the TE and TM polarisations occur in the same direction but with different amplitudes. Holding a reference phase constant is expected to increase the phase difference. In the theoretical model presented in Chap.3, the phase shifts of the TE and TM polarisations for a pressure differential of 34kPa are 1.2π and 0.75π radians which lie very close to the measured value of π above. However, under the experimental conditions there was no discernible difference between the phase-shifts for the TE and TM polarisations. The reasons for this discrepancy are at present unclear. In addition, the predicted phase-shifts agree to within a factor of three with those measured experimentally.

5.6 Addendum

Recently, Mach-Zehnder waveguides were successfully fabricated using dry-etching. They were based on the Y-junctions described in this chapter and some time was devoted to obtaining the losses of the devices compared to that of the straight waveguides which were fabricated along side them. As with the case of the Y-junctions, the output intensities of the Mach-Zehnders was found to be consistent for waveguides of the same dimensions on the same wafer. But the straight guides again led to problems of consistency, with variations existing between guides that should have been identical. The losses for Mach-Zehnder waveguides consisting of $4\mu m$ wide guides were, however, estimated to be in the region of 3dB down on the average output of straight guides of the same widths. The predicted losses

due to the presence of the S−bends and Y−junctions is 0.4dB for the particular device dimesions used.

In both the Y−junction and Mach−Zehnder waveguides, the losses predicted by the theories given in Chap.2 tend to be smaller than that measured. Identifying the exact reasons for these discrepancies requires a large number of waveguides to be measured and thus reduce the possiblity of spurious results due to faulty cleaving. More detailed experimental results will make it possible to decide whether the theory is an accurate model and, if it is not, provide clues as to the way in which it can be altered.

References

[5.1] TAMIR, T.:'Integrated Optics', Topics in Apllied Physics, **7**,Springer ann Verlag, 1979

[5.2] LIU, H. and FENG, Z.:'Lloyd's Mirror Interference in a Medium – A New Method for Determining Photoelastic Index Variation', Electronics Letters, **18**, No.6, pp251–252, 1982

[5.3] LEE, K.T.:'III–V Semiconductor Integrated Optical Waveguide Structures for Sensor Applications, MSc Thesis, University of Glasgow, 1986

CHAPTER SIX

Conclusions and Suggestions for Future Work

6.1 Conclusions

This thesis has dealt with the theoretical analysis, fabrication and demonstration of an optical waveguide membrane pressure sensor in the GaAs/AlGaAs epitaxial layer system. Two types of device have been proposed; one based on straight waveguides crossing a membrane and the other formed by a Mach–Zehnder waveguide interferometer with its sensing arm on the membrane. The straight waveguide device has been successfully fabricated, and experimental results obtained from its measurements indicate that the Mach–Zehnder waveguide pressure sensing device is feasible.

Membranes were fabricated by etching, from the wafer base, through the GaAs substrate and stopping approximately $10\mu m$ from the wafer top surface. This was achieved by choosing a suitable combination of wet–chemical etchants and epitaxial layer structure. The membranes were placed in a vacuum system which permitted the pressure on the underside of the membrane to be reduced, thus creating a differential pressure across the membrane thickness. The top surface of the membrane was viewed under a Tolansky microscope producing fringes which allowed the membrane deflection to be measured. A comparison of the deflection predicted by the theoretical model developed in Chap.3 and that measured experimentally showed good agreement.

A theoretical model of the behaviour of a straight waveguide on a stressed membrane, indicated that TE and TM polarisations experience

different phase-shifts as they passed through the stress fields of a deformed membrane. It was decided that a simple straight waveguide device could be fabricated to demonstrate important aspects of the proposed Mach-Zehnder waveguide structure. Two experiments were designed, the first used the stress-induced birefringence of the material to rotate the polarisation of an input beam while the second involved placing the device in an external interferometer and studying the phase-shifts of either the TE or TM polarisations independently. The theoretical phase-shifts for TE and TM modes are 2.4π and 1.5π radians respectively for a pressure difference of 68kPa. The measured phase-shift for both polarisations was 2π. Reasons for the identical phase-shifts are at present unclear. For a membrane of nominal dimensions 2mm x 8mm x $25\mu m$ the relative phase-shift between the orthogonal polarisations was measured to be π radians for an applied pressure of 68kPa. The theoretical prediction for the membrane at this pressure is 0.3π radians relative phase-shift. The disadvantage of such a device for the purposes of monolithic integration lie in the fact that two linear polarisers and a quarter-wave plate need to be incorporated onto the wafer in addition to the laser and detector. Thus, fabrication difficulties favour the use of a Mach-Zehnder waveguide device.

Although the final Mach-Zehnder pressure sensing device was not fully realised in this work, Mach-Zehnder waveguide structures were fabricated and studied. Loss measurements were essential to verify that the amount of light scattered by the S-bends and Y-junctions (particularly with the large arm separations of $300\mu m$) would make realisation of the device feasible. The Y-junctions were formed by a pair of intersecting S-bends with radius of curvature 40mm and arm

separations of 300μm. The losses were measured and found to be approximately 1dB greater than for straight waveguides on the same wafer. Overall losses for the complete Mach–Zehnder waveguide structure losses were measured indicating that they were approximately 2.3dB greater than for straight waveguide counterparts. This indicates that the losses experienced at the Y–junction power divider (at the input end of the Mach–Zehnder structure) are approximately the same as that at the Y–junction coupler (at the output end of the Mach–Zehnder structure). However, it must be stressed that these are preliminary figures based on one wafer sample. In addition, identical Mach–Zehnder waveguide structures on one wafer had similar output intensities, but this was not true of all the straight waveguides measured on the same wafer even though these guides were, to all intents and purposes, identical. Some of the straight waveguides showed particularly low output intensities which could have resulted from damaged cleaved ends. For a more accurate analysis it is important to use a large number of identical waveguides on one wafer.

At present there is no immediate market for integrated optical sensor devices, and apart from an initial foray into this area progress has been fairly slow. On the optical fibre sensor front, a great deal of interest has been shown as the commercial aspects of optical fibres become more familiar[1]. However, the work presented in this thesis has indicated that sensors in the AlGaAs system are feasible and, with the possibility of monolithic integration, do have a place in the sensor industry.

6.2 Further Work

(1) A `detailed study of the losses in S− bends, Y− junction and Mach− Zehnder waveguides in comparison with straight waveguides of the same geometry, length and cross− section requires.

(2) A determination of the membrane shatter point as a function of pressure and membrane dimensions. By restricting the membrane dimensions it should be possible to carry out a large number of measurements for membranes formed on small wafer samples.

(3) A more recent consideration indicates that the apparatus used to monitor the deflection of a membrane, Sec.5.2.2, could possibly be carried out on end− fire apparatus. The Lloyd's interference patterns[2], which become evident when using end− fire apparatus to launch light into a waveguide, appear as parallel lines for a flat membrane. A deformed membrane on an otherwise flat wafer would appear as a deformation of the parallel interference fringes which could be monitored using, for example, a Hammamatsu camera.

(4) Incorporating an electrode arrangement in the reference arm of a Mach− Zehnder waveguide would allow phase− shifts to be made via the electro− optic effect. This would allow the output of the device to be biased and hence increase the sensitivity of the device.

(5) Various films evaporated onto the membrane base should have minimal effects on the waveguiding properties in the membrane region. Coating the base of the membrane with, for example nickel, and applying a magnetic field across the membrane causes stress− induced index changes via manetostriction. This opens the possibility of a magneto− optic sensor.

(6) Work currently being carried out by the Ultra− small Structures

Group at Glasgow University indicates that bridge structures can readily be formed in the AlGaAs system. In simple terms, two closely placed parallel lines etched into the top surface of a wafer produce a ribbon or bridge structure as the etched regions join up below the surface of the material. Such structures have already been fabricated successfully in silicon and form the basis of a number of resonator– type devices.

(7) There is also the possibility of exploiting the dynamic properties of membranes in, for example, an accelerometer or studying their resonance characteristics.

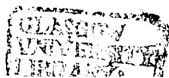

References

[6.1] CULSHAW, B.:'Optical Fibre Sensing and Signal Processing', Peter Peregrinus Ltd, 1984

[6.2] LIU, H. and FENG, Z.:'Lloyd's Mirror Interference in a Medium — A New Method for Determining Photoelastic Index Variation', Electronics Letters, **18**, No.6, pp251—252, 1984